POLITECNICO
MILANO 1863

SCUOLA DI INGEGNERIA INDUSTRIALE
E DELL'INFORMAZIONE

Performance Analysis of Wells Turbines with VIGV for Wave Energy Exploitation

Tesi di Laurea Magistrale in
Aeronautical Engineering - Ingegneria Aeronautica

Author: **Oscar Zanisi**

Student ID: 969792
Advisor: Prof. Paolo Gaetani
Co-advisors: Noraiz Mushtaq
Academic Year: 2022-23

Abstract

Oscillating water column (OWC) systems hold significant promise for sustainable power generation. Among the various options, Wells turbines emerge as strong candidates for harnessing marine wave energy. However, they are subject to operational limitations, such as Stall and Total-drag, that reduce their optimal performance. To mitigate these phenomena, researchers have explored different techniques, including the installation of fixed guide vanes (GV) before and after the rotor.

This thesis delves into the comprehensive analysis of Wells turbine behaviour and proposes a novel performance enhancement strategy. The approach involves the addition of two sets of Variable Inlet Guide Vanes (VIGV) positioned upstream and downstream of the rotor.

The primary objective is to investigate the impact of VIGV on turbine performance under variable wave conditions. Starting from the turbine design, the implemented model analyses the performance of various machine configurations: the rotor with constant chord or constant solidity, with or without guide vanes.

Computational Fluid Dynamics (CFD) is employed for a detailed validation of the proposed model. Through it, analyses are carried out on the rotor alone and on different configurations of the stators. Moreover, simulations of meaningful cases are performed on the complete geometry.

The findings of this research suggest that the implementation of a VIGV system enhances the overall performance of the machine, confirming its viability as a valid strategy to optimize marine wave energy extraction in OWC power plants.

Keywords: Wells Turbine, Oscillating Water Column, Variable Inlet Guide Vanes, Computational Fluid Dynamics.

Abstract in lingua italiana

I sistemi basati sul principio della colonna d'acqua oscillante (OWC) rappresentano una promessa significativa per la generazione sostenibile di energia. Tra le varie opzioni, le turbine Wells si rivelano essere le candidate migliori per sfruttare l'energia delle onde marine. Tuttavia, esse sono soggette a limitazioni operative, come lo stallo e la fase di total-drag, che ne riducono le prestazioni ottimali. Per mitigare questi fenomeni, i ricercatori hanno esplorato diverse tecniche, tra cui l'incorporazione di guide fisse (GV) prima e dopo il rotore.

Questa tesi approfondisce in modo esaustivo il comportamento delle turbine Wells e propone una nuova strategia per migliorarne le prestazioni. L'approccio prevede l'aggiunta di due serie di guide variabili (VIGV) posizionate a monte e a valle del rotore.

L'obiettivo principale è investigare l'impatto delle VIGV sulle prestazioni della turbina sotto l'effetto di onde di diversa intensità. A partire dal dimensionamento della turbina, il modello implementato analizza le prestazioni di varie configurazioni della macchina: rotore con corda costante o solidità costante, ciascuno dei quali con o senza guide.

Per convalidare il modello proposto, si ricorre all'analisi CFD (Computational Fluid Dynamics). Attraverso di essa, vengono condotte analisi sul solo rotore e su diverse configurazioni degli statori. Inoltre, vengono eseguite simulazioni di casi significativi sull'intera geometria.

Le conclusioni di questa ricerca suggeriscono che l'aggiunta di un sistema VIGV migliora le prestazioni complessive della macchina, confermando la sua validità come strategia per ottimizzare l'estrazione di energia dalle onde marine nel contesto di un impianto OWC.

Parole chiave: Turbina Wells, Colonna d'acqua oscillante, Guide d'ingresso variabili, Fluidodinamica Computazionale

Contents

Introduction

Context

The interest in renewable energy sources has gained significant role in recent years, driven by their importance in reducing emissions and environmental impact. Among all renewable sources, wave energy stands out as one of the most intriguing options due to its abundant availability and relatively high predictability. Consequently, various technological solutions have been proposed to harness and convert this energy source effectively. One widely applied principle in Wave Energy Converters (WECs) is the Oscillating Water Column (OWC), which involves a partially submerged chamber open at the bottom. This chamber generates alternating airflow in a connected duct through the movement of the water column inside. Wells turbines are commonly employed in the majority of these devices to convert the pressure energy of the alternating airflow into mechanical energy, subsequently generating electrical power through a generator.

A Wells turbine, named after its inventor Dr. A. H. Wells, is a type of axial turbine designed to harness energy from OWC systems in the field of wave energy conversion. Operating within the principles of fluid dynamics, the Wells turbine is specifically tailored for the variable airflows generated by the OWC. The distinguishing feature of this turbine lies in its symmetrical airfoil rotor blades, optimized for bidirectional airflows and ease of rotation, eliminating the need for complex non-return valves mechanisms that are necessary for other turbines. As the OWC system interacts with the turbine, the alternating airflow created by the water column's vertical movement induces rotation in the Wells turbine. Its symmetrical blade design ensures rotation in the same direction regardless of airflow direction, enabling consistent energy conversion during both inward and outward air flows. This characteristic aligns well with the oscillating nature of the OWC system, allowing the turbine to harness energy efficiently from wave-induced air movements.

However, the Wells turbine also presents limitations and drawbacks, in particular at low and high velocity air flows it can lead to performance limitations due to stalling and total-drag conditions. Stalling occurs when airflow separates from the blade surface, leading

to reduced efficiency. Total-drag condition arises when excessive drag counteracts the rotational force, further diminishing turbine effectiveness (at low velocity air flows).

To address these limitations and enhance Wells turbine performance, research focuses on innovative solutions and proposes a lot of alternative improved configurations.

These include solutions such as the bi-plane Wells turbine, wich consist of a series of two rotor elements that can be co-rotating or contra-rotating, the incorporation of guide vanes, strategically placed upstream and downstream of the rotor, to optimize airflow dynamics and minimize stall and drag effects.

By carefully designing and integrating these stator components, researchers aim to refine the Wells turbine's efficiency, allowing an effective energy conversion in OWC systems and advancing the viability of wave energy as a renewable energy source.

Literature Review

Reference [1] offers an encompassing review of the various approaches to harness the wave energy. Notably, the discourse includes an exploration of various turbine systems, a cornerstone in the quest for efficient wave energy conversion. Wells turbines, renowned for their adaptability in oscillating water column systems, occupy a pivotal position in this context. Their symmetrical blade design allows for bidirectional airflow, aligning perfectly with the oscillating nature of wave-induced air movements. Additionally, impulse turbines, a promising counterpart, are also dissected within this study.

Reference [2] provides an exhaustive overview of the primary technologies employed for extracting energy from ocean waves within an Oscillating Water Column (OWC) system. This comprehensive survey contains an array of innovative solutions designed to harness the potential of wave energy. Among these, notable approaches include the Wells turbine with guide vanes (WTGV), which integrates guide vanes to enhance efficiency and mitigate operational limitations. The Biplane Wells turbine with guide vanes (BWGV) extends the concept further by exploring biplane configurations to optimize energy conversion. Another intriguing technology is the Turbine using self-pitch-controlled blades (TSCB), which employs self-adjusting blades to adapt to varying flow conditions, ensuring optimal performance. Moreover, the Contrarotating Wells turbine introduces a novel concept by employing two counter-rotating rotors to enhance energy capture efficiency.

An important aspect for Wells turbines lies in their machine configuration. Following the studies conducted by the authors of references [3] and [4], and notably the research by Raghunathan [5], which serves as a milestone in this field, it is revealed that an

excellent choice for the rotor involves utilizing unswept NACA0015 airfoil profiles, with a midspan solidity of 0.4. The machine's performance with only the rotor is primarily enhanced by solutions that involve the implementation of fixed stator elements upstream and downstream of the rotor, while adhering to the symmetry necessary for operation under oscillating flow conditions.

The research has introduced other alternative methods to control phenomena that compromise turbine efficiency. For instance, strategies such as morphing blades, stall fences, and plasma actuators have been envisaged to manage stall. These innovative approaches aim to counteract the detrimental effects of stall by dynamically altering blade shapes through morphing blades [6], employing stall fences to divert airflow and prevent separation [7], and utilizing plasma actuators to influence boundary layer conditions and enhance airflow control [8].

All these methods aim to maximize the performance of Wells turbines, and research continually strives to discover novel alternative approaches. This study falls within this context, examining and proposing a new method to optimize wave energy utilization through Wells turbines.

Structure of this work

This work is divided into five chapters.

The first chapter contains a collection of theoretical concepts that form the basis of the operation of a Wells turbine in an OWC system.

The second chapter describes the implemented method for modeling its behavior based on the chosen geometry and operating conditions.

The third chapter deals with CFD (Computational Fluid Dynamics) tests performed to validate the choices behind the model described in the previous chapter. Results of the CFD analysis are also reported here.

The fourth chapter is dedicated to the parametric analysis and its results carried out to analyse the turbine under the effect of different waves.

Lastly, in the fifth chapter, the conclusions of this work are drawn and and an outlook on this topic is provided.

1 | The Wells Turbine

This chapter discusses the OWC Power Plant and the Wells turbine, addressing all the key aspects necessary to understand the functioning of this strategy to extract energy from the ocean waves. Everything related to the plant's structure, machine geometry, advantages, disadvantages, and issues that arise during operational conditions is presented in this chapter.

1.1. The OWC Power Plant

1.1.1. The OWC structure

An Oscillating Water Column (OWC) power plant is a technology that captures energy from ocean waves to generate electricity. Its structure, shown in fig. 1.1, consists of a partially submerged chamber open at the bottom, allowing the inflow and outflow of seawater due to wave-induced oscillations. This movement alternately compresses and decompresses the air within the chamber.

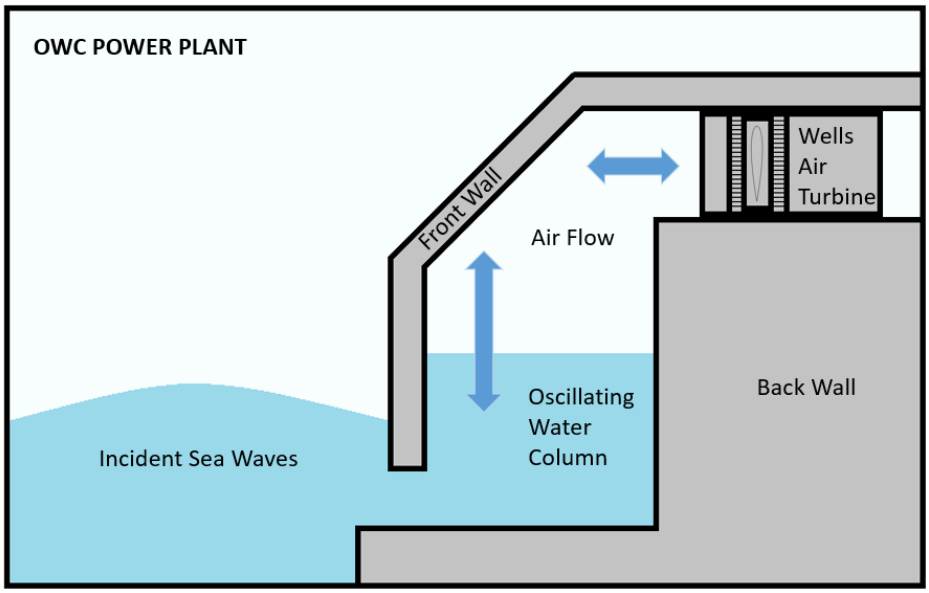

Figure 1.1: The OWC Power Plant

As waves enter the chamber, the air is pushed upwards through a turbine situated at the chamber's top. This turbine, commonly a Wells turbine, converts the air movement into mechanical energy. An electric generator is connected to the turbine, further converting this mechanical energy into usable electrical power.

The strength of the OWC power plant lies in its straightforward design and effective energy conversion process. Ocean waves, a consistent renewable energy source, drive the continuous oscillations, ensuring a reliable power generation cycle. The Wells turbine is the best solutions for oscillating airflows since it eliminates the need for intricate flow rectification systems.

Oscillating water columns operate without any submerged components that could impact marine life. Also, offshore OWC systems might have a positive ecological impact by potentially fostering marine habitats through the creation of artificial reefs. However, a key challenge lies in the potential noise pollution generated by OWCs and the aesthetic appeal of coastal landscapes.

1.1.2. OWC main parameters

An OWC facility is designed based on the average parameters of oceanic waves prevailing in the chosen location. A practical approximation to characterize wave behavior is to model it as a sinusoidal waveform, thus describable by two fundamental parameters: amplitude (a) and frequency (f). These parameters allow to understand the wave's fundamental characteristics and tailor the OWC system to efficiently harness the oscillating energy of the waves. From here, the wave elevation can be defined:

$$e = a \sin(2\pi f t) \quad [m] \tag{1.1}$$

Regarding the structure of the OWC, a pivotal parameter is the surface area of the lower section of the tower (S_{owc}) where waves enter. This parameter significantly influences the volume of air entrapped and subsequently displaced within the chamber, playing a central role in determining the energy conversion potential of the system. Properly sizing this area allows for effective capture and utilization of wave energy to drive the oscillating air column within the chamber, thus facilitating efficient energy transfer and power generation.

From these parameters, it is possible to assess the volumetric flow rate generated from a wave characterized by amplitude (a) and frequency (f) into an OWC power plant charac-

terized by lenghth (L) and width (Z):

$$Q(t) = L \cdot Z \cdot \frac{de}{dt} = L \cdot Z \cdot a \cdot 2\pi \cdot f \ \cos(2\pi f t) \quad [kg/m^3] \tag{1.2}$$

whose the maximum value is:

$$Q_{max} = S_{owc} \cdot a \cdot 2\pi \cdot f \quad [kg/m^3] \tag{1.3}$$

In the context of wave energy and Wells turbines, it's important to note that shock waves and supersonic currents are not relevant due to the subsonic nature of ocean waves. The fluid is commonly treated as incompressible, aligning with the subsonic flow regime associated with wave-induced motion and turbine operation.

By incorporating the dimensions of the chamber and the interaction between the oscillating air column and the incoming waves, it is possible to calculate the potential air flow that can be harnessed for power generation. This estimation is fundamental for designing the overall system and optimizing its efficiency, ensuring that the generated power aligns with the available wave resources in a given location. Also it is possible to evaluate the available Power of the OWC:

$$P_{a\ owc} = \frac{\rho_w \cdot a^2 \cdot 9.81^2}{f \cdot 8\ \pi} \quad [W/m] \tag{1.4}$$

The true wave potential is lower as not all the available power is converted into the OWC due to wave directionality issues, internal dissipations and the interaction with sea ground.

1.2. The Wells Turbine

1.2.1. Velocity triangles and Euler work

Like any other turbomachinery, the Wells turbine also relies on velocity triangles as a fundamental aspect to analyze how fluid interacts within a bladed stage. Therefore, the three vectors that are used to build velocity triangles are defined as: V, U and W.

- V: Absolute velocity, represents the fluid's velocity with respect to an absolute observer.
- U: Peripheral velocity, is the machine's velocity with respect to an absolute observer.
- W: Relative velocity, denotes the fluid's velocity relative to the machine.

These three vectors are linked by the kinematic relation:

$$\vec{V} = \vec{U} + \vec{W} \tag{1.5}$$

These vectors provide essential insights into the fluid dynamics and energy transfer occurring across the turbine's blades, in fact the most significant concept associated with these vectors is the concept of Euler Work:

$$L_{eul} = U_2 V_{2t} - U_1 V_{1t} = \frac{V_2^2 - V_1^2}{2} + \frac{U_2^2 - U_1^2}{2} - \frac{W_2^2 - W_1^2}{2} \tag{1.6}$$

which represents the work exchanged between the blades and the fluid (it is considered positive if the energy level of the flow increases, so for a turbine is negative). Dimensionally, this is a specific work per unit of mass [J/kg], and it signifies a change in total enthalpy:

$$L_{eul} = \Delta h_T = \left(h_2 + \frac{V_2^2}{2} + g z_2\right) - \left(h_1 + \frac{V_1^2}{2} + g z_1\right) \tag{1.7}$$

The terms related to gravity are usually neglected, and this leads to the definition of another important quantity called Rothalpy:

$$R = h + \frac{W^2}{2} - \frac{U^2}{2} \tag{1.8}$$

When considering rothalpy, it is important to note that, just as total-enthalpy $\left(h_T = h + \frac{V^2}{2}\right)$ remains constant across a stator element, rothalpy is a quantity that remains constant within the rotor.

Furthermore, considering the fundamental equation of Thermodynamics:

$$Tds = dh - \frac{dP}{\rho} \tag{1.9}$$

since the Euler work represent the work exchanged in an iso-entropic process ($ds = 0$), it can also be expressed as:

$$L_{eul} = \frac{\Delta P}{\rho} \tag{1.10}$$

This parameter is crucial for assessing the energy transformation within the turbine and plays a pivotal role in evaluating the turbine's efficiency and performance.

1.2.2. Features

The easiest design of a Wells turbine consists of a rotor, a shaft, and a set of blades. The rotor is the primary component and is made of a series of blades arranged around the axis of rotation, as shown in fig. 1.2.

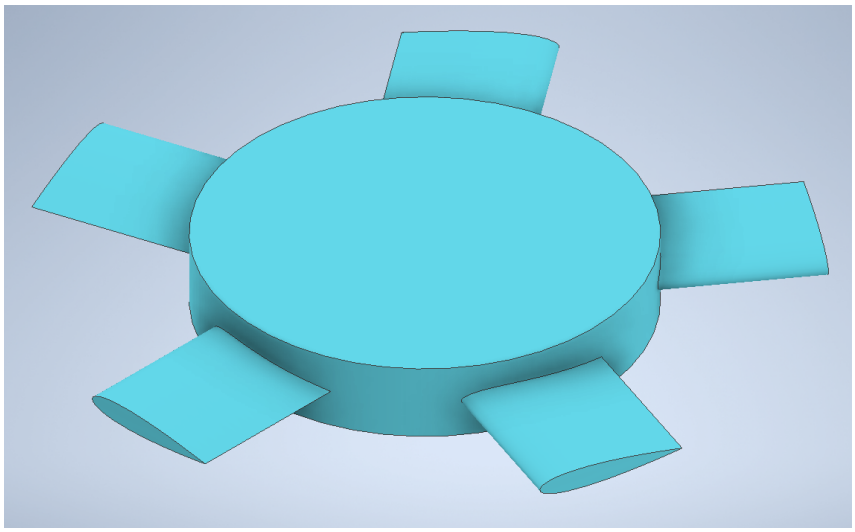

Figure 1.2: The Wells rotor

The blades of a Wells turbine are characterized by their symmetrical and slender design, ensuring consistent rotation in a single direction regardless of the airflow's orientation, as shown in fig. 1.3. When the airflow passes through the blades, it generates aerodynamic forces that initiate the rotation of the turbine.

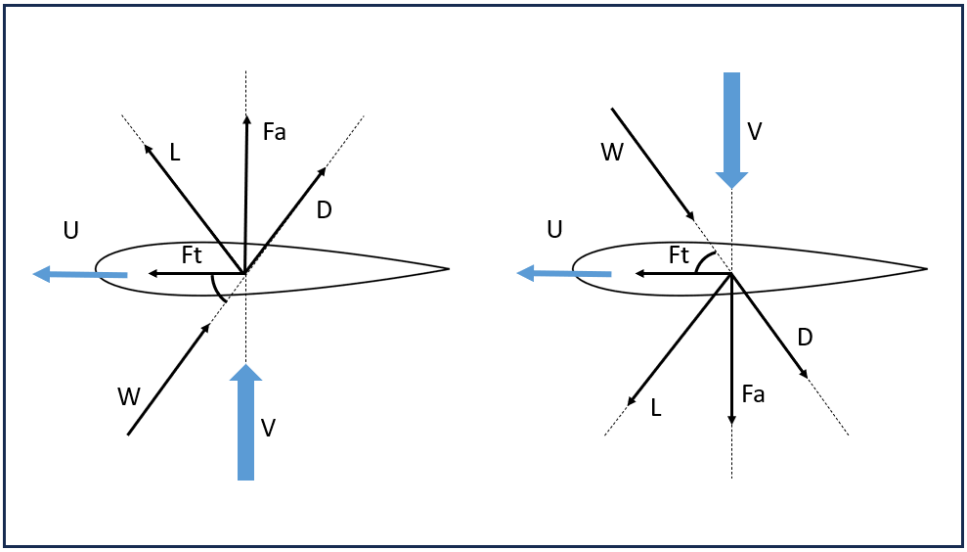

Figure 1.3: Working principle of a Wells turbine

When the blade is exposed to an airflow with incidence β, it experiences an aerodynamic force that can be decomposed into two components: Lift (L) and Drag (D). For analyzing the behavior of a Wells turbine, it makes sense to consider the axial resultant (Fa) and the tangential resultant (Ft) of these forces, as one represents the structural load on the blade and the other is responsible for the rotational movement of the machine:

$$Ft = L \cdot sin(\beta) - D \cdot cos(\beta) \tag{1.11}$$

$$Fa = L \cdot cos(\beta) + D \cdot sin(\beta) \tag{1.12}$$

Wells turbines, renowned for their straightforward structure, offer significant advantages that have made them a popular choice in various applications. The symmetry of the blades plays a crucial role, allowing them to function without the need for a complex flow rectification system. This simplified design not only reduces production costs but also contributes to the longevity and reliability of the turbines.

However, despite their strengths, Wells turbines also present operational challenges. Their efficiency is not consistent throughout all phases of the operational cycle, which represents the passage of a wave. This limitation can impact performance in various ways. When the airspeed surpasses a certain threshold, the blades are at risk of entering stall conditions. This circumstance not only decreases efficiency but can also cause structural damage to the blades themselves. Conversely, when the airspeed drops below a certain level, the turbine might continue to rotate solely due to inertia, without effectively harnessing power from the airflow. This phenomenon is known as "total-drag" and can further compromise efficiency and overall turbine performance. The primary challenge in designing a Wells turbine lies in mitigating these two phenomena.

1.2.3. Stall Condition

The phenomenon of stall in an aerodynamic profile occurs when the angle of attack, which is the angle between the profile's chord line and the direction of the incoming airflow, becomes too steep, as shown in fig. 1.4. This happens when the absolute velocity of the airflow increases over a certain value. As the angle of attack increases, the airflow over the upper surface of the profile begins to separate from the surface, leading to a decrease in lift and an increase in drag. This separation disrupts the smooth flow of air and causes turbulent vortices to form, significantly reducing the profile's overall lift-producing capabilities.

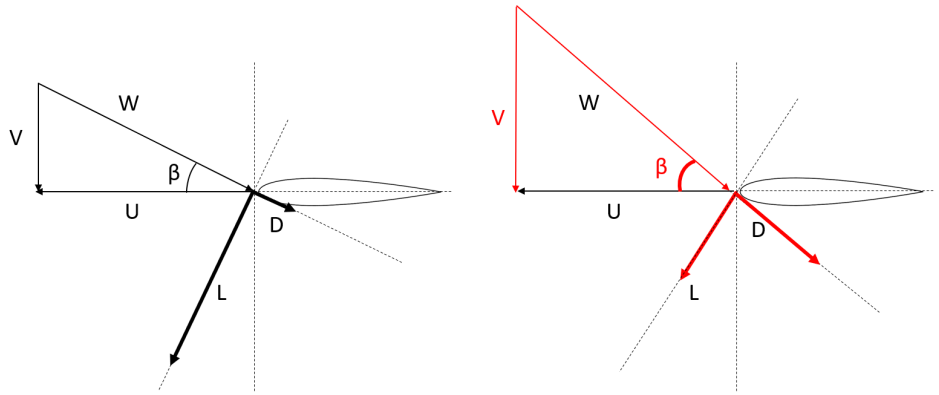

Figure 1.4: Stall condition

Stall is a critical point in aerodynamics because it marks the limit beyond which the profile's lift performance deteriorates rapidly. Once the stall angle is exceeded, the lift drops abruptly, and the profile becomes less controllable and stable. On a Wells turbine, this phenomenon results in a decreased extraction of power and consequently leads to a reduction in efficiency.

1.2.4. Total-Drag Condition

As the airflow velocity decreases beyond a certain threshold, as shown in fig. 1.5, the tangential force driving the turbine's rotation reduces in magnitude. Eventually, the turbine continues to rotate due to inertia but ceases to extract energy from the fluid. Instead, it starts performing work on the airflow, a phenomenon known as total-drag condition.

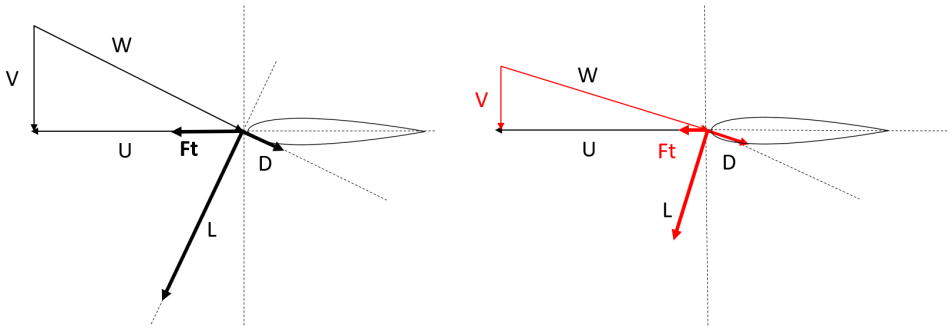

Figure 1.5: Total-Drag condition

The total drag condition is quite critical as it is never entirely avoidable due to the fact that during the passage of a wave, there is always a moment when the velocity tends to zero, especially when the wave comes to a standstill. This phenomenon introduces a challenging aspect in the operation of OWC systems, where the air turbine needs to continue its rotation even in these low-velocity scenarios to prevent a reversal of energy flow from the air column back to the wave, ensuring consistent power generation from the wave energy resource.

1.2.5. Losses evaluation

In the turbomachinery environment, losses are defined as an increase in entropy [9]. For turbines, it's worth noting that they result in a decrease in the actual work extracted from the fluid within the expansion process, shown in fig. 1.6.

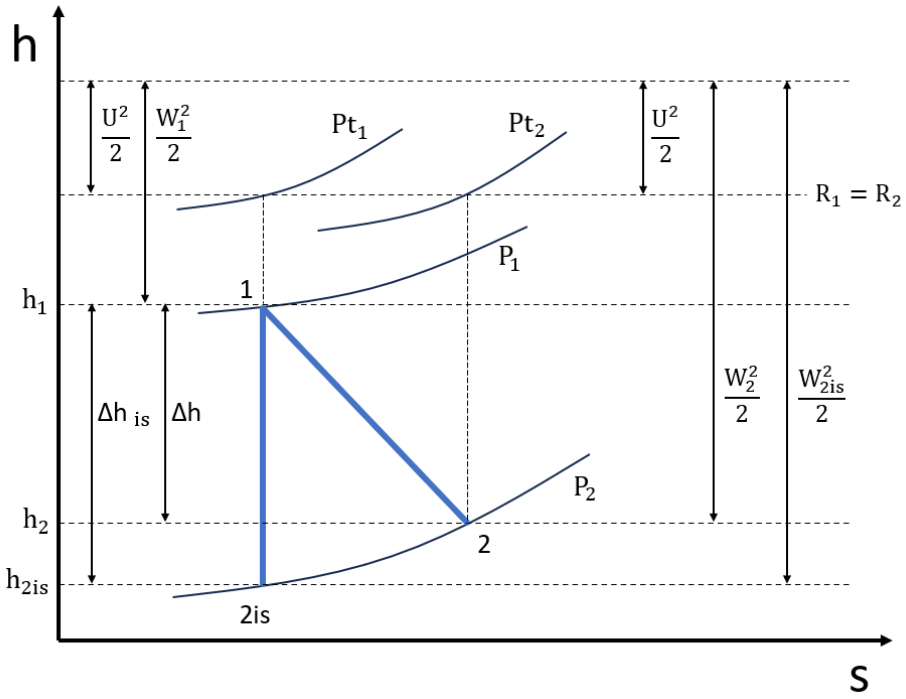

Figure 1.6: Expansion process within a rotating stage

In presence of losses, the process becomes non-ideal. The impact of losses on the entire expansion process is evaluated by efficiency, defined as:

$$\eta = \frac{\Delta h}{\Delta h_{is}} \tag{1.13}$$

Various methods exist to evaluate losses, contingent upon the type and diverse scenarios

encountered. Frequently, recourse is taken to models that involve the use of loss coefficients which frequently stand for an overall pressure loss in the system. These coefficients are defined across a single stage and are dimensionless, scaled by a dynamic pressure:

$$Y = \frac{Pt_1 - Pt_2}{Pt_1 - P_1} \tag{1.14}$$

These coefficients are defined through specific correlations depending on the model and can vary across different components and operational conditions, making them a versatile tool for quantifying losses and optimizing performance.

In the case of a simple configuration of a Wells turbine, comprising only the rotor, several types of losses need to be considered. These include: Profile losses, which are dependent on the blade geometry and the boundary layer generated around them when exposed to an airflow. The effect of these losses results in an increase in drag force on the profile and thickening of the vortex regions, phenomena that impede the blade's advancement and disrupt the flow's smoothness, leading to a less efficient energy exchange. In a context like that of Wells turbines, where analysis can be conducted treating the fluid as incompressible, the following relationship between drag coefficient and total pressure losses can be considered:

$$c_D = \frac{D}{0.5\ \rho\ c\ V_\infty^2} = \frac{s}{c}\ Y\ \frac{\cos \alpha_m^3}{\cos {\alpha_{out}}^2} \tag{1.15}$$

Additionally, there are Clearance losses, which concern the portion of air that is not influenced by the rotor blades and instead bypasses the rotor, leaking through the gap between the blade tips and the outer casing of the machine. Clearance losses are often evaluated using the Dunham & Came model [10], which also incorporates Secondary flow-related losses.

$$Y_{cle} + Y_{sec} = \frac{c}{b}\left[0.0334\ \frac{\cos \alpha_{out}}{\cos \alpha_{in}} + B\left(\frac{k}{c}\right)^{0.78}\right]\left(\frac{c_L}{s/c}\right)^2\ \frac{\cos {\alpha_{out}}^2}{\cos {\alpha_m}^3} \tag{1.16}$$

where: k is the clearance, s is the pitch, c is the chord, B is a parameter that is equal to 0.37 if the blades are shrouded and 0.47 if the blades are unshrouded and c_L is the lift coefficient, that can be evaluated as:

$$c_L = 2\ \frac{s}{c} |\tan \alpha_{in} - \tan \alpha_{out}|\ \cos \alpha_m \tag{1.17}$$

However, for a Wells turbine with just a rotor configuration, considering the contribution

of Secondary flow-related losses is unnecessary due to the flat and successive arrangement of the blades, which prevents the formation of vortex channels as observed in some other turbine designs.

$$Y_{cle} = \frac{c}{b}\, B \left(\frac{k}{c}\right)^{0.78} \left(\frac{c_L}{s/c}\right)^2 \frac{\cos \alpha_{out}{}^2}{\cos \alpha_m{}^3} \tag{1.18}$$

It is notable that these quantities often depend on the aspect ratio c/s, known as solidity. This parameter is indeed a crucial dimensionless factor indicating the density of the blade row in a stage and thus how much it obstructs the airflow. During the design phase, the choice of solidity is a critical aspect as it significantly influences the performance of a turbomachine.

Lastly, Kinetic energy losses play a role, becoming more pronounced as the kinetic energy of the outflowing air increases. To understand the meaning of this type of loss, the kinetic energy loss coefficient is used (the significance of this coefficient is dual to the concept of efficiency), which for an expansion process is defined as:

$$\zeta = \frac{h_2 - h_{2is}}{h_{t2} - h_2} = \frac{h_2 - h_{2is}}{V_2^2/2} = \frac{V_{2is}^2 - V_2^2}{V_2^2} \tag{1.19}$$

these losses can be mitigated by reducing the flow velocity at the outlet section.

As mentioned earlier, losses should be understood as an increase in entropy, which occurs due to dissipations. Starting from the fundamental equation of thermodynamics, this increase is quantified as:

$$ds = c_P \frac{dT}{T} - R \frac{dP}{P} \tag{1.20}$$

and since $T_{t1} = T_{t2}$ the entropy variation is:

$$\Delta s = R \ln \frac{P_{t1}}{P_{t2}} \tag{1.21}$$

1.3. Design parameters

This section is dedicated to the work conducted by S. Raghunathan [5], which stands as a milestone in the study of Wells turbines. The significance of this study, serving as the foundation of this thesis, lies in its comprehensive and precise theoretical analysis, with concepts and findings validated through experiments conducted by the author. Moreover, all the necessary data, graphs, and concepts are made available, enabling a comprehensive and in-depth exploration of this turbine type.

1.3.1. Studies and experiments on two dimensional symmetric airfoils

Since Wells turbines feature a blade arrangement composed of symmetric airfoils, it is essential to comprehend their behavior when subjected to an airflow. Raghunathan's study begins from this point, analyzing the performance of various symmetric NACA airfoils (typically thin) under the same operating conditions. Results are visible in fig. 1.7:

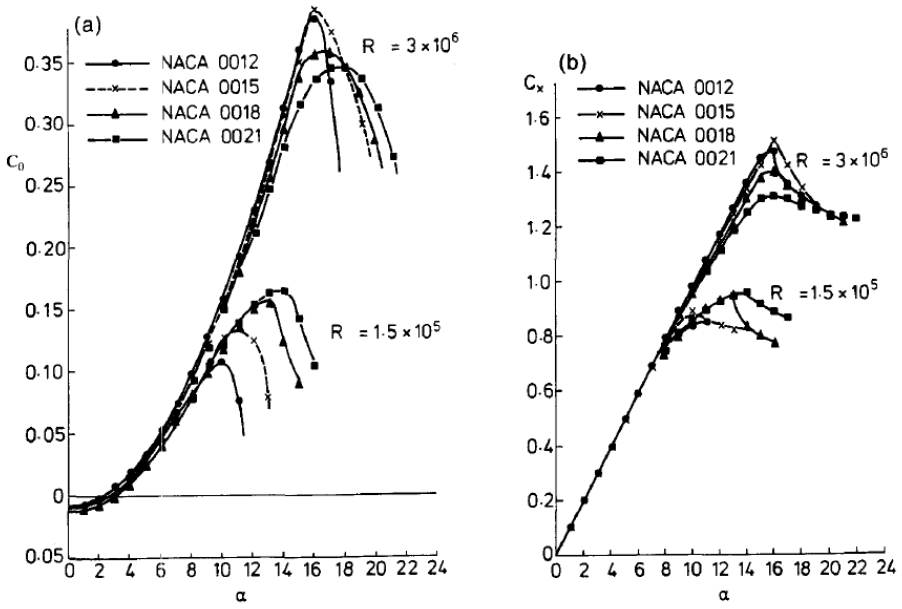

Figure 1.7: Tangential and Axial force coefficients.
From: Raghunathan [5]

The aim of this analysis is to understand the intensity of the forces that develop on the airfoil when subjected to an airflow, as the angle of incidence changes. It is important to analyze both the axial and tangential components of the aerodynamic force generated

on the airfoil because the tangential force, F_t, is responsible for the movement of the rotor blades, while the axial force, F_x, indicates the structural load on the turbine, and consequently the pressure difference between the region before and after the rotor.

The forces developed on the profiles (which depend on the flow) influence the turbine's efficiency, as shown in fig. 1.8: as mentioned before, dealing with waves modeled as sinusoids, the turbine will experience (at the extremes of the operating cycle) both very weak flows and very intense flows.

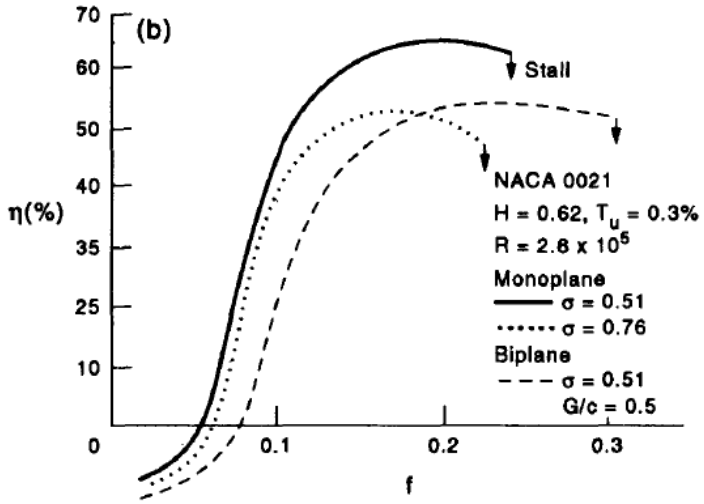

Figure 1.8: Efficiency trend for different flow coefficients.
From: Raghunathan [5]

When airflow rates are low (small angles of airflow incidence), the drag component in the direction of the chord surpasses the lift, resulting in negative efficiencies (total-drag condition). In such cases, the pneumatic power input is transformed into heat, yielding no power output. It's important to note that in these circumstances, unlike traditional turbines, the Wells turbine doesn't function as a pump. Conversely, at higher flow rates (larger incidences), the blade's boundary layer tends to separate (stall), causing a decrease in efficiency.

Furthermore, it should be considered that the operational efficiency of a monoplane rotor is influenced by the shared aerodynamic interactions among its blades, (generation of vortices and induced velocities between adjacent blades). This interaction is determined by the angle at which the airflow meets the blades and the blade solidity.

The trend of normalized coefficients C_t/C_{t0} and C_x/C_{x0} along with the variation of solidity is illustrated in fig. 1.9, where C_{t0} and C_{x0} are measured values of force coefficients of an isolated profile subjected to the same incidence in a wind tunnel.

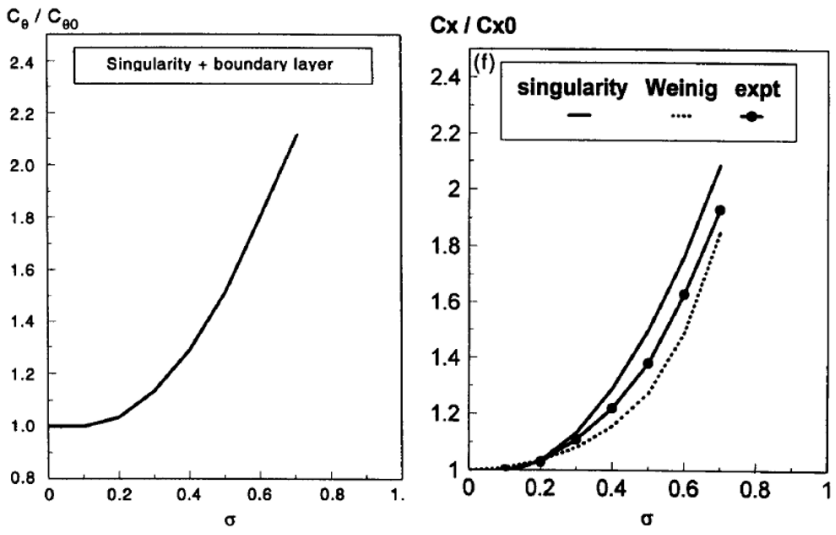

Figure 1.9: The effects of solidity on force coefficients.
From: Raghunathan [5]

1.3.2. Parameters affecting the design of a mono-plane Wells turbine

As previously mentioned, the performance of a Wells turbine is contingent upon the force coefficients, which are, in turn, influenced by several parameters. The subsequent discussion will delve into their impacts on the machine's behavior. Each parameter's influence has been assessed through experiments conducted on a reduced scale [5]. In these experiments, the parameter of interest is varied while keeping the other parameters fixed at suitable values.

- The rotor solidity (σ):
  The turbine's solidity represents the obstruction caused by the turbine to the airflow and also it's an index of the mutual interference between the blades. Observations from experimental data on the average cyclic efficiency reveal that, at low solidity values, the impact of solidity is minor; however, efficiency notably reduces for $\sigma > 0.5$, as shown in fig. 1.10.

  The efficiency reduction in high-solidity Wells turbines is attributed to high kinetic energy losses during the exit phase, linked to the exit swirl. Furthermore, three-dimensional effects may emerge near the hub where closely spaced blades at high solidity could interact with the boundary layer on the hub. These interactions could lead to boundary layer separation on both the hub's surface and the nearby blade surfaces, since blades near the hub experience higher incidence than the blades at

the tip.

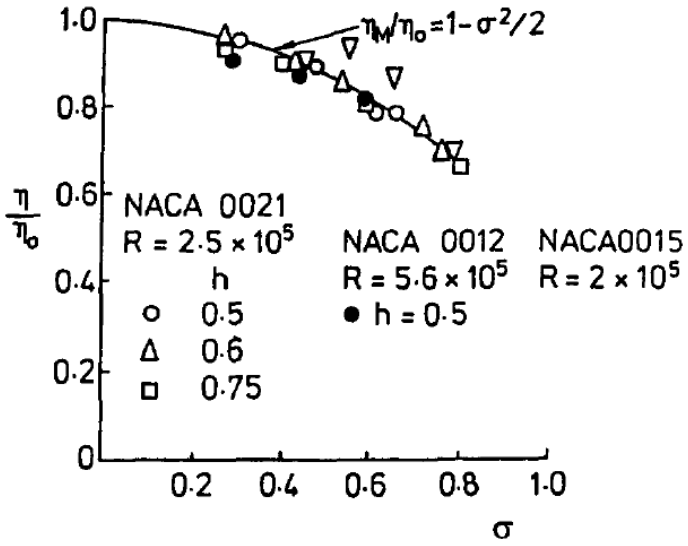

Figure 1.10: The effect of solidity on efficiency.
From: Raghunathan [5]

- The hub-to-tip ratio (h):
  This value influences the airflow's angle of incidence at the hub, the tip clearance losses and the relative interference effects at the hub.

  In the context of a Wells turbine operating at a specific velocity, the angle of incidence at the hub surpasses the one at the tip and rises as the hub-to-tip ratio diminishes. Consequently, a reduction in the hub-to-tip ratio is likely to enhance turbine stall and result in a decline in aerodynamic efficiency.

  Given a specific tip clearance, the hub-to-tip ratio establishes the proportion between tip clearance and blade height. A reduction in h reduces this proportion, potentially curbing tip clearance losses and thus enhancing aerodynamic efficiency. Conversely, a reduction in airflow leakage around the tips leads to decreased relief effects (reduced spanwise flow near the tips) potentially causing blade stall.

  Additionally, the interference effects caused by the hub boundary layer affect aerodynamic efficiency. A reduction in h could mitigate these interference effects, thus elevating efficiency.

  The author [5] suggests to keep the value of h as close as possible to 0.6 as it is the best compromise between all the three discussed effects, since the efficiency peaks at that value as shown in fig. 1.11:

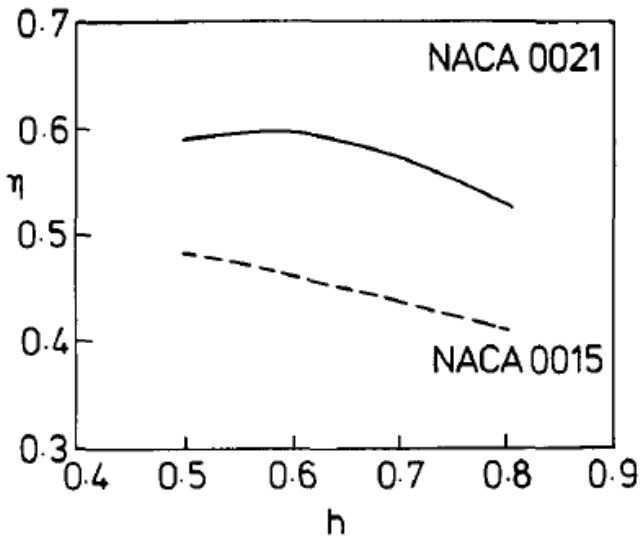

Figure 1.11: The effect of hub-to-tip ratio on efficiency.
From: Raghunathan [5]

- The profile thickness:
  The impact of airfoil thickness cannot be isolated from the Reynolds number effect. Experiments demonstrate that reduced thickness tends to enhance efficiency, but it can be detrimental to self-starting capabilities. Conversely, for thicker airfoils, the opposite trend is observed, where they are advantageous for self-starting but may hinder efficiency, as shown in fig. 1.12:

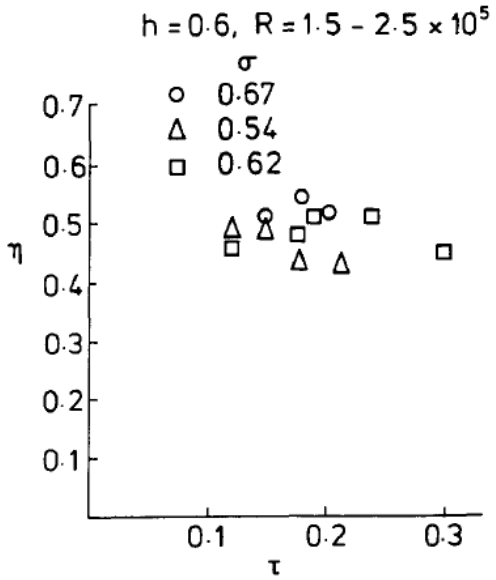

Figure 1.12: The effect of profile thickness on efficiency.
From: Raghunathan [5]

- The aspect ratio (AR):
  The aspect ratio, AR, impacts the efficiency of the turbine and the flow ratio at which the turbine experiences stall. Decreasing the aspect ratio primarily leads to higher efficiencies by delaying stall. This delay is linked to the 'relief effect' on the blades, resulting from a relatively higher mass flow through the tip. Lowering the aspect ratio strengthens tip vortices. Additionally, it's noted that the influence of aspect ratio becomes more prominent as tip clearance increases. An AR value of 0.5 could be considered a suitable choice for a Wells turbine design. The effect of this parameter on efficiency is shown in fig. 1.13:

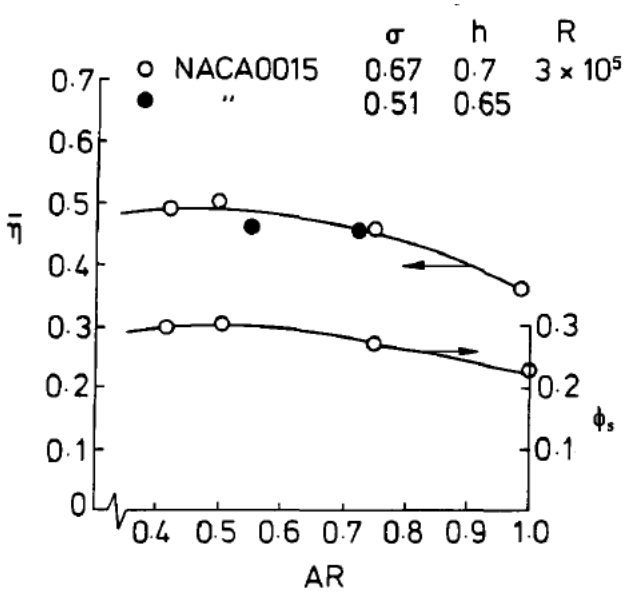

Figure 1.13: The effect of aspect ratio on efficiency.
From: Raghunathan [5]

- The clearance (k):
  The Wells turbine shows high sensitivity to tip clearance. Reducing tip clearance promotes stall advancement but increases the efficiency due to reduced clearance losses. Conversely, turbines with larger tip clearances can operate across a broader range of flow rates without stalling.

  However, values of tip clearance ratio beyond 0.02 do not yield significant advantages. Hence, the author [5] recommends to use tip clearance ratios below 0.02.

  The effect of this parameter on efficiency is shown in fig. 1.14:

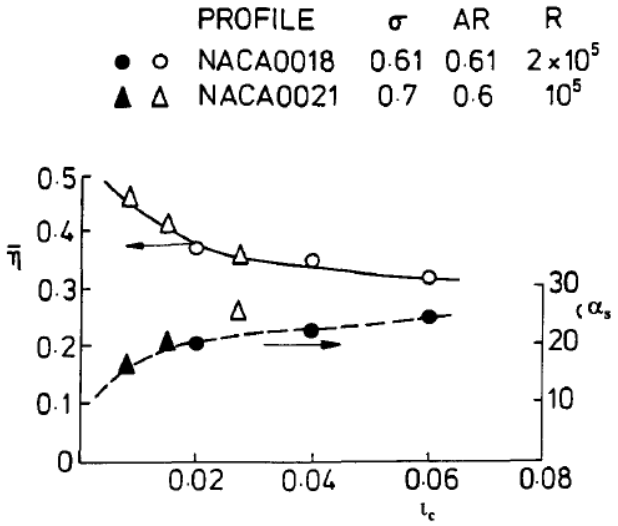

Figure 1.14: The effect of tip clearance on efficiency and stall.
From: Raghunathan [5]

1.3.3. Radial equilibrium

According to the theory of radial equilibrium, the fluid is irrotational, axially symmetric, and its radial velocity component is zero. The pressure field acts opposite to the centripetal acceleration and balances it, preventing the fluid from flowing radially. The Momentum equation in radial direction yields to:

$$\frac{1}{\rho}\frac{\partial P}{\partial r} = \frac{V_t^2}{r} \tag{1.22}$$

2 | The model

In this chapter, a method for modeling the rotor of a Wells turbine is presented, and also a potential new strategy to enhance its performance is discussed. In particular, this chapter outlines the features of this technology and presents all the aspects related to the analytical method developed to describe its functioning. In this way, both the single rotor and the complete configuration of the machine can be tested.

2.1. Model description

2.1.1. General outline

The purpose of this work is to analyze the behaviour of a simple Wells turbine and then to study it after two rows of mobile guide vanes are added upstream and downstream of the rotor, expecting and improvement of the performances.

The model was developed using Fortran 90.

The ultimate goal is to create a real turbine that one day will operate in a real OWC power plant. The OWC design will start from the values (of amplitude and frequency) of the most frequent waves present in the chosen area. The code thus defines the turbine's geometry starting from the selected/imposed OWC data. This way, the turbine will encounter more frequently waves that are optimal for its geometry.

It's important to notice that ocean waves don't have a completely predictable nature, and therefore, using average values is necessary to develop a more reliable analysis, considering that some waves may not be optimal. This is also why attempting to add the two stator rows is interesting: not only to extend the operational range within a single period but also to correct the effects of waves different from the usual ones encountered.

2.1.2. Structure of the code

The code allows the user to choose whether to perform the calculation for the configuration with just the rotor or for the complete machine with the rotor and two stators.

The code takes as input:

- Length (L_{owc}) and Width (Z_{owc}) of the OWC power plant.
- Amplitude (a) and frequency (f) of the wave.
- Turbine parameters (rpm, diameter ratio (h), solidity (σ), number of blades (N_b), stall incidence of the rotor (β_{max}), total-drag incidence of the rotor (β_{min}).
- Inlet air data.

From this data, the code provides:

- The pressure values, the velocity components, and flow angles at each section of the turbine and at every time-step.
- The useful power, the lost power, and efficiency at every time-step.
- The angle of rotation of each stator at each time-step.
- Values of flow angles, velocities, and forces generated at the hub, tip, and midspan sections of one rotor blade.

2.2. Design steps

2.2.1. Evaluation of the OWC parameters

To proceed with the sizing and performance analysis of the Wells turbine, it is necessary to evaluate three parameters of the OWC (see section 1.1.2). These parameters are:

- The OWC surface area (S_{owc}):

$$S_{owc} = L \cdot Z \tag{2.1}$$

  It is a significant parameter when it is related to the surface area of the turbine S_t (not yet evaluated). The smaller the ratio S_t/S_{owc}, the more the air moved by the waves will be accelerated through the OWC structure towards the turbine's inlet section.

- The maximum volumetric flow rate (Q_{max}):

$$Q_{max} = S_{owc} \cdot a \cdot 2\pi \cdot f \tag{2.2}$$

  which, in addition to being a crucial parameter for understanding the maximum velocity that will impact the turbine, serves as the reference value from which the volumetric flow rate q (time-dependent) will be discretized. The time discretization is a crucial aspect of the code's structure, as a significant portion of its framework involves a large loop iterating in this dimension, calculating quantities of interest at each time step.

- The maximum available power (P_a):

$$P_{a\ owc} = \frac{\rho_w \cdot a^2 \cdot Z \cdot 9.81^2}{f \cdot 8\ \pi} \tag{2.3}$$

  This parameter proves to be a valuable indicator of the maximum exploitable power but, in practice, the actual wave potential is lower than the theoretical maximum because not all the available power can be effectively harnessed by the OWC. This discrepancy arises from factors such as wave directionality constraints, internal dissipations, and interactions with the seabed, all of which contribute to a reduction in the power conversion efficiency.

These parameters are evaluated starting from:

OWC dimensions	**Wave data**
$L_{owc} = 3\ [m]$	$a = 2\ [m]$
$Z_{owc} = 3\ [m]$	$f = 0.1\ [Hz]$

Table 2.1: OWC and wave data

2.2.2. Air data

The following air properties data are used as a basis:

Air data	Value
P_{air}	10^5 [Pa]
T_{air}	288 [K]
μ	$1.8 \cdot 10^{-5}[Pa \cdot s]$
R	287 J/kg/K;
γ	1.4 [-]
$\rho = P_{air}/RT_{air}$	1.21 [kg/m^3]

Table 2.2: Air data at the inlet

The initial values of pressure and temperature are chosen based on the following considerations: at the beginning of the operating cycle, the wave has not yet risen and pressurized the OWC chamber (so the pressure is ambient); the air temperature inside the chamber is comparable to the water temperature (the chosen value is a suitable average).

2.2.3. Definition of the turbine geometry

In this phase only the rotor component is considered: the two stator components are just added to it later accordingly to the geometrical constrains.

The turbine's geometry is defined starting from the following assumptions, based on Raghunathan's research [5] (see Section 1.3):

- The turbine rotates at the constant speed of 3000 rpm.
- The hub-to-tip ratio is fixed at the value of $h = 0.6$ as suggested.
- The solidity at midspan is chosen to be $\sigma = 0.4$ in order not to de-rate too much the efficiency.
- The rotor profile is a NACA0015 because of the best trade-off between the range and the tangential force coefficient. Its stall angle is $\beta_{max} = 15$ $[deg]$.
- The turbine blades (unswept) are chosen to be $N_b = 5$ with constant cord.
- The tip clearance is fixed at $k = 1$ $[mm]$

At this point, it is possible to evaluate:

The rotational speed:

$$\omega = 2\pi \frac{rpm}{60} \tag{2.4}$$

The hub diameter:

$$D_h = \sqrt[3]{\frac{8\ Q_{max}\ h^2}{\pi\ \omega\ (1-h^2)\ \tan\left(\beta_{max}\right)}} \tag{2.5}$$

The tip diameter:

$$D_t = \frac{D_h}{h} \tag{2.6}$$

The turbine surface:

$$S_t = \frac{\pi\ D_h^2\ (1-h^2)}{4\ h^2} \tag{2.7}$$

The diameter at midspan:

$$D_m = \frac{D_h + D_t}{2} \tag{2.8}$$

The chord:

$$c = \frac{\pi\ D_m\ \sigma}{N_b} \tag{2.9}$$

The blade height:

$$b = \frac{D_t - D_h}{2} \tag{2.10}$$

At this point, the rotor geometry is fully defined:

Lenght	**Value [m]**	**Lenght**	**Value [m]**
D_h	0.577	c	0.193
D_m	0.770	b	0.192
D_t	0.962	τ_{max}	0.028

Table 2.3: Rotor dimensions

2.2.4. Verification of Reynolds and Mach numbers

It is necessary to analyze the values of the Reynolds number and the Mach number.

The Reynolds number is evaluated at the hub (where it has the lowest value); it is necessary to ensure that the value of the Reynolds number is greater than 10^5 to consider the analysis valid, as it relies on the performance curves presented in Raghunathan's work [5], which were developed for a certain range of Reynolds numbers.

The maximum (at the tip) Mach number is evaluated just to confirm the subsonic regime on the whole domain.

In order to evaluate the Reynolds number

$$Re = \frac{\rho\, W_{1h}\, c}{\mu} \tag{2.11}$$

and the Mach number:

$$Ma = \frac{W_{1t}}{\sqrt{\gamma\, R\, T_{air}}} \tag{2.12}$$

it is necessary to evaluate:

- The maximum axial (absolute) velocity:

$$V_x = \frac{Q_{max}}{S_t} \tag{2.13}$$

- The relative inlet velocity at the hub:

$$W_{1h} = \sqrt{V_x^2 + \left(\omega\, \frac{D_h}{2}\right)^2} \tag{2.14}$$

- The relative inlet velocity at the tip:

$$W_{1t} = \sqrt{V_x^2 + \left(\omega\, \frac{D_t}{2}\right)^2} \tag{2.15}$$

2.2.5. Discretization of the time domain

A Wells turbine operates in a symmetrical manner. During the period in which a wave rises and falls, the turbine encounters a flow rate that follows a sinusoidal law, as described in fig. 2.1.

The flow rate is zero when the wave reaches its minimum and maximum heights, and it is maximum when the wave is at its midpoint.

At the points where the flow rate is maximum and minimum, the regions affected by stall and total-drag phenomena are located.

During the passage of a wave, the behavior of the flow rate can be divided into four intervals, between the values of minimum and maximum flow rate. Therefore, it is sufficient to analyze what happens during 1/4 of the period.

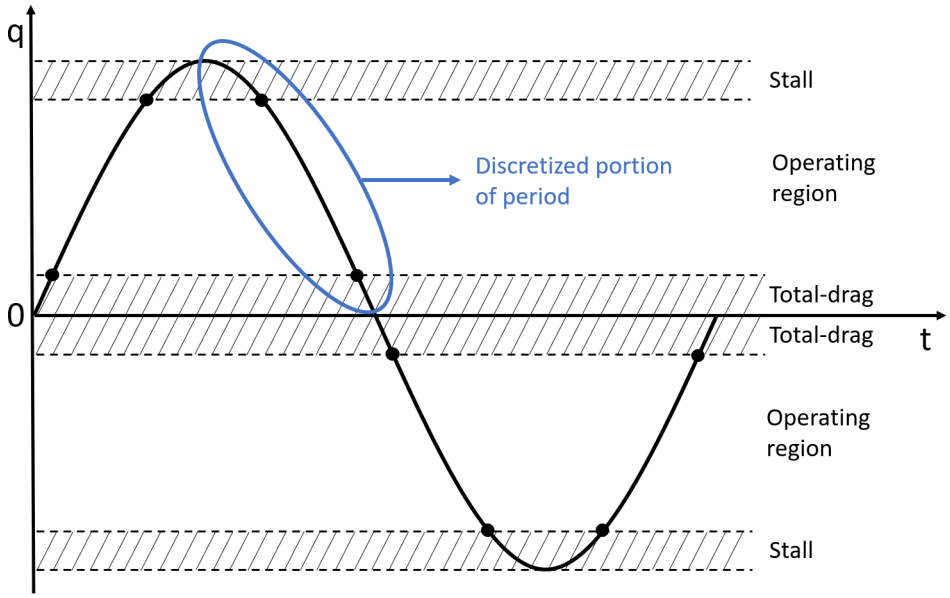

Figure 2.1: Flow rate behaviour during a wave cycle.

The portion of the period under consideration is discretized into a sufficient number of time steps (N_t). Considering the counter i marching from 1 to $N_t + 1$, the time step is:

$$t = \frac{1}{4\ f}\ \frac{i-1}{N_t} \tag{2.16}$$

At this point, it is possible to evaluate the flow rate at each time step. The calculated flow rate values form a vector [q], with its elements arranged in descending order from Q_{max} to Q_{min}.

$$q_i = Q_{max}\ \cos\left(2\ \pi\ f\ t\right) \tag{2.17}$$

The main structure of the code consists of a large time-iterative loop. At each iteration, all the quantities of interest fot the specific time step are calculated starting from the i-th element of the vector [q], so that the behaviour of the turbine receiving a certain flow rate is known.

2.2.6. Discretization of the spatial domain

In addition to the temporal discretization, a spatial discretization is also performed to analyze how the various quantities behave along the span of the blades more effectively.

In particular, a certain number of equidistant points ($N_p + 1$) are distributed along the

length of the blade, delineating the intervals into which the blade is divided (N_p intervals), as shown in fig. 2.2:

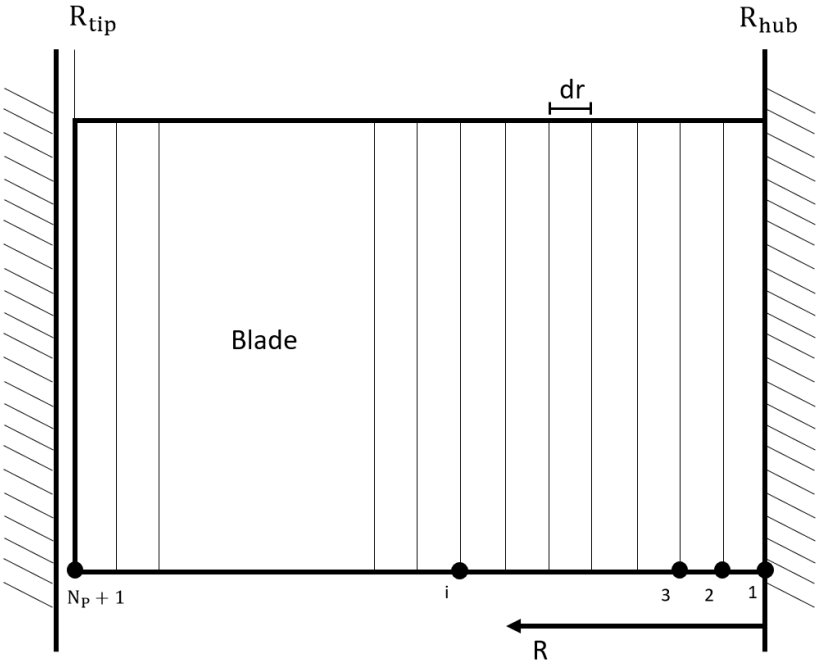

Figure 2.2: Blade discretization.

Just like for the time, considering the counter i marching from 1 to $N_p + 1$, each value of the diameter is collected into a vector:

$$d_i = D_h + (D_t - D_h)\,\frac{i-1}{N_p} \tag{2.18}$$

Velocity triangles are radial-dependent. Each section of the blade has a different angle of incidence (the highest is at the hub) and sees a different velocity (the highest is at the tip).

This type of discretization is needed to perform a stream tube analysis, more accurate than an analysis based on average values on the whole blade: the integral values of the forces acting on the blade are more precise, as long as the evaluation of losses and the variation of all quantities of interest along the radial direction.

2.2.7. Iteration cycles

Once the turbine geometry has been defined and the vectors [q] and [d] have been created, all the elements required to perform the calculations are available.

The main structure of the code consists of two major iterative loops: an outer loop iterating over time, and an inner loop iterating over space. In this way, for each iteration of the outer loop (for each flow rate value), all quantities are calculated within each of the stream tubes into which the blade is discretized.

At this point, the first iterative cycle starts, and the inlet velocity, which is axial, is immediately calculated.

$$V_x = \frac{q_j}{S_t} \tag{2.19}$$

This component of the Absolute velocity is assumed to be constant along the axial direction since the Wells turbine is an axial turbine.

Also, the total-pressure at the inlet section is evaluated:

$$P_t = P_{atm} + \frac{1}{2}\,\rho\,V_x^2 \tag{2.20}$$

At this point all the quantities at the inlet section are known.

2.2.8. Analysis of the rotor

The analysis of the rotor, located between sections 1 and 2, occurs in the internal cycle, where each spatial iteration analyzes what happens within a single interval of a rotor blade.

At each time step, starting from the velocity triangle, the forces acting on each section of the blade and the associated powers are calculated. In the end, all these quantities are integrated over the length of the blade (and multiplied for the number of blades) to determine the overall performance of the machine in terms of useful power, lost power, and efficiency at each time step.

Velocity triangles before the rotor

All the information needed to evaluate the velocity triangles upstream of the rotor is available.

On each blade interval into which the rotor is divided, a different velocity triangle acts.

In fact, the i-th portion of the rotor blade rotates at the Peripheral velocity of:

$$U = \omega \, \frac{d_i}{2} \tag{2.21}$$

Due to this, the angle of incidence of each section is different, since is U-dependant:

$$\beta_1 = \arctan\left(\frac{V_x}{U - V_{1t}}\right) \tag{2.22}$$

The same applies to the Relative velocity:

$$W_1 = \sqrt{(U - V_{1t})^2 + V_x^2} \tag{2.23}$$

In particular, near the hub,there are higher incidences and lower velocities, while near the tip there are lower incidences and higher velocities, as shown qualitatively in fig. 2.3

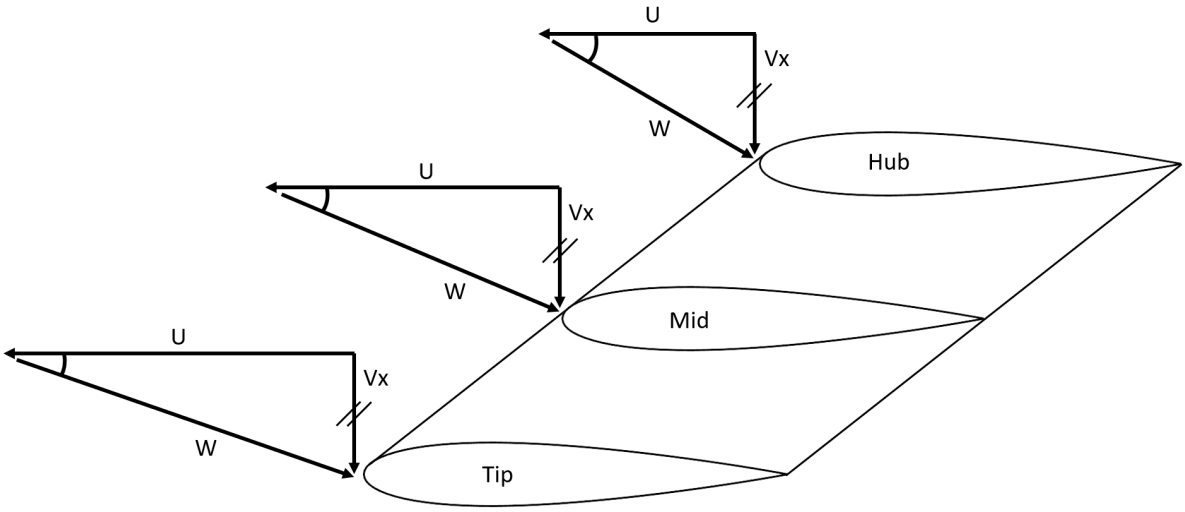

Figure 2.3: Velocity triangles upstream the rotor.

The rotor solidity

Another quantity that varies with the radial position is solidity, that is calculated as:

$$\sigma = \frac{c \, N_b}{2 \, \pi \, dr_{up}} \tag{2.24}$$

where dr_{up} is a variable that represents the radius update: starting from the initial value of $Dh/2$ (hub) a dr is added at each iteration of the internal cycle completing the entire span of the blade up to $Dt/2$ (tip).

Force coefficients

The next step is to calculate the forces acting on each blade interval, which allows later to evaluate the machine's performances and calculate the downstream quantities.

The components of the force (F) acting on a blade interval with thickness dr are:

$$F_x = \frac{1}{2}\,\rho\, W_1^2\, c\, C_x\, rC_x\, dr \quad (axial) \tag{2.25}$$

$$F_t = \frac{1}{2}\,\rho\, W_1^2\, c\, C_t\, rC_t\, dr \quad (tangential) \tag{2.26}$$

In detail, C_x and C_t are the coefficients of axial and tangential force acting on a single profile, and they are known from the studies of Raghunathan [5]. Their trend versus the incidence angle is shown in fig. 1.7 in section 1.3 of this work.

Both functions of C_x and C_t are reconstructed pointwise and approximated with a polynomial function:

- For C_x, it is sufficient to use a first-order polynomial with the coefficients:

Coefficient	Value
$B0$	0
$B1$	0.097

Table 2.4: Coefficients of the polynomial approximating C_x

- For C_t, it is used a second-order polynomial with the coefficients:

Coefficient	Value
$C0$	-0.015
$C1$	0
$C2$	0.0016

Table 2.5: Coefficients of the polynomial approximating C_t

The two coefficients are then calculated as:

$$C_x = B1\ \beta_1 \tag{2.27}$$

$$C_t = C2\ \beta_1^2 + C0 \tag{2.28}$$

Furthermore, $rC_x = C_x/C_{x0}$ and $rC_t = C_t/C_{t0}$ are corrective coefficients that take into account the dependence of force coefficients on solidity, which is different at each blade section. The dependence on solidity, analyzed by Raghunathan [5], is shown in fig. 1.9 in section 1.3 of this work.

In this case as well, to evaluate these quantities a polynomial approximation (second order) is used:

$$rC_x = D2\ \sigma^2 + D1\ \sigma + D0 \tag{2.29}$$

$$rC_t = E2\ \sigma^2 + E1\ \sigma + E0 \tag{2.30}$$

Where:

Coefficient	Value	Coefficient	Value
D0	1.0106	E0	1.0054
D1	-0.4247	E1	-0.4042
D2	2.4851	E2	2.8274

Table 2.6: Coefficients of the polynomial approximating rC_x and rC_t

In this way, at each temporal step of the outer cycle, the series of iterations of the inner cycle is completed, calculating the axial and tangential force components on each blade interval.

Velocity triangles after the rotor

The quantities downstream of the rotor are calculated starting from the Euler work. First of all, for each blade interval, the tangential component of the Absolute velocity:

$$V_{2t} = -\frac{F_t}{\rho\ \frac{q(j)}{N_b\ n_p}} + V_{1t} \tag{2.31}$$

Then are evaluated the outlet angle,

$$\beta_2 = \arctan\left(\frac{V_x}{U - V_{2t}}\right) \tag{2.32}$$

and the Relative velocity:

$$W_2 = \frac{V_x}{sin(\beta_2)} \tag{2.33}$$

The issue with this method is that it proves to be unreliable in evaluating quantities when the turbine is in total-drag conditions since, for purely analytical reasons, it provides results that are senseless. In fact, the tangential force (numerator) and the flow rate (denominator) both tend toward zero in total-drag conditions, and the value of V_{2t} in the final iterations shows unrealistic values. For this reason, at this stage of the cycle, the quantities are calculated based on the relative total pressure reduction:

$$W_2 = \sqrt{W_1^2 + 2\,\frac{F_x}{\rho\,\frac{S_t}{Nb\;np}}} \tag{2.34}$$

$$\beta_2 = \arcsin\left(\frac{V_x}{W_2}\right) \tag{2.35}$$

$$V_{2t} = -W_2\ \cos(\beta 2) + U \tag{2.36}$$

At this point, the velocity triangles downstream of the rotor are known, and it is possible to move on to the evaluation of the losses associated with it.

Losses related to the rotor

The losses associated with the rotor are profile losses and clearance losses.

To assess profile losses, the drag force acting on a blade interval is calculated based on the axial and tangential force components acting on it:

$$D = \frac{F_x\ \tan(\beta_1) - F_t}{\tan(\beta_1)\ \sin(\beta_1) + \cos(\beta_1)} \tag{2.37}$$

Clearance losses are conventionally calculated using the Dunham & Came correlation [10] (using the quantities evaluated at the midspan), where the secondary-flows contribute is not considered since the rotor blades do not form a channel in which secondary flows can

develop.

$$Y_c = \frac{c}{b}\, B \left(\frac{k}{c}\right)^{0.78} \left(\frac{c_L}{1/\sigma}\right)^2 \frac{\cos\left(\beta_2\right)^2}{\left(\cos\left(\beta_m\right)\right)^3} \tag{2.38}$$

Where the lift coefficient is:

$$c_L = 2\,\frac{1}{\sigma} |\tan\left(\beta_1\right) - \tan\left(\beta_2\right)|\ \cos\left(\beta_m\right) \tag{2.39}$$

and the mean angle is:

$$\beta_m = \arctan\left(\frac{\tan\left(\beta_1\right) + \tan\left(\beta_2\right)}{2}\right) \tag{2.40}$$

This correlation returns the integral value of Y_c, but there is radial dependence, meaning these losses have a different effect on each interval.

To account for this, Y_c is assumed to have a linear distribution along the blade, with the highest value at the tip and decreasing to 0 at the midspan, as shown in fig. 2.4:

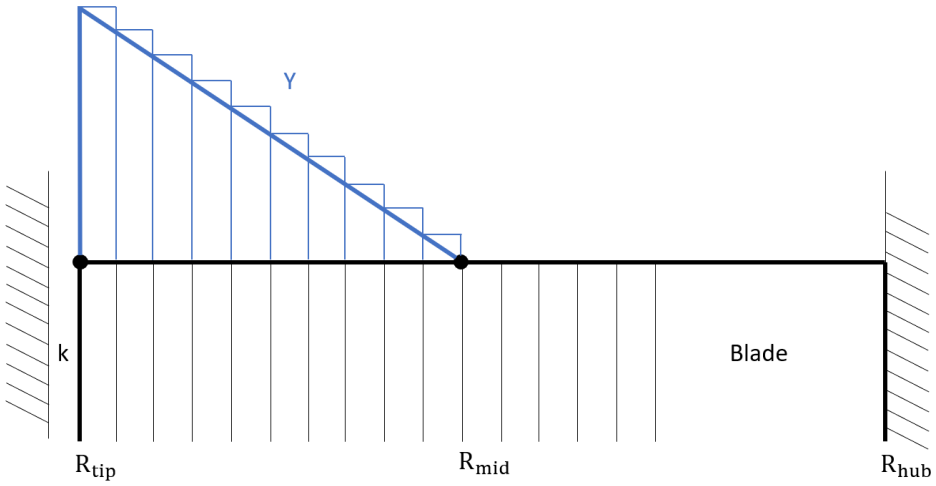

Figure 2.4: Contributes of the clearance losses on a rotor blade

The maximum value of Y_c is at the tip:

$$Y_{c\,max} = \frac{4\,Y_c}{b} \tag{2.41}$$

The i-th contribution on the intervals after the midspan is:

$$Y_{c\,i} = (\frac{2\,Y_{c\,max}}{b})\;(i - 1 - \frac{n_p}{2})\;dr \tag{2.42}$$

There is no contribution on the intervals before the midspan.

The clearance losses result in an increase in Drag. On each blade interval, the axial force F_x undergoes an increase due to clearance, given by:

$$\Delta F_x = Y_{c\,i}\;\frac{1}{2}\;\rho W_1^2\;c\;dr \tag{2.43}$$

which is added to F_x in the drag calculation.

Global values

Everything needed is available to calculate quantities related to one timestep:

- The total axial force acting on the rotor:

$$F_{x\,tot} = N_b \sum_{i=1}^{n_{p+1}} (F_{x\,i}) \tag{2.44}$$

- The total tangential force acting on the rotor:

$$F_{t\,tot} = N_b \sum_{i=1}^{n_{p+1}} (F_{t\,i}) \tag{2.45}$$

- The useful power:

$$P_{use} = N_b \sum_{i=1}^{n_{p+1}} (F_{t\,i}\;U_i) \tag{2.46}$$

- The lost power:

$$P_{lost} = N_b \sum_{i=1}^{n_{p+1}} (D_i\;W_{1\,i}) \tag{2.47}$$

Pressure evaluation after the rotor

The static pressure difference across the rotor is known:

$$\Delta P = \frac{F_{x\,tot}}{S_t} \tag{2.48}$$

and from here, the static pressure at section 2:

$$P_2 = P_1 - \Delta P \tag{2.49}$$

Downstream of the rotor, each blade interval has a different velocity triangle. To calculate a total-pressure value that is representative of section 2, it is necessary to consider a velocity triangle exiting the rotor with average values.

Thanks to Euler work, it is possible to evaluate V_{2t}:

$$V_{2t} = -\frac{F_{t\,tot}}{\rho\, q(j)} + V_{1t} \tag{2.50}$$

It is an average value used as before to calculate V_2 (and β_2, W_2) and, with it, the total-pressure:

$$P_{t2} = P_2 + \frac{1}{2}\,\rho\, V_2^2 \tag{2.51}$$

Radial equilibrium

At this point, a check on radial equilibrium is also performed to assess the pressure gradient developing radially along the rotor blade:

$$P_{tip} - P_{hub} = \rho\, V_{2t}^2\, \ln\left(\frac{D_t}{D_h}\right) \tag{2.52}$$

Losses related to kinetic energy

The last source of losses that remains to be evaluated is related to the kinetic energy of the air flow after the rotor.

The lost power due to it is

$$P_{kin} = \rho\, q(j)\, \frac{V_2^2}{2} \tag{2.53}$$

Efficiency evaluation

At each timestep, the efficiency is determined by the ratio of useful power output to the total power available in the airflow passing through the turbine:

$$\eta = \frac{P_{use}}{P_{use} + P_{kin} + P_{lost}} \tag{2.54}$$

It's important to note that during the total-drag condition, the tangential force F_t (and consequently P_{use}) are negative. Because of this, for analytical reasons, efficiency takes on a negative value.

Physically, it makes sense to consider the efficiency equal to zero during that phase of the period because the turbine is not producing power, and it's moving only due to inertia.

Overall quantities

The useful power produced during the period is obtained by summing the contributions of power produced at each time step. Since it is a time-varying quantity, it is good to assess that the useful power produced by the turbine is the average value over the period:

$$P_{use\,tot} = \frac{\sum_{j=1}^{n_{p-1}} (P_{use\,j})}{n_p} \tag{2.55}$$

The plant's efficiency is finally assessed by comparing the integral value of the turbine's useful power with the available power from the OWC:

$$\eta_{overall} = \frac{P_{use\,tot}}{P_{a\,owc}} \tag{2.56}$$

At this point, the part of the model that allows analyzing the rotor's behavior is concluded.

2.3. Addition of VIGV

The idea is to add two rows of stator blades, one upstream and one downstream of the rotor as shown in fig. 2.5. The key feature of these two blade sets is their ability to adjust their angle of incidence relative to the oncoming airflow through a control law.

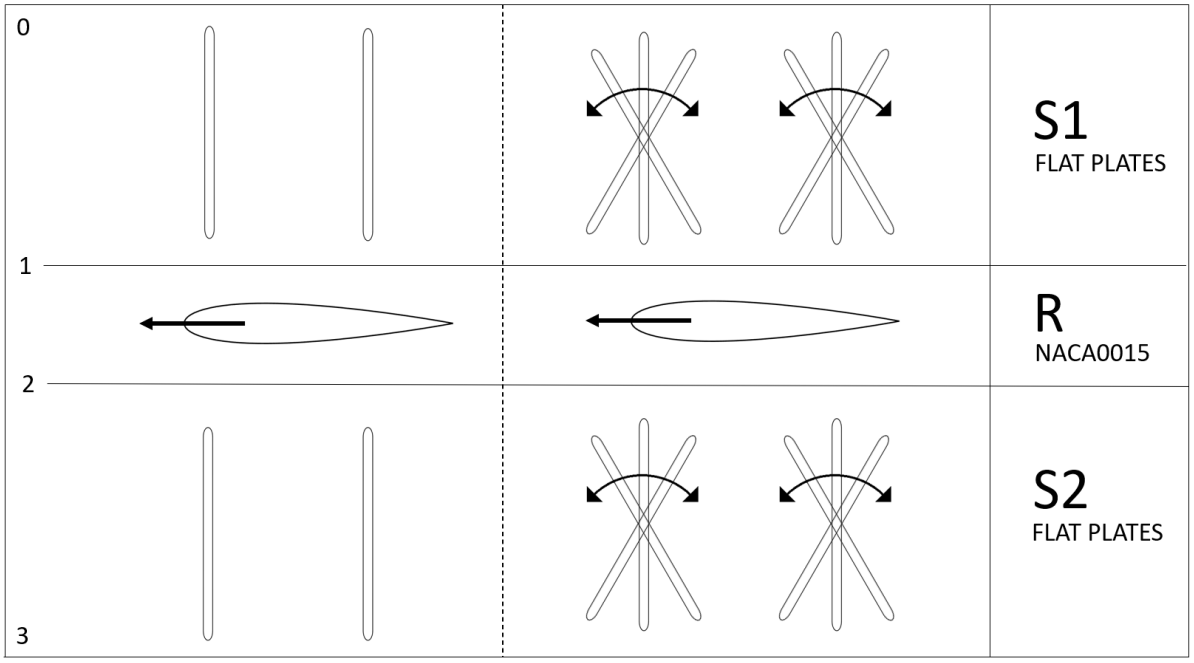

Figure 2.5: Structure of the turbine with the addition of the upstream and the downstream stators.

The primary role of the upstream stator (S1) is to receive the airflow and redirect it toward the rotor (R) with improved characteristics. The purpose of this component is to prevent a potential stall of the rotor and to minimize the total drag condition as much as possible, recognizing that this condition cannot be entirely eliminated.

For what concerns the downstream stator (S2), its purpose is to minimize the kinetic energy of the flow at the machine's exit.

Since the turbine is integrated into an OWC system, as mentioned earlier, air flows through it first in one direction and then in the other. Therefore, it is essential for the problem to be symmetric: the two rows of stationary stator blades must be identical. Indeed, one set of blades must perform its role during the first operative cycle, but when the cycle reverses, it must act like the other one.

Considering all these aspects, it is possible to see a qualitative representation of the whole

turbine in fig. 2.6:

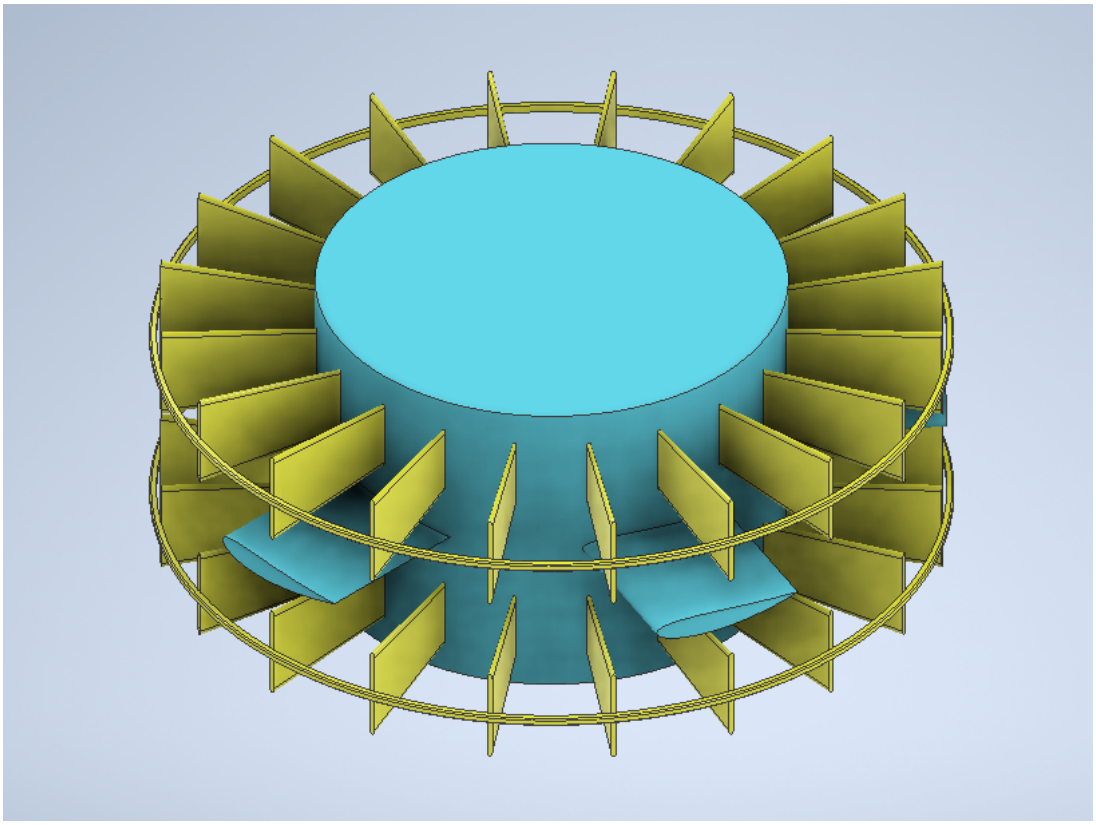

Figure 2.6: Qualitative visualization of the Wells turbine with two rows of VIGV

2.3.1. About the stators

The geometry of the stators must be chosen consistently with the rotor geometry. They are just added to the rotor to improve its performance, so parameters such as diameters and blade length must be the same. The parameters not constrained by the rotor's geometry include blade geometry (which must still be symmetric) and two of the following: the number of blades, chord, and solidity. To minimize the losses generated by the stators, flat plates are used for the following reasons:

- The two rows of stators only need to deflect to correct critical conditions during the operational cycle; the rest of the time they are at zero incidence, and with an almost negligible drag coefficient in that condition they do not introduce significant losses to the machine.
- A row of flat plates can deflect by considerable angles before the profile losses increase too much; for the stators, a maximum rotation is imposed to ensure this phenomenon does not occur.

- When the wave reverses its motion, and the two stators have to swap their roles, the flat plates should not undergo particularly high rotations on themselves since the leading and trailing edges are the same.

In this context, it is beneficial to reference the work of Coppinger & Swain [11]. Their study focuses on a variable inlet guide vane system (VIGV) positioned upstream of a compressor, analyzing their performance and losses as the angle of incidence varies, proceeding from the work of Handel [12]. Other studies about FP/VIGV are [13], [14], [15] and especially the work performed by Frank (et al.) [16], since it contains a loss analys analogue to [11]. With these studies, it is possible to draw some analogies for the case under consideration in this work.

The VIGV system by Coppinger is structured in such a way as to enhance the performance of a radial compressor. As seen in fig. 2.7, it is a system with eight blades positioned to maintain a constant solidity equal to 1.

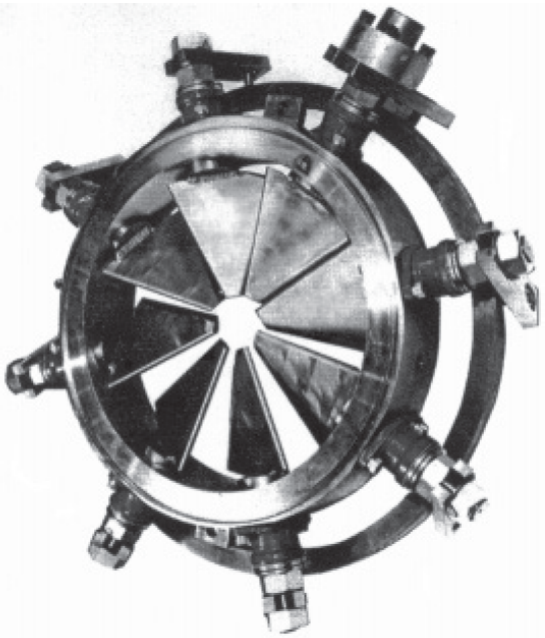

Figure 2.7: VIGV system, From Coppinger [11]

In order to adapt the Coppinger model to the Wells turbine featured in this study, several considerations and modifications are necessary. Coppinger blades are attached to the casing and point towards the shaft of the machine; the ratio between the hub diameter and tip diameter is very low, and as a result, the blades end with a very small chord, almost pointed.

If one wishes to implement a VIGV system similar to that for a Wells turbine, where the ratio between diameters is significantly higher (the shaft is very wide), the blades must be increased in number to achieve a small chord near the hub; a small number of blades would have higher chord near the hub and this would cause a larger clearance near the hub.

So the following parameters are chosen:

- Number of blades: $N_b = 20$
- Solidity: $\sigma = 1$

Considering the reference geometry of the rotor (see Subsection 2.2.3), the stators can have the following dimensions:

Lenght	**Value [m]**	**Lenght**	**Value [m]**
D_h	0.577	c_h	0.09
D_m	0.770	c_t	0.12
D_t	0.962	c_t	0.15
b	0.192	τ	0.005

Table 2.7: Stator dimensions

In fig. 2.8 a qualitative representation of the sized VIGV system is shown:

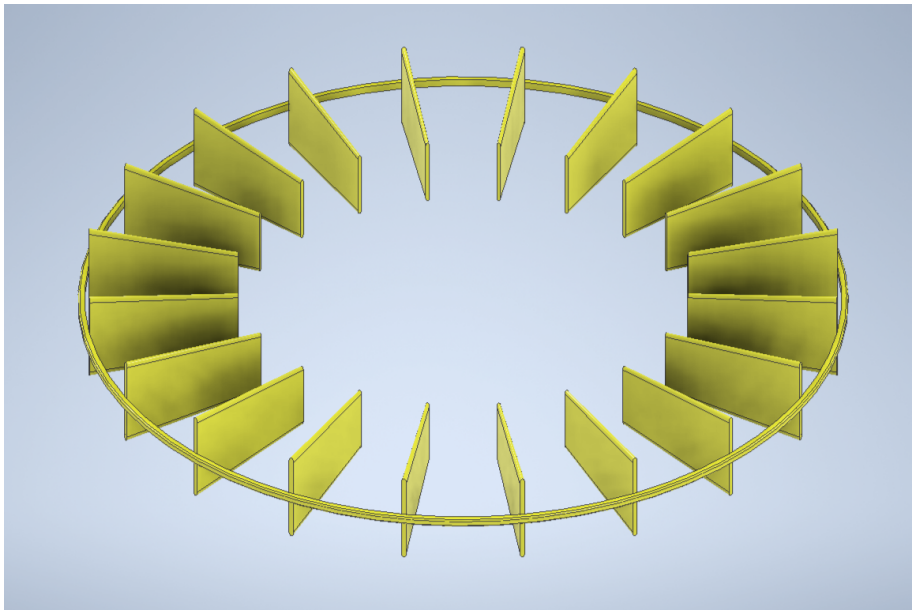

Figure 2.8: Qualitative visualization of the sized VIGV

2.3.2. The upstream stator control law

As previously mentioned, the purpose of the first stator is to receive the airflow generated by the oscillation of the waves and redirect it optimally towards the rotor.

The control law defining the stator adjustment must prevent the airflow from being discharged onto the rotor at angles greater than the stall angle or less than the total-drag angle, and also avoiding that the stator itself is involved in a stall phenomenon.

The result of applying this control law is to assign a tangential component (V_{1t}) to the absolute velocity V (which, when it impacts the machine, has only an axial component V_x, known), to correct the velocity triangle on the rotor.

The limits within which the control law operates are:

- The stall angle of the rotor: according to the studies by Raghunathan [5], for a flow field characterized by a Reynolds number on the order of 10^6, the stall angle for a NACA0015 profile is $\beta_{max} = 15$ [deg]. This angle was also used to define the turbine's geometry.
- The total drag angle: this angle was defined performing calculations on the "rotor-only" configuration. When the airflow impacts the rotor at an angle lower than $\beta_{min} = 5$ [deg], the tangential force coefficient C_t becomes too low and then also negative, and the turbine enters the total-drag condition.
- The stator's maximum deflection angle: analyzing the results of the study of Coppinger & Swain [11], a row of flat plates exposed to an airflow starts to generate a significant total-pressure losses if it is inclined at angles greater than $\theta = 30$ [deg], but they can be turned up to $\theta = 60$ [deg] before critical phenomena (such as blockage) happens.

Stall correction

To prevent the rotor from stalling, it is necessary to control the region of the blade that stalls first among the others: the hub, where the incidence is higher than at any other point, since there the Peripheral velocity (U) has the lowest value.

For each flow rate value, the angle of incidence at the hub is then calculated:

$$\beta_{1hub} = \arctan\left(\frac{V_x}{U_{hub}}\right) \qquad \left(where \;\; U_{hub} = \omega \, \frac{D_h}{2}\right) \tag{2.57}$$

If this angle is greater than the stall angle of the rotor, the stator is set to rotate by:

$$\theta_{S1} = \arctan\left(\frac{V_{1t}}{V_x}\right) \qquad (< 0) \tag{2.58}$$

where the tangential component of the Absolute velocity, wich is imposed, is:

$$V_{1t} = \omega\,\frac{D_h}{2} - \frac{V_x}{\tan\left(\beta_{max}\right)} \qquad (< 0\ ,\ \text{opposed to U}) \tag{2.59}$$

and the Absolute velocity is:

$$V_1 = \sqrt{V_x^2 + V_{1t}^2} \tag{2.60}$$

This angle coincides with the angle of incidence of the stator itself, as the airflow arrives with only an axial component, V_x. For the same reason, the upstream stator has no radial dependence: every section of the stator blade has the same incidence.

This way, the angle of attack on the rotor is reduced by a sufficient amount to prevent it from stalling. The result of this control law is depicted in fig. 2.9:

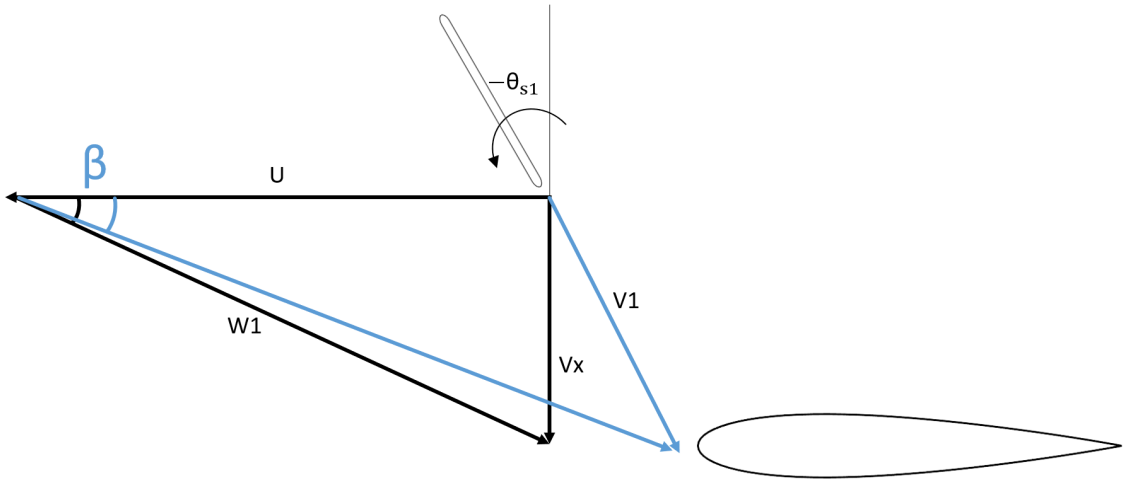

Figure 2.9: S1: Stall control

The rotation angle is imposed to never be greater than θ_{max}, to avoid to increase too much the losses related to the upstream stator.

Minimum incidence verification

While controlling the incidence at the hub to reduce the angle of incidence on the whole rotor blade, it is necessary to ensure that the blade tip has not been brought into total-drag condition.

The tip is the location where the incidence is the lowest, and potentially there could be the risk to send it below the angle β_{min}.

This must be avoided, as the final part of the blade is the one that sustains the major loads and is responsible for the majority of the power produced.

Therefore, a check is performed on the angle at the tip:

$$\beta_{1tip\ check} = \arctan\left(\frac{V_x}{\omega\ \frac{D_t}{2} - V_{1t}}\right) \tag{2.61}$$

If this angle is less than β_{min}, then the following quantities are redefined:

$$\theta_{S1} = \arccos\left(\frac{V_x}{\sqrt{V_x^2 + \left(\omega\ \frac{D_t}{2} - \frac{V_x}{\tan(\beta_{min})}\right)^2}}\right) \tag{2.62}$$

which is the stator maximum deflection that ensures an incidence of β_{min} on the rotor tip: if θ_{S1} is higher than this value, the tip enters the total-drag condition.

$$V_{1t} = V_x\ \tan\left(\theta_{S1}\right) \tag{2.63}$$

$$V_1 = \sqrt{(V_x^2 + V_{1t}^2)} \tag{2.64}$$

Total-drag correction

To prevent the rotor from entering the total-drag condition, it is necessary to control the region of the blade that is subject to the lowest incidence among the others: the tip, since there the Peripheral velocity (U) has the highest value.

For each flow rate value, the angle of incidence at the tip is then calculated:

$$\beta_{1tip} = \arctan\left(\frac{V_x}{U_{tip}}\right) \qquad \left(where\ \ U_{tip} = \omega\ \frac{D_t}{2}\right) \tag{2.65}$$

If this angle is lower than the total-drag angle of the rotor, the stator is set to rotate by:

$$\theta_{S1} = \arctan\left(\frac{V_{1t}}{V_x}\right) \qquad (> 0) \tag{2.66}$$

where the tangential component of the Absolute velocity, wich is imposed, is:

$$V_{1t} = \omega \frac{D_t}{2} - \frac{V_x}{\tan(\beta_{min})} \qquad (> 0\ ,\ \text{directed as U}) \tag{2.67}$$

and the Absolute velocity is:

$$V_1 = \sqrt{V_x^2 + V_{1t}^2} \tag{2.68}$$

This way, the angle of attack on the rotor is increased by a sufficient amount to prevent it from be in total-drag, remembering that this condition can't be avoided completely on the whole period, but only postponed or corrected.

The result of this control law is depicted in fig. 2.10:

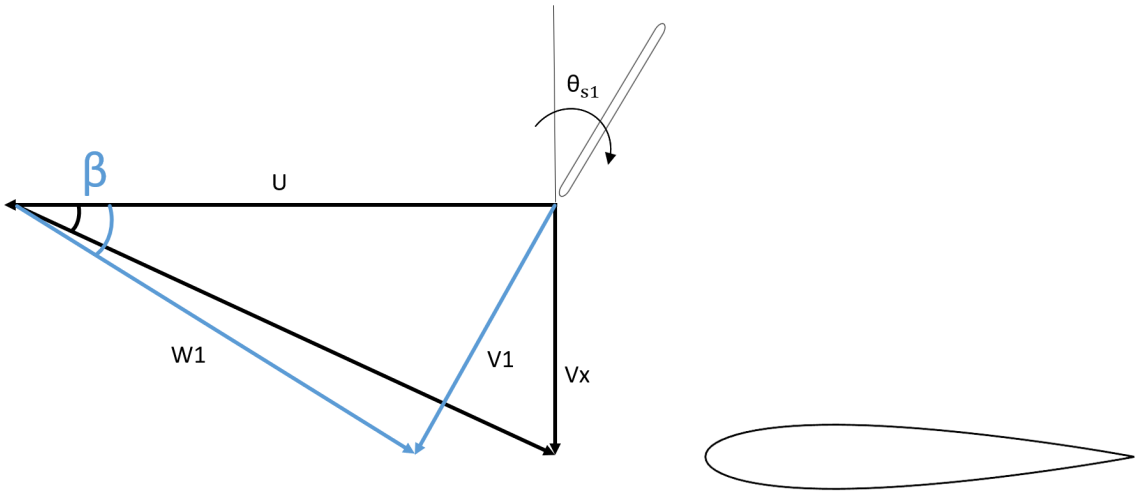

Figure 2.10: S1: Total-drag control

(Note: actually, the rotor goes into total drag for a $\beta_{min} < 3$, but a slightly higher angle has been set as β_{min} to increase the power extraction by the rotor in that period phase where the speed is very low.)

Maximum incidence verification

While controlling the incidence at the tip to increase the angle of incidence on the whole rotor blade, it is necessary to ensure that the hub has not been brought into stall condition.

This situation is not as critical as the one before: the crucial thing is that the tip goes into total-drag as late as possible, even at the cost of stalling the hub. In any case, it is better to try to avoid both situations, so the check is still performed.

The hub is the location where the incidence is the highest, and potentially there could be the risk to send it above the angle β_{max}.

Therefore, a check is performed on the angle at the tip:

$$\beta_{1hub\ check} = \arctan\left(\frac{V_x}{\omega\ \frac{D_h}{2} - V_{1t}}\right) \tag{2.69}$$

If this angle is greater than β_{max}, then the following quantities are redefined:

$$\theta_{S1} = \arccos\left(\frac{V_x}{\sqrt{V_x^2 + \left(\omega\ \frac{D_h}{2} - \frac{V_x}{\tan(\beta_{max})}\right)^2}}\right) \tag{2.70}$$

which is the stator minimum deflection that ensures an incidence of β_{max} on the rotor hub: if θ_{S1} is lower than this value, the hub enters the stall condition.

$$V_{1t} = V_x\ \tan\left(\theta_{S1}\right) \tag{2.71}$$

$$V_1 = \sqrt{(V_x^2 + V_{1t}^2)} \tag{2.72}$$

The main phase of the operative cycle

During the main phase of the operating cycle, where there are no phenomena to correct, the stator has zero incidence and does not modify the flow direction. Therefore, the main outputs of the control law are set to the value:

- $\theta_{S1} = 0$
- $V_{1t} = 0$

- $V_1 = V_x$

The next step is to analyze the losses related to the upstream stator.

2.3.3. Losses related to the upstream stator

While the upstream stator is introduced to enhance machine performance, it is also a source of losses, notably profile losses and clearance and secondary flows losses.

The assessment of losses related to the upstream stator relies on calculating the Total-pressure loss coefficient, $Y_{tot\,S1}$, which is the sum of the profile losses contribution ($Y_{p\,S1}$) and the clearance & secondary flows losses contribution ($Y_{c\,S1}$).

The losses, quantified by the total-pressure loss coefficient, are discharged onto the static pressure jump that occurs across the stator row.

S1 Profile losses

For the calculation of the total-pressure loss coefficient for profile losses in a row of flat plates, reference is made to the work of Coppinger & Swain [11], which provides its trend as a function of the angle of incidence, as shown in fig. 2.11:

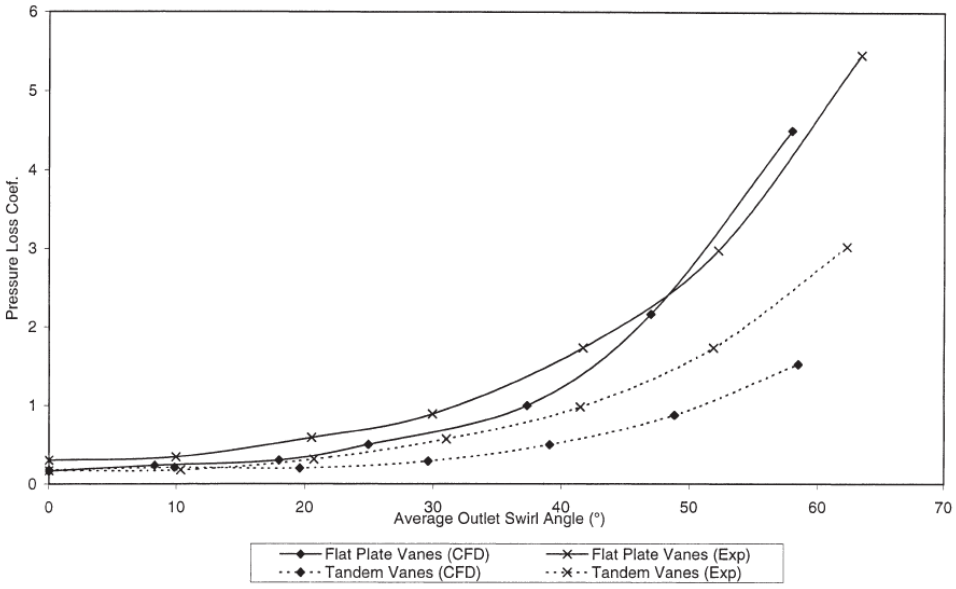

Figure 2.11: Total-pressure loss coefficient versus incidence angle.
From: Coppinger [11]

The trend of Y_p for flat plates is then reconstructed pointwise and approximated with a fourth-order polynomial function, whose coefficients are:

Coefficient	Value
A_0	0.020606060606061
A_1	-0.000338023088023
A_2	0.000114393939394
A_3	-0.000001414141414
A_4	0.000000030303030

Table 2.8: Coefficients of the polynomial approximating Y_p

At each timestep, the angle of incidence of S1 is known, and consequently, the value of $Y_{p\,S1}$:

$$Y_{p\,S1} = A_4\,\theta_{S1}^4 + A_3\,\theta_{S1}^3 + A_2\,\theta_{S1}^2 + A_1\,\theta_{S1} + A_0 \tag{2.73}$$

S1 Clearance losses

When the stator rotates to redirect the airflow, a portion of it is not processed by the blades due to clearance. To evaluate $Y_{c\,S1}$, when the stator has an incidence different from zero, the correlation by Dunham & Came [10] is used (both the contribution of clearance and secondary losses are considered):

$$Y_{c\,S1} = \frac{c_s}{b}\left[0.0334\,\frac{1}{\cos\left(\theta_{S1}\right)} + B\left(\frac{k}{c_s}\right)^{0.78}\right]\left(\frac{c_{L\,S1}}{1/\sigma_s}\right)^2\,\frac{1}{\left(\cos\left(\theta_{S1\,m}\right)\right)^3} \tag{2.74}$$

where the lift coefficient is:

$$c_{L\,S1} = 2\,\frac{1}{\sigma_s}\left|\tan\left(\theta_{S1}\right)\right|\,\cos\left(\theta_{S1\,m}\right) \tag{2.75}$$

and the mean angle is:

$$\theta_{S1\,m} = \arctan\left(\frac{\tan\left(\theta_{S1}\right)}{2}\right) \tag{2.76}$$

Also, the parameter B is chosen to be $B = 0.47$ since the blades are unshrouded.

When the stator row has an incidence of of 0 [deg], the total-pressure loss coefficient related to the clearance & secondary flows is set to be null since the flow path is not influenced by the clearance.

Pressure evaluation after S1

Once $Y_{S1\,tot}$ is known, it is possible to calculate the values of the static pressure and the total pressure at section 1 (between the upstream stator and the rotor):

$$P_{t1} = P_{t0} - Y_{tot\,S1}\,\frac{1}{2}\,\rho\,V_x^2 \tag{2.77}$$

$$P_1 = P_{t1} - \frac{1}{2}\,\rho\,V_1^2 \tag{2.78}$$

At this point, the analysis of the upstream stator is completed.

2.3.4. The downstream stator control law

The downstream stator is located after the rotor, between section 2 and 3. Unlike the upstream stator, its purpose is to slow down the flow exiting the rotor as much as possible to minimize losses due to the kinetic energy associated to the flow leaving the machine.

At the same time, this component must accomplish its task while avoiding significant losses. This implies that it should rotate as much as possible to oppose the airflow but without stalling, hence without exceeding θ_{max} (the same limit angle imposed on the first stator).

The angle of the absolute velocity at the rotor exit is calculated:

$$\alpha_2 = \arcsin\left(\frac{V_{2t}}{V_2}\right) \tag{2.79}$$

This quantity coincides with the angle of incidence of the downstream stator, in case it is straight. The control is then performed on this angle, as when its absolute value is greater than θ_{max}, it causes the stator to stall.

When this condition is met, the stator is forced to rotate on itself by:

$$\theta_{S_2} = \alpha_2 + \theta_{max} \quad (if\ \alpha_2 < 0) \tag{2.80}$$

or by:

$$\theta_{S_2} = \alpha_2 - \theta_{max} \quad (if\ \alpha_2 > 0) \tag{2.81}$$

When the stator is rotated, its effective incidence angle is:

$$\delta_{s_2} = \theta_{S_2} - \alpha_2 \tag{2.82}$$

For a clearer visualization, consider fig. 2.12:

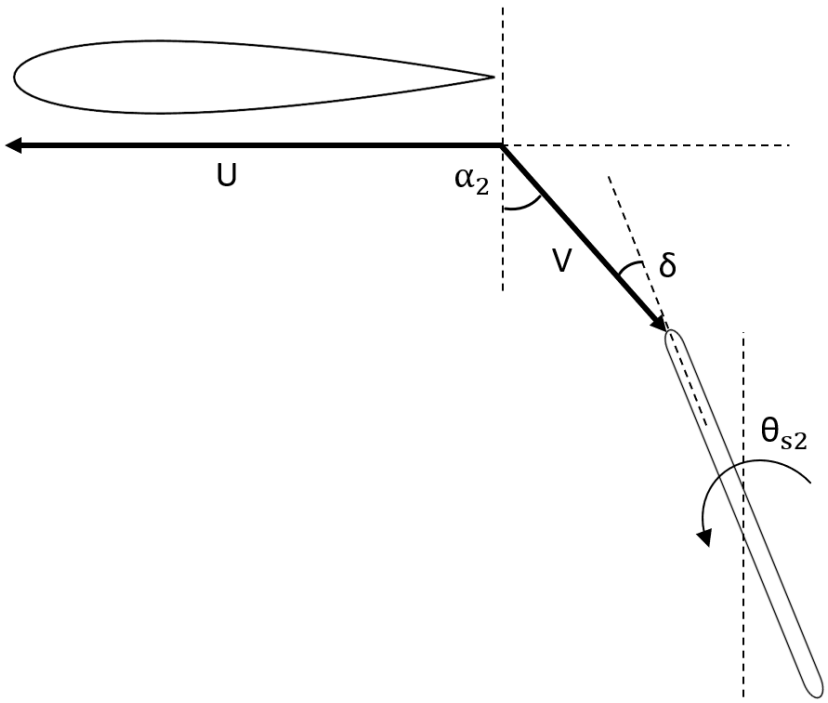

Figure 2.12: S2: Stall controll

The Absolute velocity exiting the downstream stator is:

$$V_3 = \frac{Vx}{\cos(\theta_{S2})} \tag{2.83}$$

and its tangential component is:

$$V_{3t} = V_3 \ \sin(\theta_{S2}) \tag{2.84}$$

The next step is to analyze the losses related to the downstream stator.

2.3.5. Losses related to the downstream stator

The calculation of losses for the downstream stator proceeds similarly to those related to the upstream stator, given that the two rows of blades are identical.

S2 Profile losses

For profile losses, reference is always made to the studies of Coppinger & Swain [11], as done for S1. The profile losses for S2 at each time step are:

$$Y_{p\,S2} = A_4\,\delta_{S2}^4 + A_3\,\delta_{S2}^3 + A_2\,\delta_{S2}^2 + A_1\,\delta_{S2} + A_0 \tag{2.85}$$

In this case, it is important to note that the incidence of S2, which follows the flow downstream of the rotor, is always constant and is the maximum allowed. Consequently, these losses ($Y_{p\,S2}$) are always higher than those of S1 and are the same at each time step.

S2 Clearance losses

With the same precautions taken for S1, the clearance losses of S2 are evaluated at each time step with the Dunham & Came correlation [10]:

$$Y_{c\,S2} = \frac{c_s}{b}\left[0.0334\,\frac{1}{\cos\left(\delta_{S2}\right)} + B\left(\frac{k}{c_s}\right)^{0.78}\right]\left(\frac{c_{L\,S2}}{1/\sigma_s}\right)^2\,\frac{1}{\left(\cos\left(\delta_{S2\,m}\right)\right)^3} \tag{2.86}$$

where the lift coefficient is:

$$c_{L\,S2} = 2\,\frac{1}{\sigma_s}\left|\tan\left(\delta_{S2}\right)\right|\,\cos\left(\delta_{S2\,m}\right) \tag{2.87}$$

and the mean angle is:

$$\delta_{S2\,m} = \arctan\left(\frac{\tan\left(\delta_{S2}\right)}{2}\right) \tag{2.88}$$

In this case as well, the losses are expected to be higher than those of S1.

Losses related to kinetic energy

The downstream stator has a clear influence on the losses related to the kinetic energy at the exit of the machine.

The lost power is:

$$P_{kin} = \rho \, q(j) \, \frac{V_3^2}{2} \tag{2.89}$$

This value increases with the exit velocity (V_2 if there is only the rotor, V_3 with the stators): that is why the role of the downstream stator is to slow down the flow at the exit, as shown in fig. 2.13

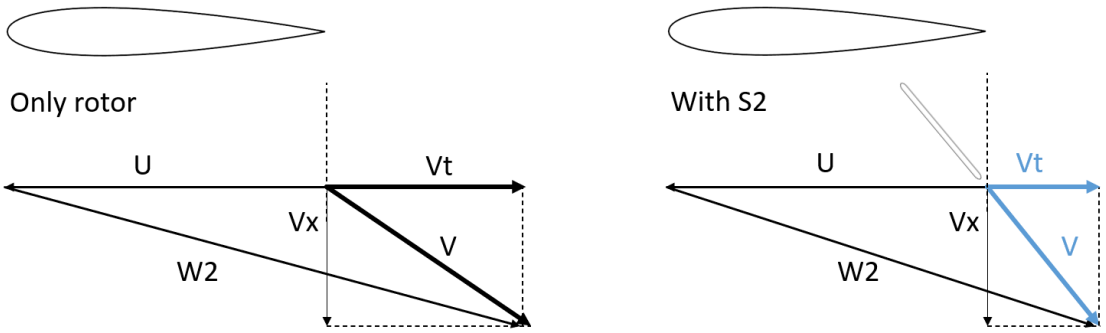

Figure 2.13: S2: reduction of kinetic energy at the exit

Pressure evaluation after S2

Once $Y_{S2\,tot}$, sum of $Y_{p\,S2}$ and $Y_{c\,S2}$, is known, it is possible to calculate the values of the static pressure and the total pressure at section 3 (after the downstream stator):

$$P_{t3} = P_{t2} - Y_{tot\,S2} \, \frac{1}{2} \, \rho \, V_2^2 \tag{2.90}$$

$$P_3 = P_{t3} - \frac{1}{2} \, \rho \, V_3^2 \tag{2.91}$$

At this point, the analysis of the upstream stator is completed.

2.3.6. The diffuser

The last component of the machine is a diffuser, which aims to restore the air flow pressure to the ambient level. Since the machine is axial, it has a conical shape. Its pressure recovery factor can be assumed:

$$c_p = \frac{P_4 - P_3}{P_{t3} - P_3} = 0.75 \tag{2.92}$$

So far, the pressures have been calculated based on the reference ambient pressure. However, the analyzed period begins from the moment the wave is at maximum speed, at which point the chamber is already pressurized. To understand the true value of pressures at each point in the machine, it is necessary to define the error in the calculation of the pressure exiting the diffuser compared to the value at which it is expanded: the ambient pressure.

The error made on the pressures is assessed as:

$$P_{err} = P_{atm} - P_4 \tag{2.93}$$

At this point, the static and total pressure at each section of the machine are updated by adding the error made on them to obtain their true value:

$$P_{true} = P + P_{err} \tag{2.94}$$

$$P_{t\,true} = P_t + P_{err} \tag{2.95}$$

2.3.7. An alternative to Flat Plates

An alternative that has been considered instead of flat plates is to use NACA0012 airfoils. The geometry described earlier remains the same; the only change is in the blade sections.

Pros and cons

The reasons for analyzing this alternative are:

- When they are rotated at significant angles, NACA0012 is expected to react aerodynamically better than flat plates, having a much less pointed leading edge.
- In the literature, there is much more data analyzing the behavior of NACA0012 compared to flat plates. These studies range from individual profile analyses ([17],[18]) to studies involving high/low span blades/wings ([19]) and also cascade of blades ([20],[21]).

Disadvantages are:

- When placed at zero incidence, NACA0012 profiles certainly generate more losses compared to flat plates, through which the flow passes almost unchanged.
- Using NACA0012 profiles, when the wave reverses its motion and the two stators

must exchange their roles, the blades must undergo a 180-degree rotation on themselves to have the correct orientation, since (unlike flat plates) the leading and trailing edges are different. This would undoubtedly lead to a more complex (and expensive) mechanism in the implementation of the machine.

Losses evaluation

The trend of the drag coefficient for a series of NACA0012 profiles as a function of the angle of attack and solidity is available([20]), as shown in fig. 2.14:

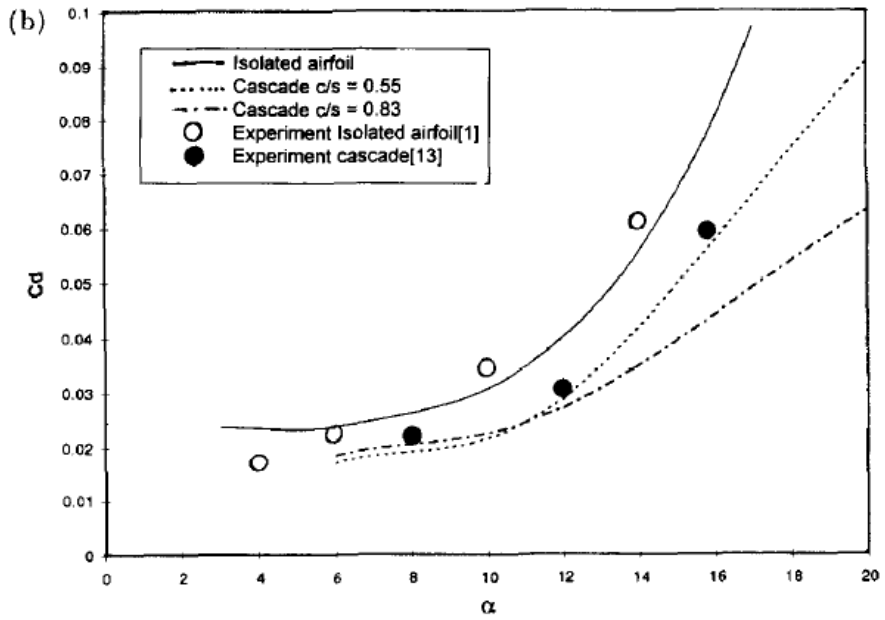

Figure 2.14: Cd vs α for a NACA 0012 cascade

So, for what concerns the profile losses, it is possible to evaluate the total-pressure loss coefficient through the following relationship between it and the C_d:

$$c_D = \frac{s}{c}\, Y\, \frac{\cos \alpha_m^3}{\cos \alpha_{out}{}^2} \tag{2.96}$$

2.4. The model - constant solidity

Until now, the complete model has been described. As anticipated, the code allows the user to decide whether to perform the analysis only on the rotor or on the rotor between the two stators. Another choice provided to the user is to perform the analysis in a particular case where the rotor is not characterized by constant chord, as analyzed so far, but by constant solidity.

2.4.1. Considerations

The choice to analyze this geometry as well arises from the following considerations:

- To verify if maintaining the optimal (at midspan) solidity value, as defined by Raghunathan [5], constant throughout the machine has any advantage compared to the canonical case with constant chord.
- In the case of constant chord, the solidity is high at the hub: a high root of the blade could obstruct too much the incident flow. This phenomena should be reduced with constant solidity since the blade root becomes smaller.
- The final part of the blade is the region responsible for producing the majority of the useful power. In the case of constant solidity, this region would be more extensive and produce more power than the constant-chord case.

Two disadvantages that could be encountered using this solution are:

- There could be a considerable increase of the drag force in the final region of the blades.
- Due to the increased forces near the blade tip, there could be structural integrity issues at the root due to the reduced section of the root of the blade at the hub.

2.4.2. Differences from the constant-chord model

The sizing of the turbine does not undergo variations, as it is always based on values at the midspan. Only the blades present a different shape, as showed in fig. 2.15:

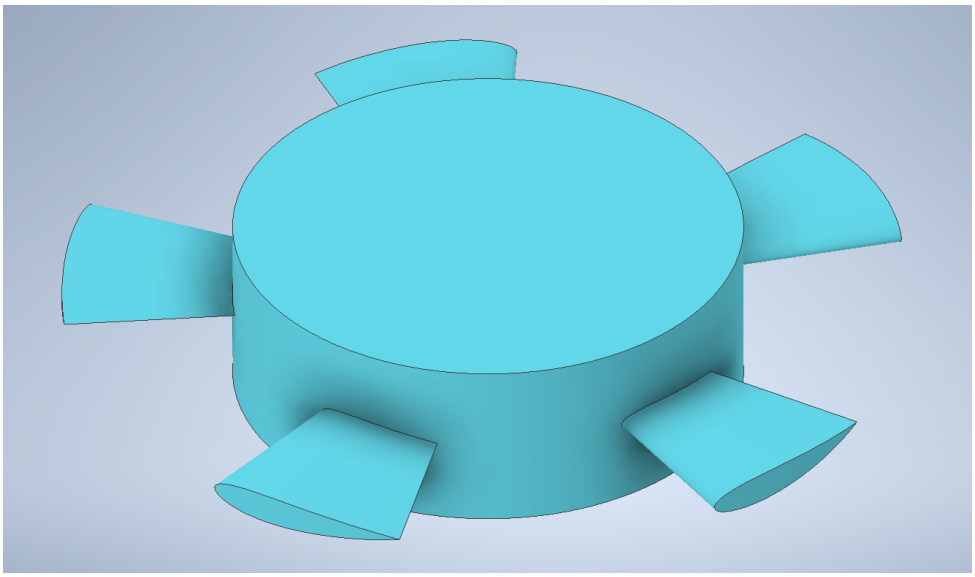

Figure 2.15: Wells rotor with constant solidity

In the rotor analysis, instead of considering solidity varying with the radius, the solidity at the midspan is always used, while the chord varies:

$$c = \frac{\sigma \; 2\pi \; dr_{up}}{N_b} \tag{2.97}$$

Furthermore, no correction is applied to solidity in the coefficients of the forces F_x and F_t. The ratios rC_x and rC_t are always constant (at the value of solidity at the midspan) with the value:

- $rC_x = 1.25$
- $rC_t = 1.3$

As in the case of constant chord, this solution can be evaluated on its own or enriched by the presence of the two stators. In this way, once the geometry of the rotor is fixed, it is possible to analyze and compare the four different configurations:

- R_c: Rotor (with constant chord)
- R_s: Rotor (with constant solidity)
- $R_c + VIGV$: Rotor (with constant chord) and the stators
- $R_s + VIGV$: Rotor (with constant solidity) and the stators

under the influence of waves of different intensity.

3 | CFD analysis

The role of CFD in this work is to validate the model described in the previous chapter. Specifically, the conducted simulations aim to reinforce certain assumptions and provide a more realistic guideline in the analysis of Wells turbines.

The simulations were conducted with Ansys - CFX.

3.1. Simulations on the rotor

The rotor tests were conducted as follows: The behavior of the turbine is analyzed under the influence of a wave of intensity such as to bring the hub almost to stall. In particular, simulations are conducted on the mid and tip hub sections in such a way that the hub experiences angles ranging from total drag to stall (angles on other sections will be smaller). In this way, it is possible to assess various aspects of the turbine's behavior under the influence of a range of angles encountered during its operational period: In this case, the goal is to evaluate the axial and tangential force coefficients, as well as the angle of the flow exiting the rotor.

3.1.1. Problem setting

CFX-TurboGrid

To conduct these simulations on the rotor, three meshes were created for the three values of solidity. Each mesh is 2D and consists of 100000 elements.

TurboGrid is not able to generate a mesh for a NACA0015 oriented at 90 degrees: the problem arises from the fact that it can't identify the leading edge and the trailing edge according to the scheme it operates with (which in this case would coincide respectively with the entire upper and lower part of the profile).

The solution to this problem is transferred to the CFX pre-settings, but firstly, the mesh is created for a profile oriented at zero incidence in CFX-TurboGrid, as shown in fig. 3.1, where the axis of rotation is Z:

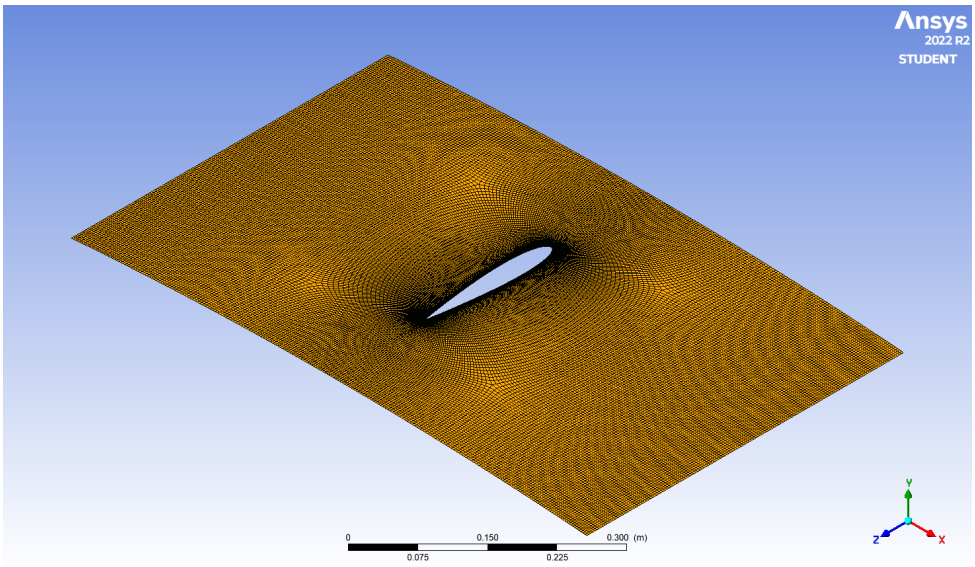

Figure 3.1: Mesh for a NACA0015 airfoil at zero incidence

CFX Pre-processing

In CFX-PRE the Inlet, Outlet, and both Periodic surfaces are redefined to apply the proper boundary conditions. The curvature of the geometry is not in the right direction, but this fact is negligible since the geometry is in 2D.

As shown in fig. 3.2, the Inlet BC is imposed on the (old) Periodic surface PER1, The Outlet BC is imposed on the (old) Periodic surface PER2, and a Rotational periodicity is imposed between the (old) Inflow and (old) Outflow surfaces.

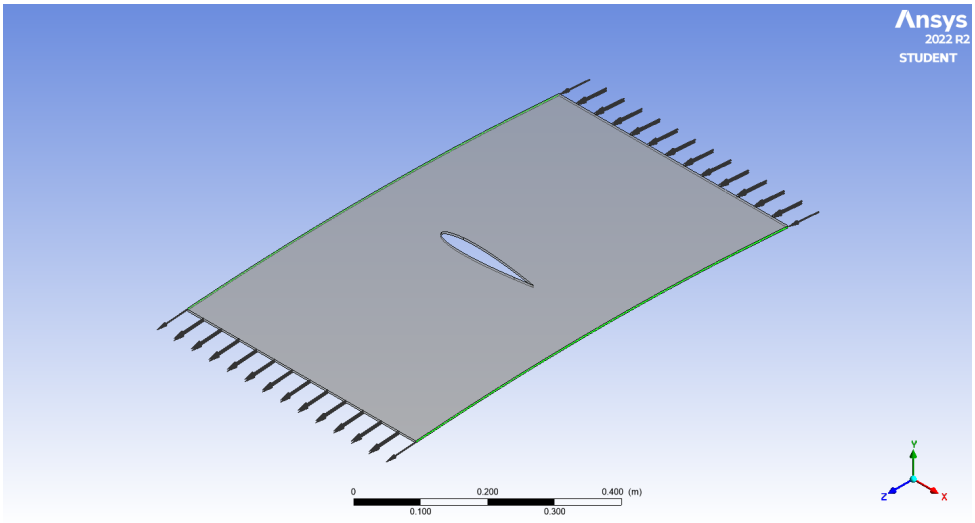

Figure 3.2: Definition of Boundary conditions on the proper surfaces

Normally, to operate in 2D in CFX, the dimensions of the machine are not real (a radius is set at an unrealistic high value to have minimal curvature) but must be consistent with the real case, especially the solidity must be correct. Usually, it is redefined by increasing the number of blades so that there is a correct proportion between the real case and the 2D case, but in this case, this is not possible: changing the number of blades increases the distance between Inlet and Outlet and not between the periodic surfaces.

To have the correct solidity, it is necessary to build correctly the .crv files of the hub and shroud from which the geometry is created, to set the distance between the periodic surfaces.

To have the desired distance between Inlet and Blade and between Blade and Outlet, one must act on the choice of the number of blades.

In particular, a distance of three times the rotor chord is imposed between the Blade and the Outlet, to map correctly the flow behaviour. There will be the same distance between the Inlet and the Blade (this is not necessary but it is forced due to the limitation previously described).

For what concerns the Boundary conditions:

- Inlet: Total-pressure and Static Temperature are imposed.
- Outlet: Static Pressure is imposed
- Blade: No-slip wall
- Hub and Shroud: Free-slip wall
- Periodic surfaces: Rotational periodicity

CFX-Solver

Each simulation reach convergence before the maximum number of iteration imposed (2000), the residuals descend until the set value of $5 \cdot 10^{-}6$.

It makes sense to start a simulation from the results of the previous one, so that computation times are reduced. This choice is possible since, with the same geometry and solidity, the only variable is the flow rate (defined by the boundary conditions at the inlet and outlet).

As an example, for the set of simulation related to the hub solidity, the residual history for mass and momentum (fig. 3.3), energy (fig. 3.4) and turbulence (fig. 3.5) are shown (each main peak corresponds to the beginning of one simulation):

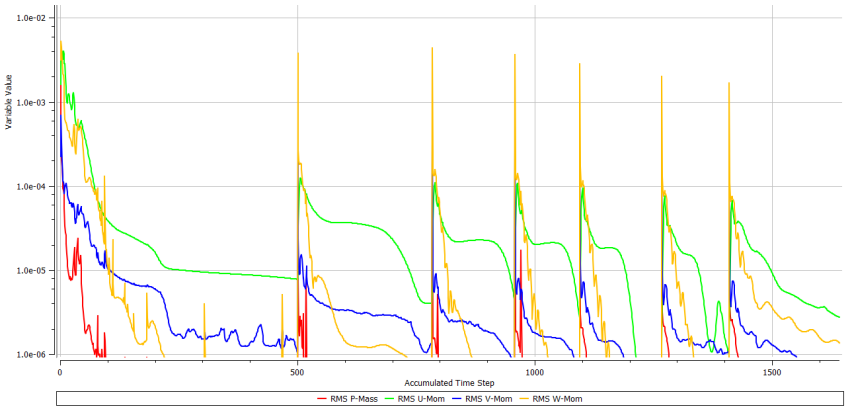

Figure 3.3: Mass and Momentum residuals

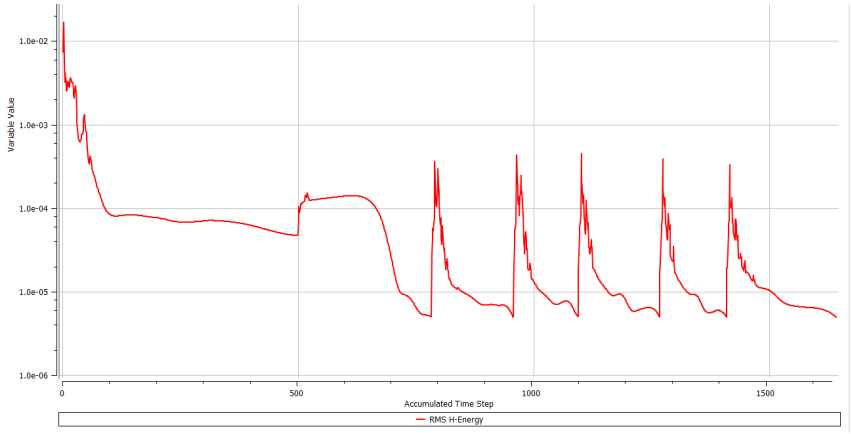

Figure 3.4: Energy residuals

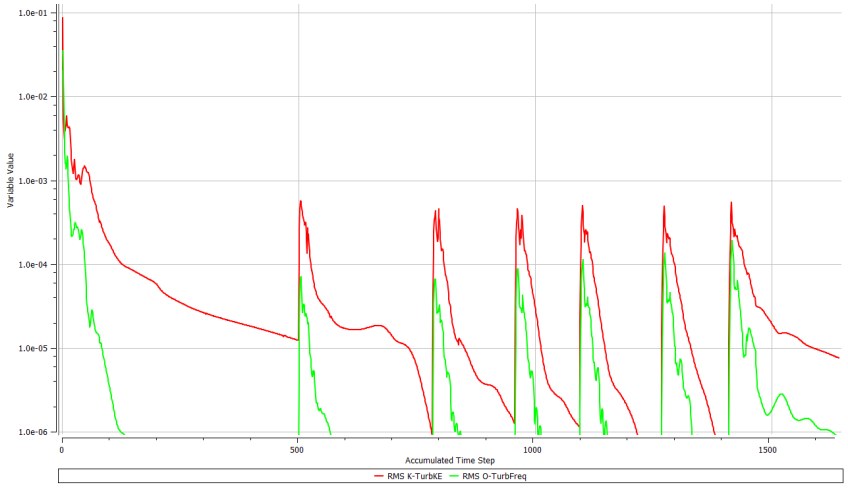

Figure 3.5: Turbulence residuals

CFX Post-processing

In the post-processing phase, results are extracted. In addition to checking the convergence of residuals, which is a necessary but not sufficient condition for the success of the simulation, it is advisable to analyze the flow field to ensure that the results make physical sense. As an example, the flow field around the hub is reported in fig. 3.6 for the characteristic angles of the beginning, middle, and end of the period are shown.

The hub is chosen as an example because it is the region where separation/stall phenomena occur first: simulations around the hub are the ones in which convergence is more challenging since a steady-state simulation is unable to accurately analyze turbulence when its characteristic scale increases too much. In any case, cases up to stall are being analyzed, and not beyond, so simulations of this kind are appropriate: an onset of separation around the hub at high angles is expected.

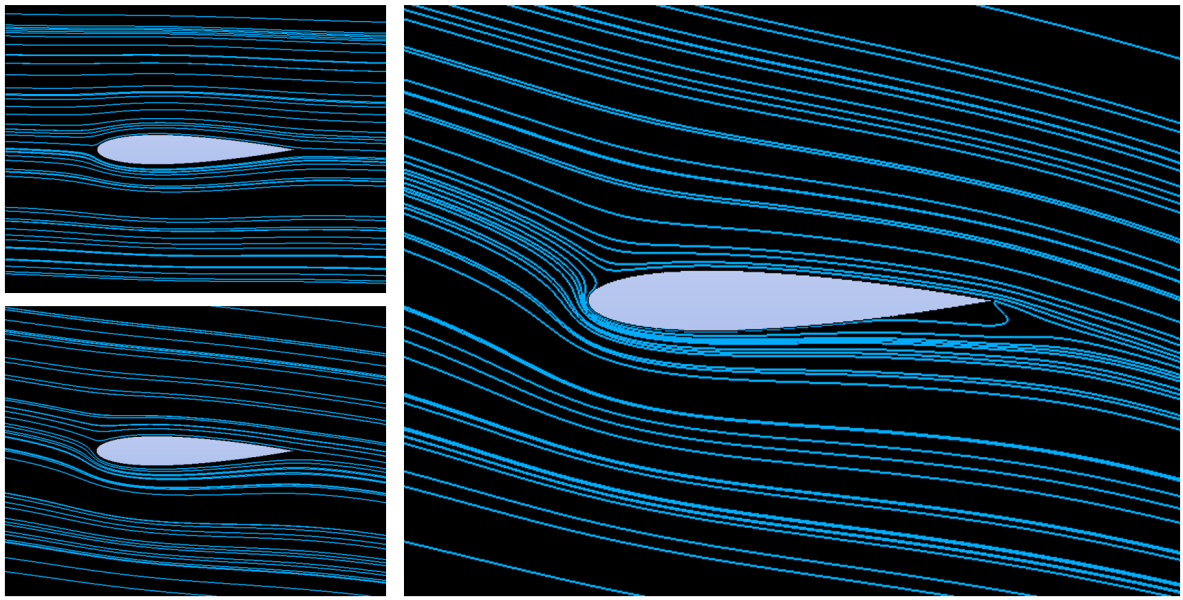

Figure 3.6: Velocity flow field at the hub

At the beginning of the period, the profile is subjected to the very low incidence angle of 1.2 [deg] and is entirely in total-drag condition: the force on it is expected to be opposite to the direction of motion. At the midpoint of the period, there is an incidence of 7.2 [deg]; during normal operating conditions, there are no characteristic phenomena to analyze. Separation phenomena starts to manifest on the profile's tail at an angle of 14.2 [deg], not far from the stall angle (15 [deg]).

The pressure field, visible in the figure fig. 3.7, is consistent with the velocity field:

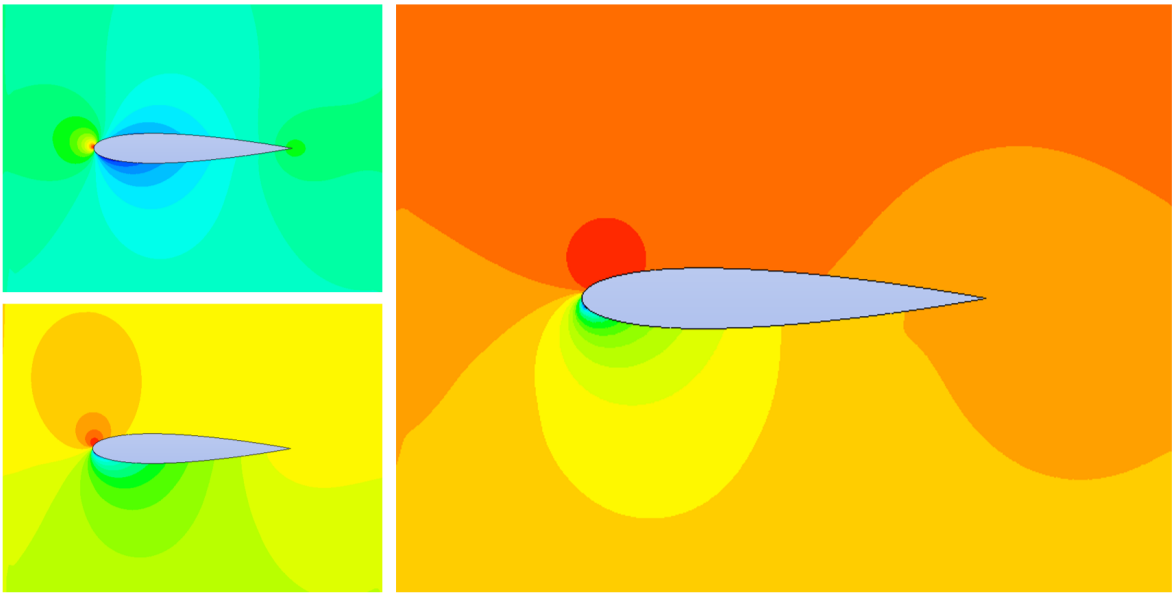

Figure 3.7: Pressure field at the hub

At this point, it can be stated that the simulations have converged, and it is possible to extract and analyze the quantities of interest.

3.1.2. Force coefficients evaluation

Choosing to reconstruct the trends of force coefficients is aimed at validating the starting point from which this study proceeds: Raghunathan's work [5].

The reason to deepen this study is that it involves an analysis that starts with a study of individual 2D profiles, to which a corrective and coefficient is subsequently applied to predict the effect of solidity. With CFD a significant deviation from the old model is not expected, but it allows for the simultaneous evaluation of various aspects, constituting a more realistic assessment.

Through CFD analysis, in the post-processing phase it is possible to extract the axial and tangential force values for each case, which are then made dimensionless to obtain their respective coefficients:

$$C_x = \frac{F_x}{\frac{1}{2}\,\rho\, W_1^2\, c\, dR} \tag{3.1}$$

$$C_t = \frac{F_t}{\frac{1}{2}\,\rho\, W_1^2\, c\, dR} \tag{3.2}$$

where dR is the width of the domain.

The plots in fig. 3.8 and fig. 3.9 show the variation of the axial force coefficient and tangential force coefficient with respect to the incidence angle, for different solidity values.

The force coefficients increase with the angle of incidence and are higher for high solidity:

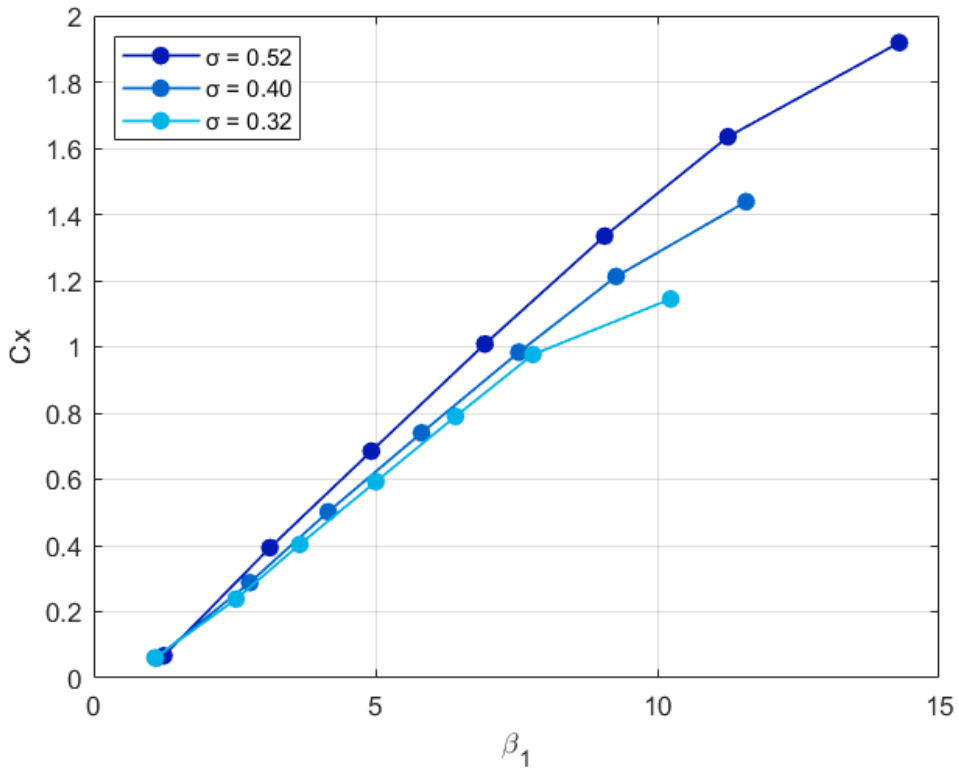

Figure 3.8: C_x versus β_1 and solidity effect

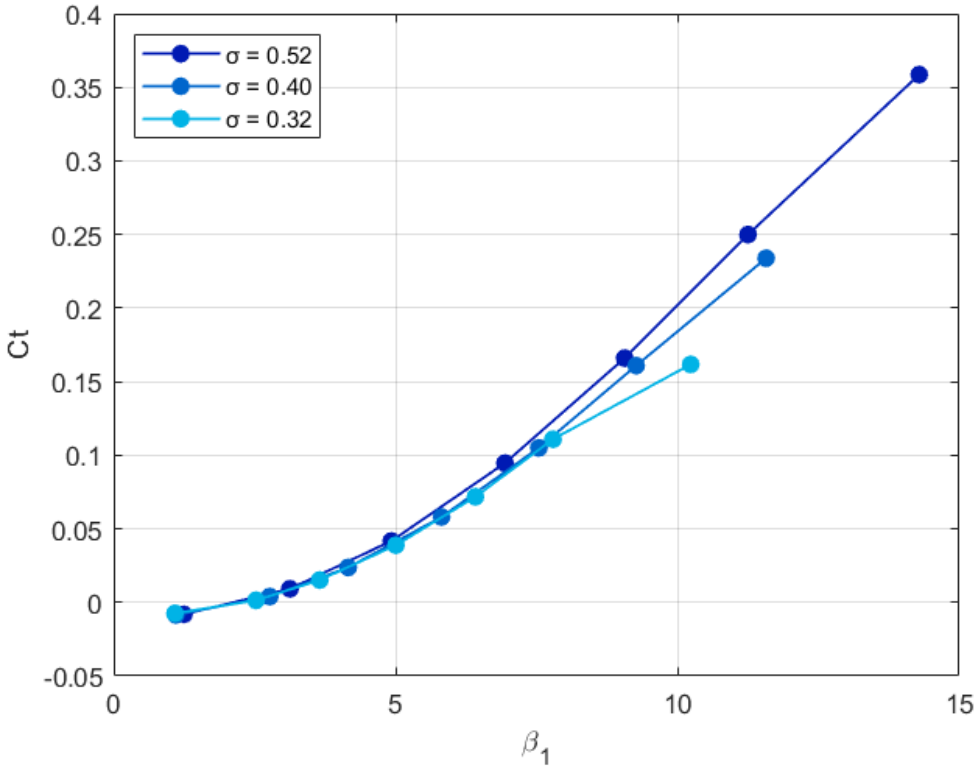

Figure 3.9: C_t versus β_1 and solidity effect

The fact that force coefficients are higher for high solidity should not be confused with the fact that for the force developed on the blades, it is the opposite. At the tip, where the incidences are the lowest, the (relative) velocity W on the blade is much higher than at the hub. This is why at the tip the forces are greater even though their coefficients are lower than those at the hub.

The obtained data is comparable to that of the initial model. In figure fig. 3.10 and fig. 3.11 the correspondence between the values of the coefficients of the model and those obtained with CFD are reported. The difference between CFD and the model is quite small, indicating that the initial model is reliable (although CFD provides a more accurate result). Quantities related to the midspan solidity are chosen as an example:

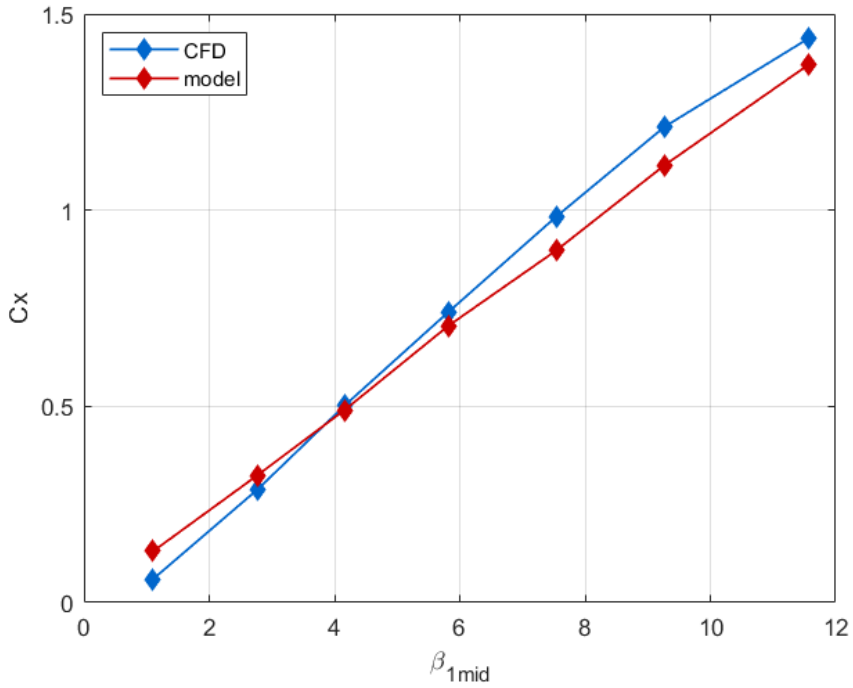

Figure 3.10: Cx versus β_1 at midspan: comparison between the model and CFD

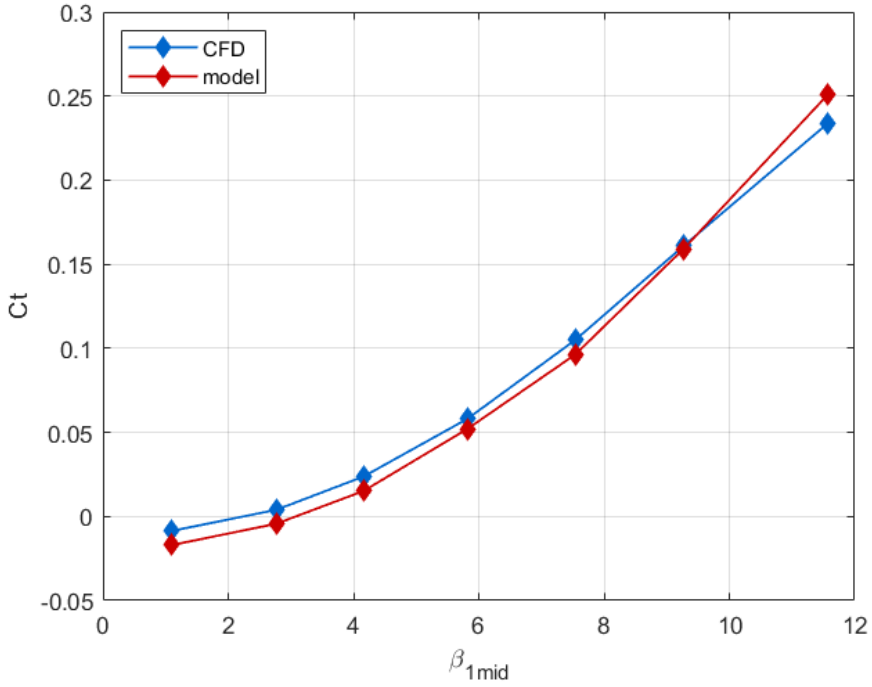

Figure 3.11: Ct versus β_1 at midspan: comparison between the model and CFD

3.1.3. Discharge angle evaluation

Another interesting aspect to verify consist of evaluating the discharge angle of the rotor: in the model, it is calculated from the Euler work, but for a Wells turbine this method is unstable during the period when the flow tends to zero (which is why other methods are used to calculate this quantity during that phase).

To do this, in the post-processing phase, a plane is created at a distance equal to two times the thickness of the rotor profile, on which the average axial and tangential velocity components are calculated.

From these values, it is possible to determine the discharge angle of the rotor and evaluate the effect of solidity on this quantity, as shown in fig. 3.12

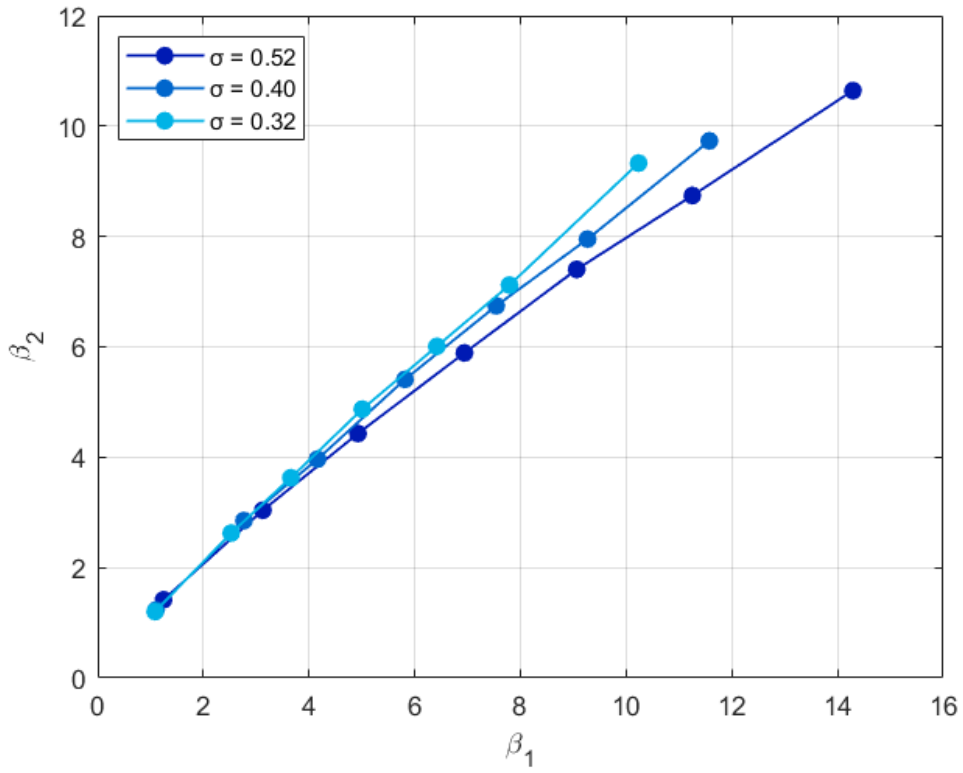

Figure 3.12: β_2 versus β_1 and solidity effect

At this point, it is possible to compare the obtained values with those of the implemented model. The model is quite accurate in evaluating the angles in the whole period, noting that in the total-drag phase it deviates slightly from the expected values. It makes sense to assert that CFD is a more accurate reference in evaluating flow exit angles, especially in the total-drag phase especially.

The approximation used in CFD involves considering 'average' values on the plane created downstream of the rotor. However, the total-drag phase is the least influenced by this approximation, as the flow around the rotor is very similar to itself and is homogeneous across the entire motion field. Near stall, the flow field is less uniform and more heterogeneous, but the results are extremely similar to those of the model. Therefore, this assumption does not make the analysis less accurate, and CFD can serve as a good guide for mapping the angles downstream of the rotor.

As an example, a comparison for the midspan values are shown in fig. 3.13, as before the da:

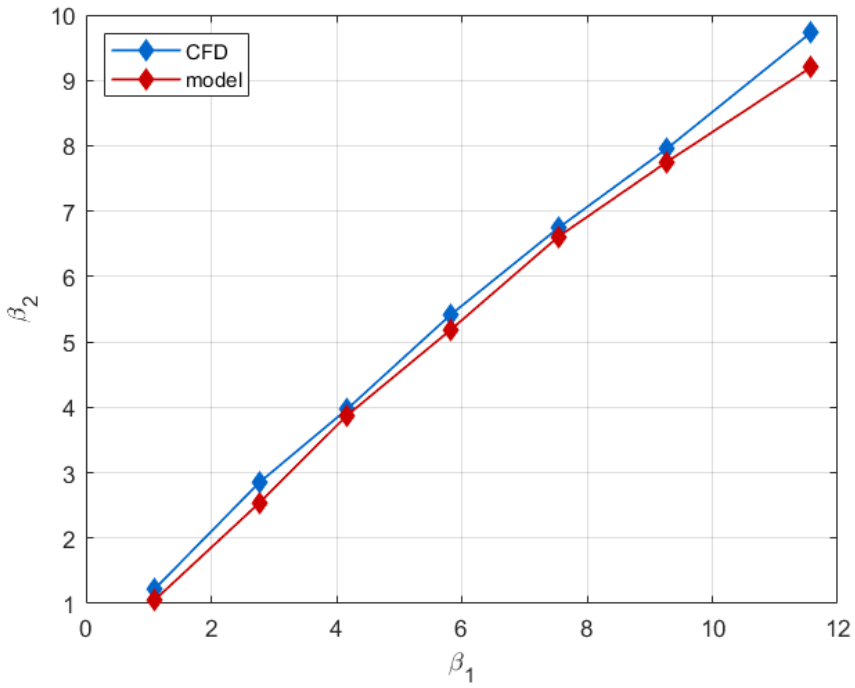

Figure 3.13: β_2 versus β_1 at midspan: comparison between the model and CFD

3.2. Simulations on the stators

The simulations on the stator cascade are conducted with the aim of verifying that it is capable of directing the airflow onto the rotor in the best possible manner.

Regarding the blade profiles, three are taken into consideration: a Naca0012, a thin flat plate, and a thick flat plate. The behavior of each profile is analyzed for a set of angles of incidence that allow for conducting steady-state simulations, so up to the formation of large scale turbulence/separation phenomena.

3.2.1. Setting

The simulations are set up similarly to those of the rotor, with the difference that the grids can be created and managed conventionally.

For each case, the .crv files of hub, profile and shroud are created to define the geometry and a grid of nearly 100000 cells is generated with TurboGrid, with higher density near the trailing edge and the walls. The grids for the three geometries in the zero-angle-of-incidence cases are shown in figure fig. 3.14:

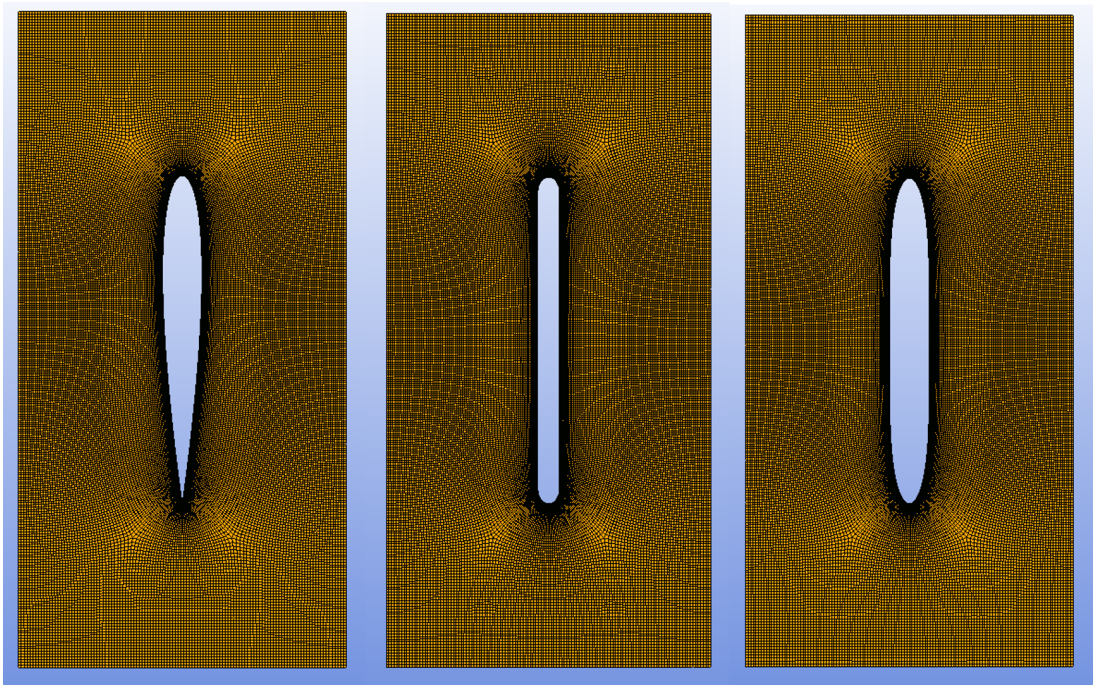

Figure 3.14: Meshes for the three stator profiles

Every geometry is tested at the same solidity and with the same number of blades: respectively $\sigma = 1$ and $N_b = 20$.

For what concerns the boundary condition in CFX-PRE:

- Inlet: Normal Speed and Static Temperature are imposed.
- Outlet: Static Pressure is imposed
- Blade: No-slip wall
- Hub and Shroud: Free-slip wall
- Periodic surfaces: Rotational periodicity

The residuals of all quantities settle on the target value of $10^{-}6$, ensuring the convergence of the simulations.

3.2.2. Post-processing

In all analyzed cases, the array of blades, inclined at a certain angle, is subjected to a flow with only axial absolute velocity.

The relevant quantities extracted are the absolute velocity and its tangential component downstream of the stator cascade. With these two data, a clear understanding of the flow discharged onto the rotor is obtained.

Additionally, the total pressure at the outlet is calculated in order to compute the total-pressure loss coefficient through the stator.

NACA0012

This geometry has been tested at the following set of incidence angles: [0 5 10 15 20 25]. Up to 20 [deg], the flow field remains smooth without separation, as shown in figure fig. 3.15.

Attempting to further incline the profile (25 [deg]), the simulation does not converge because turbulent phenomena reach a scale so high that a steady-state simulation cannot close the problem. This phenomenon is consistent with the theoretical model [20] from which the data were extracted to calculate the drag coefficient, where the cascade is also studied up to the incidence of 20 [deg].

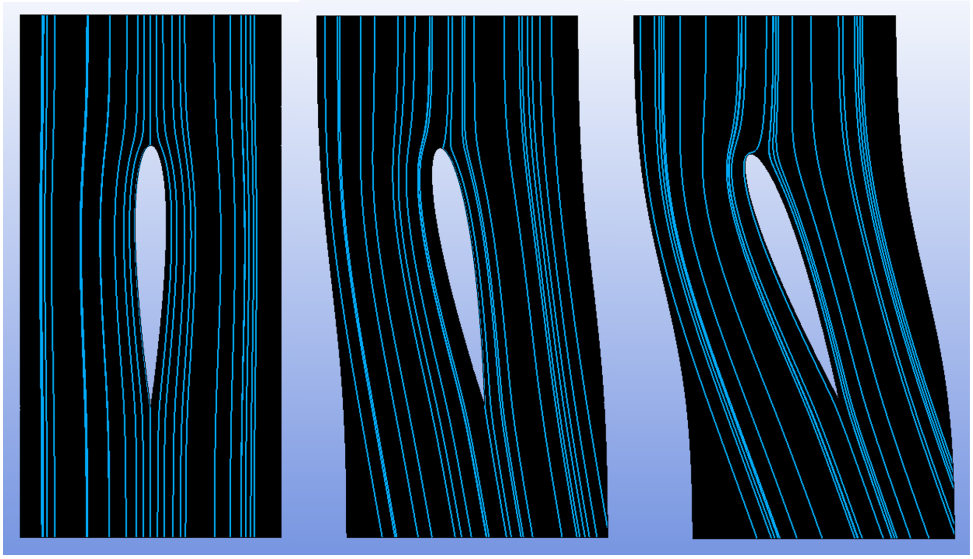

Figure 3.15: Streamline across a cascade of NACA0012 at $\theta = 0, 10, 20$ [deg]

The figure fig. 3.16 shows the absolute velocity at the outlet and its tangential component as a function of the rotation of the blade row (which corresponds to the angle of incidence relative to the airflow). The data are calculated starting from the axial and tangential components of the velocity downstream of the airfoil, on a plane located at 1/4 chord from the trailing edge. The error compared to the starting model is very small, but CFD provides a more accurate result.

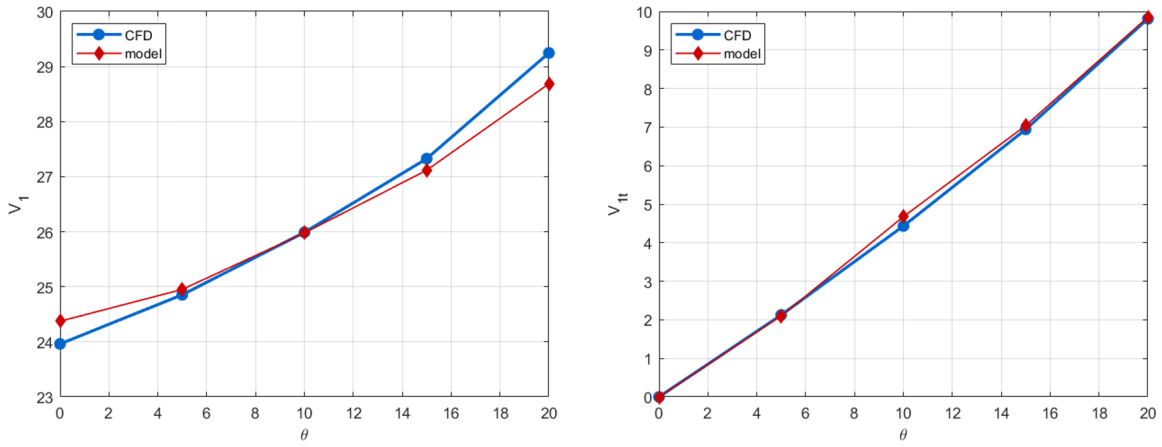

Figure 3.16: V_1 and V_{1t} versus θ for a cascade of NACA0012 with $\sigma = 1$

Furthermore, the total-pressure loss coefficient is presented in figure fig. 3.17. It is calculated by extracting the total pressure downstream of the airfoil and the static and total

pressures upstream. The CFD results deviate slightly from the model: this is because, in addition to the higher sensitivity of Y when calculated with respect to the inlet pressures, the drag coefficient of the model (in the absence of other data) belonged to a blade array with a solidity slightly lower than the unit solidity examined with CFD, that is still a more accurate result.

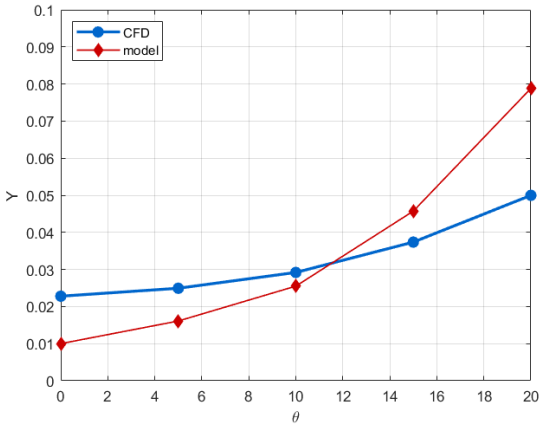

Figure 3.17: Total-pressure loss coefficient for a cascade of NACA0012 with $\sigma = 1$

Note about flat plates

For flat plates there is not a comparable amount of data/studies available as for profiles like NACA.

In particular, whenever a study is conducted on an array of VIGV, data about the profiles or the geometry that makes up the flat plates belonging to those cascades is never provided. This is because such studies are always focused on improving the performance of another machine (often a radial compressor), and each study uses specific and optimized blades for the particular case.

Moreover, it is very unlikely that flat and symmetrically profiled blades in two directions, as required in this work, are used in those cases, since having blades with an aerodynamic profile leads to better performance for those situations.

This work relies on Coppinger's reference [11] because it is the case with blades having a profile more similar to the needs of this study, even though optimization has been done on them with filing at specific points on the profile and so determining the exact geometry is not possible.

So, the two geometries used for the next two cases were chosen in this way:

- Thin flat plate: This has been composed in such a way as to be as similar as possible to those of Coppinger [11]. In particular, it is a rectangular shape with a thickness/length ratio of 0.04, while the leading and trailing edges are composed of two semi-circles (not ellipses to avoid making them even sharper, further promoting flow separation on the upper surface).
- Thick flat plate: analyzing the results of the thin flat plate (reported below), it was decided to test also a thicker geometry, created to try to combine the positive aspects of the NACA0012 while maintaining a symmetric geometry in two directions. With a thickness-to-chord ratio of 0.08, a flat plate is composed whose leading and trailing edges are both the tip of a NACA0012 (from the leading edge to the maximum thickness). The obtained geometry turns out to be quite similar to that of another study [15] conducted on a VIGV system, whose blades have an almost identical length-to-thickness ratio (even if they are not symmetric in two directions).

In figure fig. 3.18, the chosen geometries for this work (left) are shown alongside their closest counterparts found in the literature ([11] up right and [15] down right):

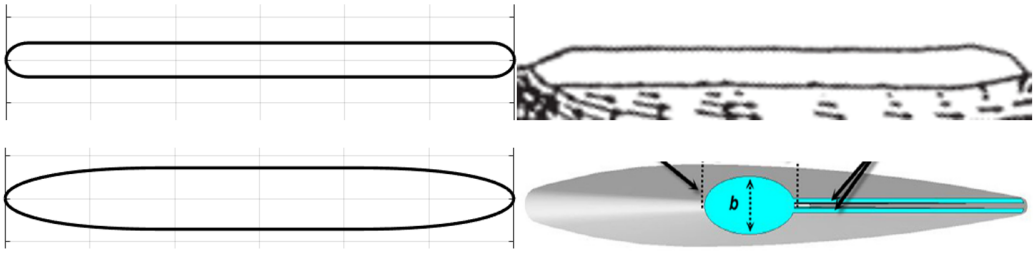

Figure 3.18: Similarity between the chosen geometries for FP and literature ([11],[15])

Thin FP

This geometry has been tested at the following set of incidence angles: [0,10,20,30,40]. The separation phenomena, as shown in figure fig. 3.19, are already evident at an incidence of 20 [deg] and become very intense towards 40 [deg], up to where steady-state simulations are able to complete calculations by reaching convergence.

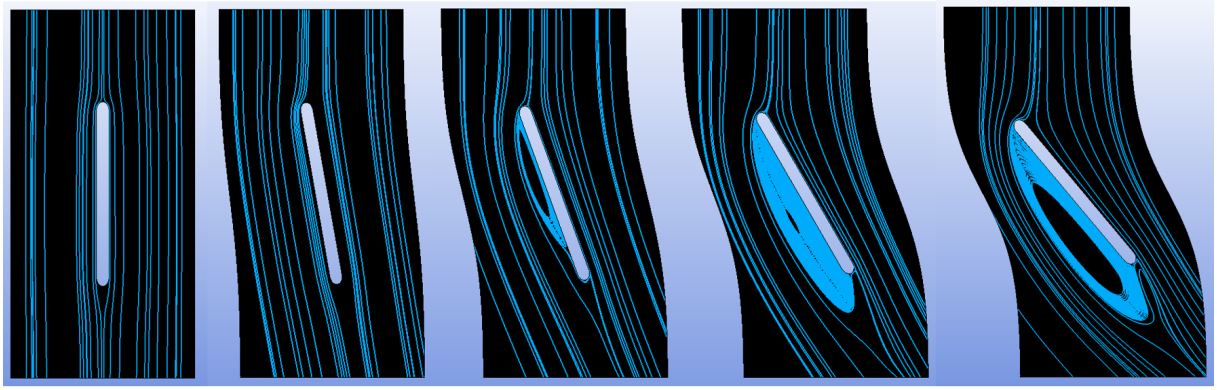

Figure 3.19: Streamline across a cascade of thin FP at $\theta = 0, 10, 20, 30, 40$ [deg]

The figure fig. 3.23 shows the absolute velocity at the outlet and its tangential component as a function of the rotation of the blade row (which corresponds to the angle of incidence relative to the airflow). The data are calculated starting from the axial and tangential components of the velocity downstream of the airfoil, on a plane located after the turbulent region. The error in comparison to the model becomes quite significant for higher incidences.

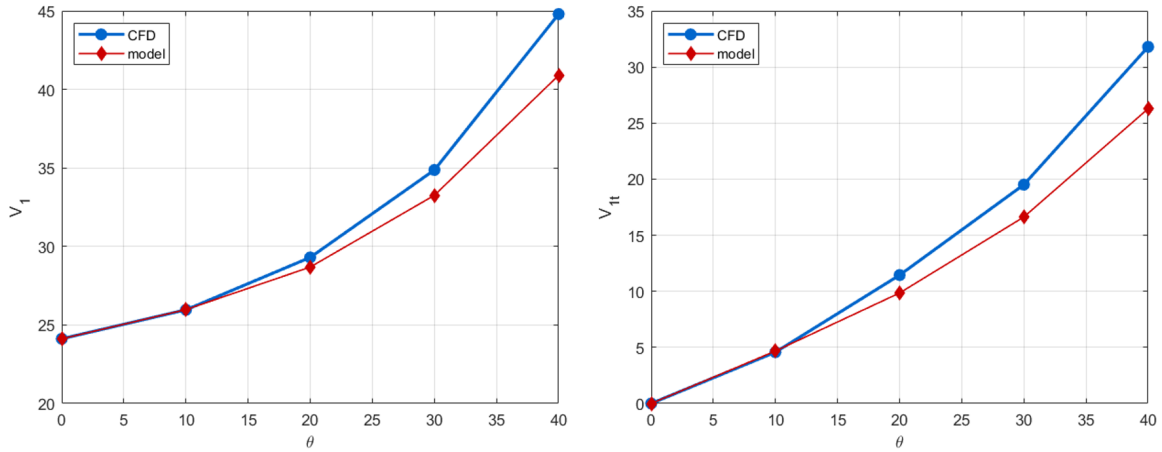

Figure 3.20: V_1 and V_{1t} versus θ for a cascade of thin FP with $\sigma = 1$

Furthermore, the total-pressure loss coefficient is presented in figure fig. 3.21. It is calculated by extracting the total pressure downstream of the airfoil and the static and total pressures upstream. The CFD results deviate significantly from the model. This is definitely due to using a geometry that is not sufficiently similar to that of the model.

The high sensitivity of the flow to the leading edge shape influences the entire downstream flow field generating high losses. In general, a row of flat plates, due to their pointed geometry, separates earlier than a row of airfoils, but the turbulent zone (at the same angle of attack) is smaller and more stable. Therefore, it makes sense to work to optimize the profile of the flat plates to minimize Y as much as possible and prefer them to airfoils for this application.

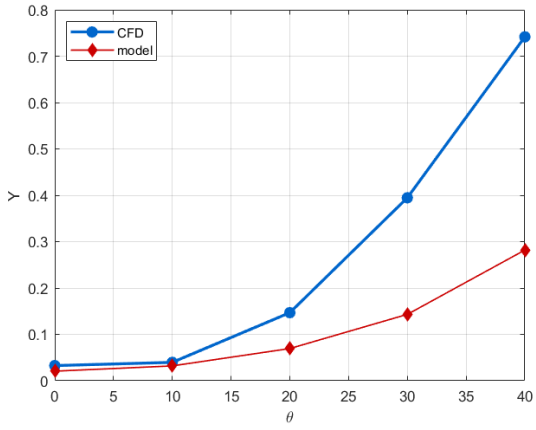

Figure 3.21: Total-pressure loss coefficient for a cascade of thin FP with $\sigma = 1$

Thick FP

This geometry has been tested at the following set of incidence angles: [0,5,10,15,20]. As shown in fig. 3.22, the behaviour is similar for the cascade of NACA0012.

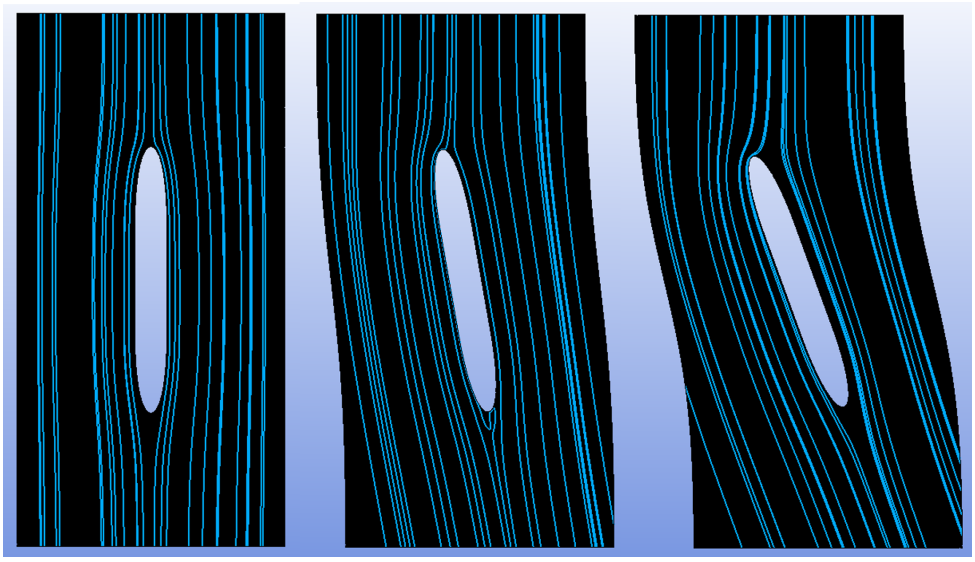

Figure 3.22: Streamline across a cascade of thick FP at $\theta = 0, 10, 20$ [deg]

The figure fig. 3.23 shows the absolute velocity at the outlet and its tangential component as a function of the rotation of the blade row (which corresponds to the angle of incidence relative to the airflow). The data are calculated starting from the axial and tangential components of the velocity downstream of the airfoil, on a plane located at 1/4 chord from the trailing edge. The error compared to the starting model is the smallest of the three cases.

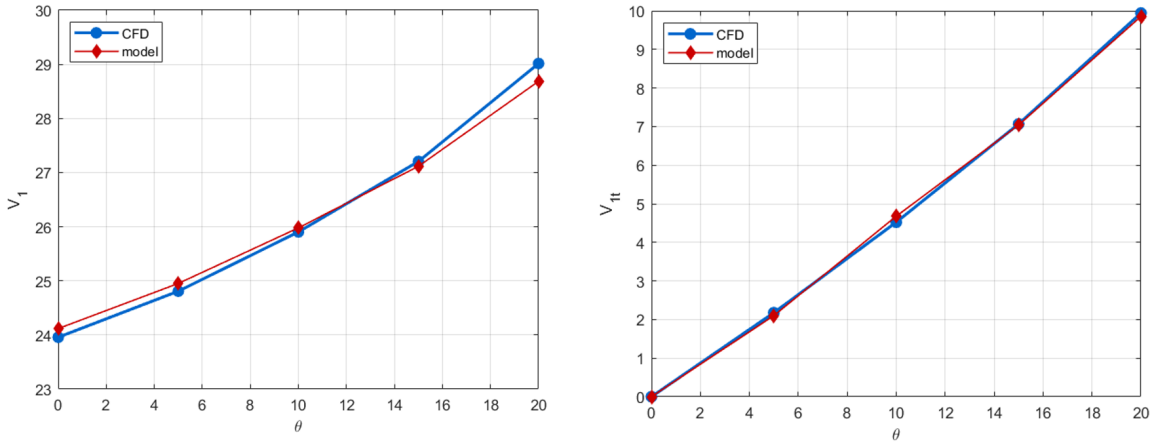

Figure 3.23: V_1 and V_{1t} versus θ for a cascade of thick FP with $\sigma = 1$

Furthermore, the total-pressure loss coefficient is presented in figure fig. 3.24. It is calculated by extracting the total pressure downstream of the airfoil and the static and total pressures upstream. The thick flat plate has a much more acceptable behavior than the thin flat plate for what concerns the losses generation, but has the same incidence limit of a NACA0012 cascade, with the additional benefict to be symmetric in two directions.

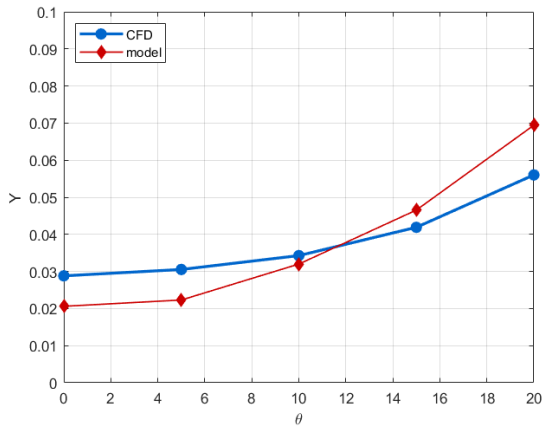

Figure 3.24: Total-pressure loss coefficient for a cascade of thick FP with $\sigma = 1$

3.3. Simulations on the complete configuration

In the preceding sections, the behavior of the rotor and stators has been analyzed individually. At this point, it is possible to test them together. The analysis is conducted at the midspan and a NACA0012 array is used as the stator.

The turbine, under the influence of a wave with an amplitude greater than the one used to size its geometry, will experience three significant moments, analyzed in this section:

- Case 1: the inlet velocity is high ($Vx = 27\ [m/s]$), and the upstream stator is rotated to reduce the incidence on the rotor and avoid stall.
- Case 2: the inlet velocity is moderate ($Vx = 17\ [m/s]$), with no corrective phenomena, so the upstream stator is set to zero incidence relative to the flow.
- Case 3: the velocity is low ($Vx = 7\ [m/s]$), the turbine is in total drag phase, so the upstream stator is rotated to increase the incidence on the rotor.

In all three cases, the downstream stator is positioned to avoid separation phenomena on itself.

3.3.1. Setting

As described in the preceding sections, the stator and rotor grids are curved in two different directions, making it impossible to generate an interface (Mixing Plane) between them. Therefore, simulations are conducted sequentially, first S1, then R, and finally S2.

The quantities at the outlet of each component are used as boundary conditions at the inlet of the next component. In particular:

- S1:
  - Inlet: Normal speed and Static Temperature
  - Outlet: Static Pressure
- R:
  - Inlet: Cartesian Velocity Components (from S1 Outlet) and Static Temperature
  - Outlet: Static Pressure
- S2:
  - Inlet: Cartesian Velocity Components (from R Outlet) and Static Temperature

– Outlet: Static Pressure

Also, for every piece:

- Blade: No-slip Wall
- Hub and Shroud: Free-slip wall
- Periodic Surfaces: Rotational Periodicity

3.3.2. Post-processing

During the post-processing phase, the following data is extracted for each section of the turbine: Absolute velocity (fig. 3.25), Static pressure (fig. 3.26) and Total pressure (fig. 3.27).

The graphs also include the values predicted by the model: comparing the data with that of the model, it can be observed that the incurred error is quite low.

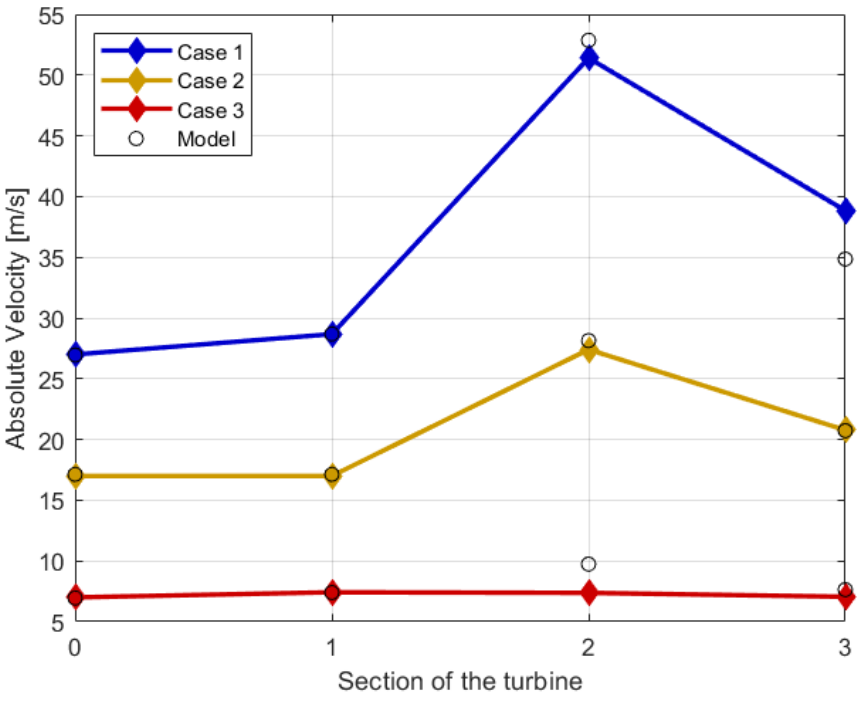

Figure 3.25: Absolute Velocity in every section

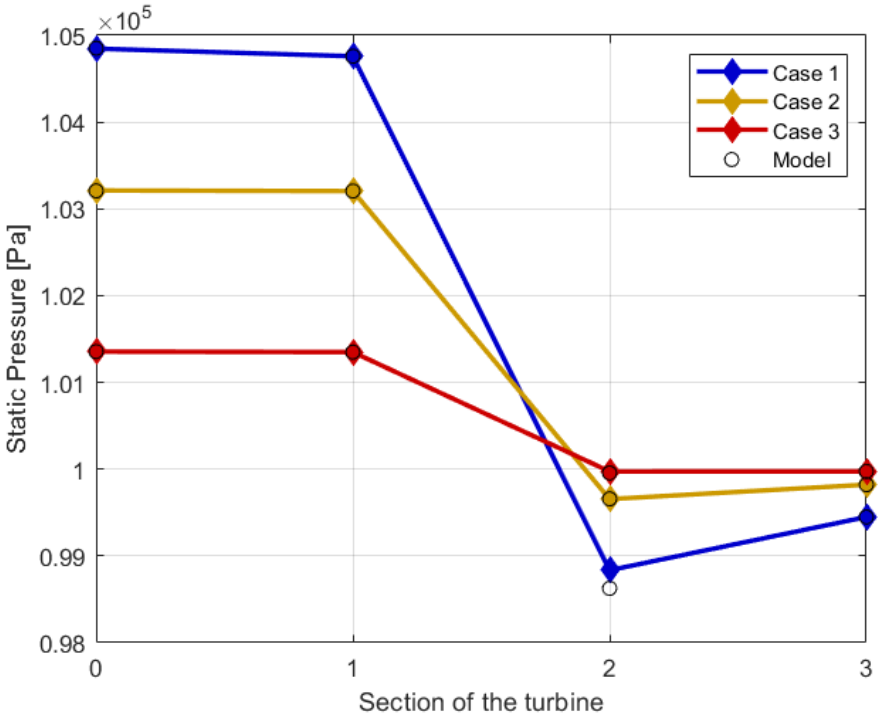

Figure 3.26: Static pressure in every section

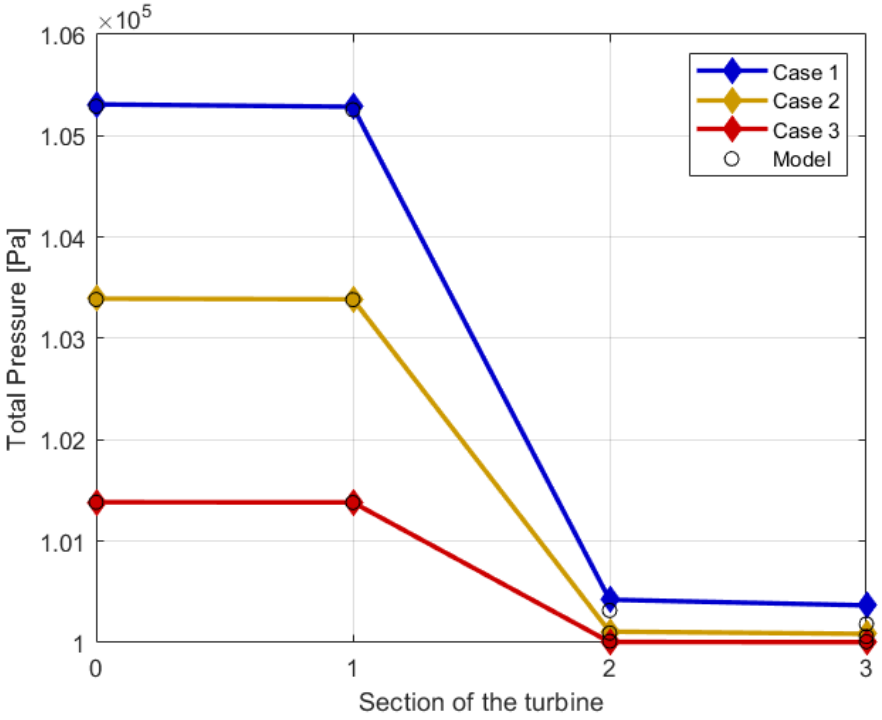

Figure 3.27: Total pressure in every section

Moreover, coefficients of axial and tangential forces acting on the rotor are also extracted and reported for all three cases in fig. 3.28:

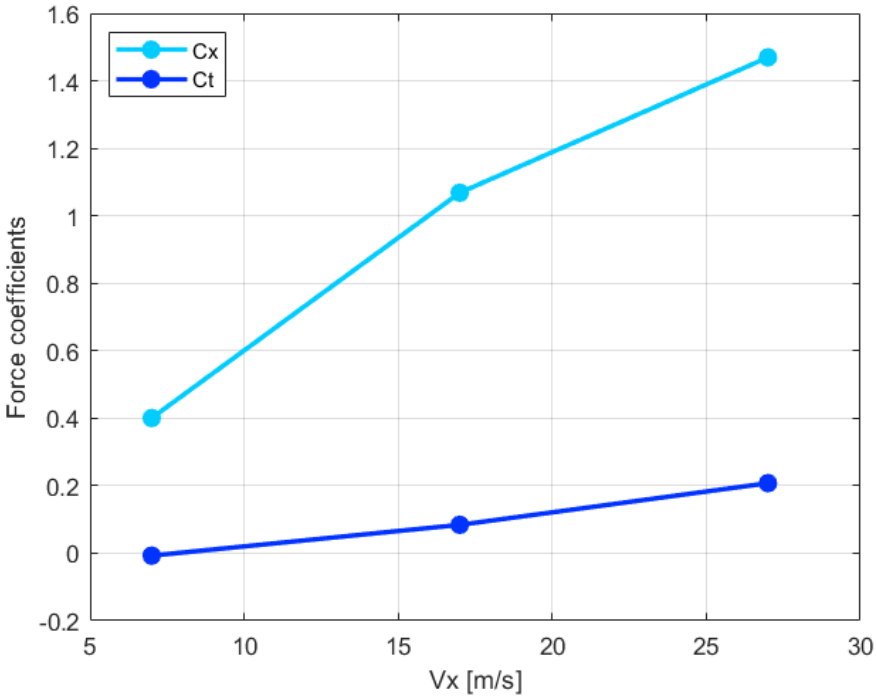

Figure 3.28: Axial and Tangential force coefficients on the rotor

4 | Parametric Analysis

This chapter presents the parametric analysis that describes the turbine's behavior under the influence of various types of waves, and its results.

The four geometries analyzed in this study,

- Only rotor with constant chord
- Only rotor with constant solidity
- Rotor with constant chord and VIGV
- Rotor with constant solidity and VIGV

are tested with waves of different maximum amplitudes to understand which solutions are better and what are the critical aspects.

The dimensions of the machine and the input data are specified in Chapter 2.

In the beginning, the behavior of the machine is analysed along the single period of three characteristic waves with $f = 0.1\ [Hz]$:

- The standard wave ($a = 2\ [m]$): this is the wave used to size the turbine.
- a wave stronger by 25% ($a = 2.5\ [m]$)
- a wave weaker by 25% ($a = 1.5\ [m]$)

On these waves, the power production over the period, the incidence of the flow on the rotor, and the control exerted on it (when needed) by the VIGV, are analysed.

Subsequently, the average power production is analysed across various waves of different amplitudes.

The performance is analysed over a quarter of the period, since it is sinusoidal and subject to temporal symmetry, from the moment when the velocity is maximum to the moment when it is minimum.

4.1. Effect of the standard wave

$a = 2\ [m]$

This wave can be seen as an operational limit: the turbine has been sized based on its parameters, which means that when it encounters a wave of this type, the stall phenomenon does not occur. The hub region, which is most affected by it, reaches the limit incidence (without exceeding that value) when the air velocity induced by the wave is highest. Waves stronger than this one lead to the stall of a portion of the blade or even the entire blade.

As can be seen from fig. 4.1, in fact, the upstream stator does not come into play to reduce the incidence on the rotor. It only activates during the total-drag phase (actually, a bit earlier) to try to delay the onset of this phase and increase the power production in the final part of the period, as visible in fig. 4.2.

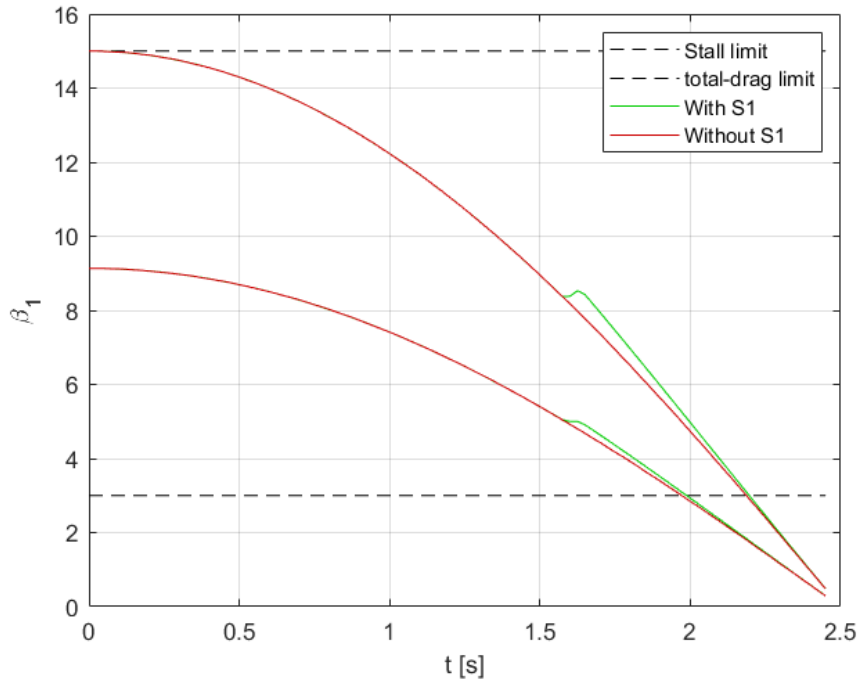

Figure 4.1: Incidence at the hub (up) and at the tip (down) during the period of the standard wave

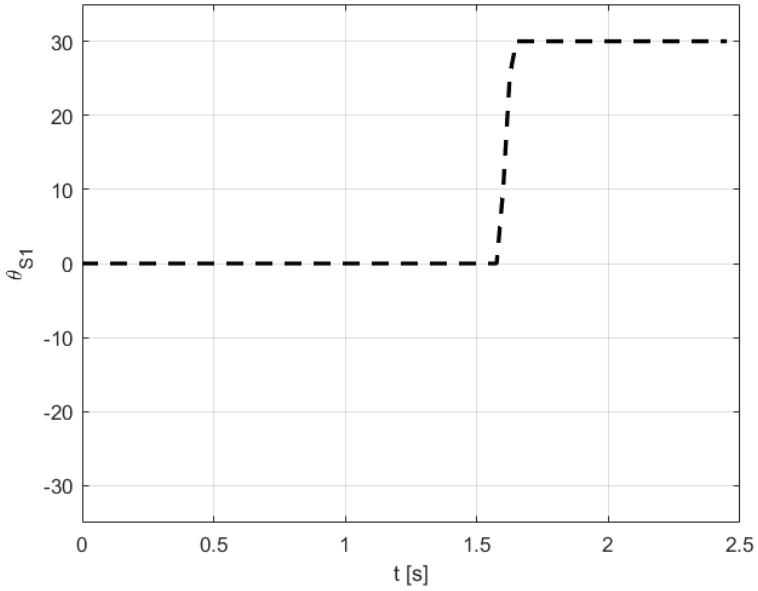

Figure 4.2: Orientation of S1 during the standard wave

For what concerns the power production during the period of the standard wave, the four configurations are compared in fig. 4.3:

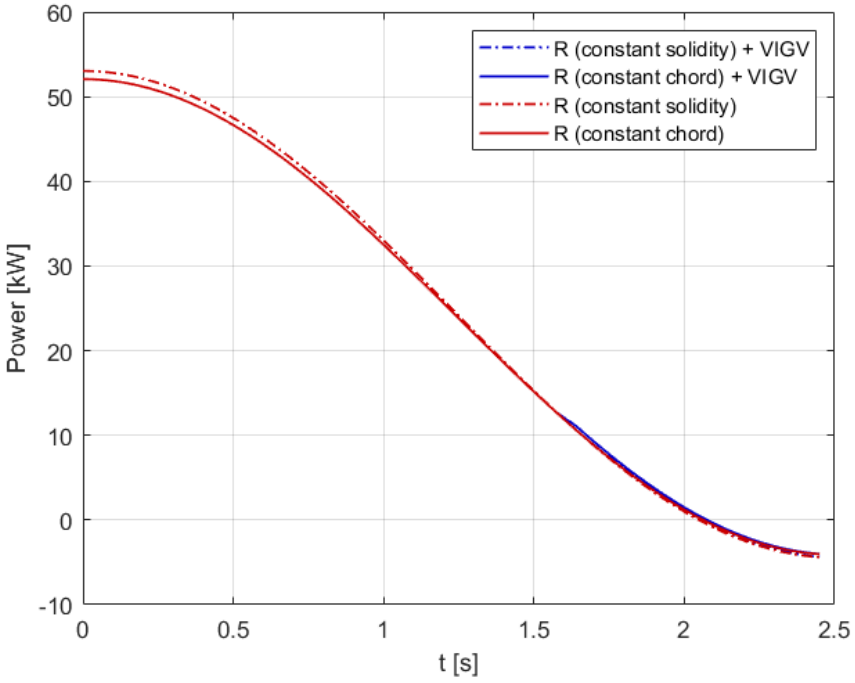

Figure 4.3: Power production during the period of the standard wave

The four configurations have very similar behavior (so much that the solutions with the stators perfectly overlap with those without them in the part of the period where they are not acting). The constant solidity configuration is slightly better than the constant chord one.

To define how effectively this power is generated, the efficiency parameter is used, whose behavior is described in fig. 4.4:

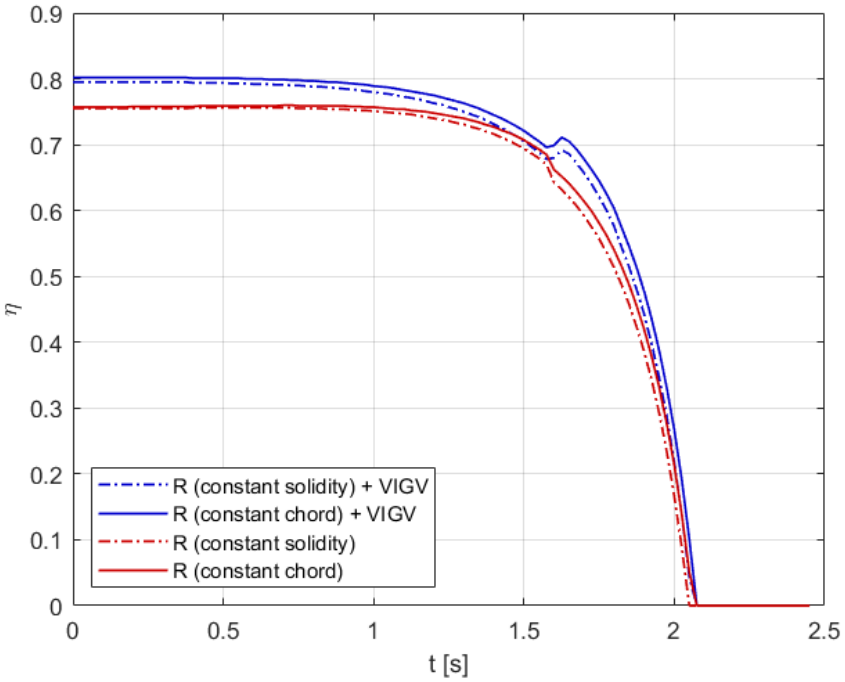

Figure 4.4: Efficiency during the period of the standard wave

There are no significant changes between cases with only the rotor, while, as can be seen, efficiency increases when the VIGV are present. This is because throughout the entire period, the downstream stator is recovering some of the kinetic energy at the outlet, and particularly, when activated, the upstream stator increases the power produced in the last part of the period.

When the efficiency is zero, the turbine is in the total-drag phase, where it is the turbine that performs work on the fluid, that is nearly stagnant, rotating only due to inertia.

4.2. Effect of different waves

$a = 2.5\ [m]$

This wave has an amplitude that is 25% higher than the standard one. Under the influence of this wave, during the first part of the period, the turbine is subject to the stall phenomenon (and, of course, also to the of total-drag in the final phase). In this scenario, the upstream stator comes into play to reduce the incidences during the initial part of the period.

In fig. 4.5 the incidence history at the hub is reported:

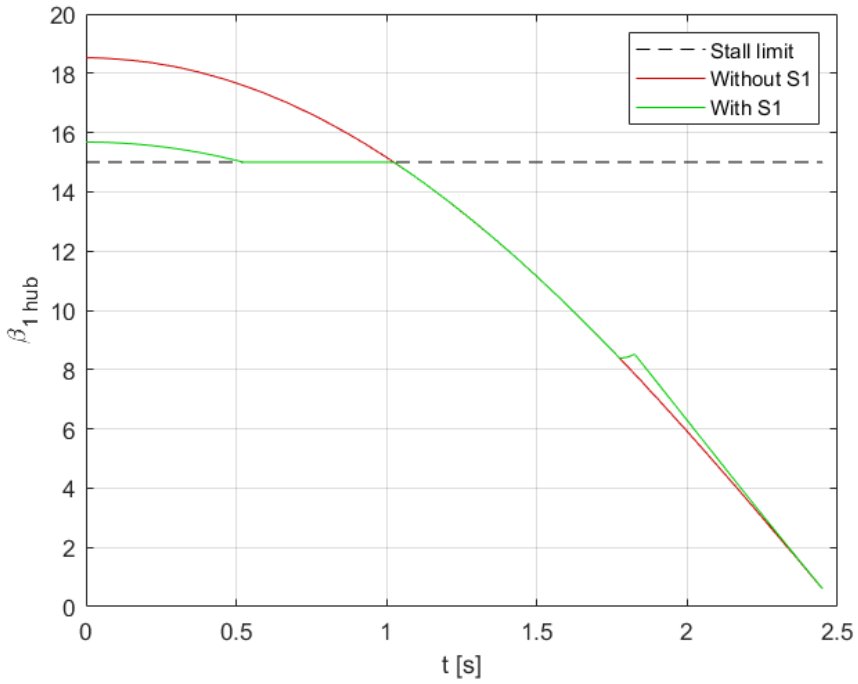

Figure 4.5: Incidence at the hub during the period of a stronger wave

The configuration with only the rotor shows incidence angles well above the stall. The upstream stator is capable of significantly reduce this phenomenon, keeping the rotor at the limit incidence, avoiding critical situations for a good portion of the period during which it would stall.

In the very early phase of the period, the VIGV cannot fully keep the angle below the limit. This is due to the fact that a maximum rotation of 30 [deg] has been imposed, although an optimized VIGV system may be able to handle much higher incidences, up to 60 [deg] avoiding completely the stall.

It's also possible to observe an attempt to correct the total drag phase, where the stator causes a slight increase in incidence on the rotor.

In fig. 4.6, on the other hand, the orientation of the upstream stator during the considered period is represented:

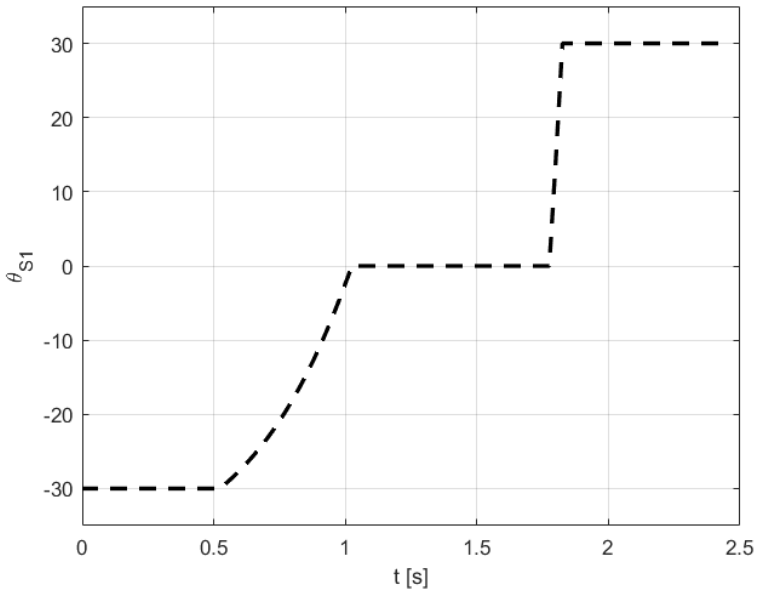

Figure 4.6: Orientation of S1 during a stronger wave

Unable to rotate beyond the maximum imposed incidence, it stays at -30 [deg] in the first part of the period to reduce the stall as much as possible. From the moment it proceeds from -30 [deg] towards 0 [deg], it corrects it completely. It remains constant at 0 [deg] when there are no phenomena to correct. Towards the end of the period, it bends up to +30 [deg] to keep the incidence on the rotor as high as possible, trying to delay the total drag, and finally remains at +30 [deg], being the maximum imposed incidence.

At this point, the power production over the period is analyzed in fig. 4.7, comparing the different configurations:

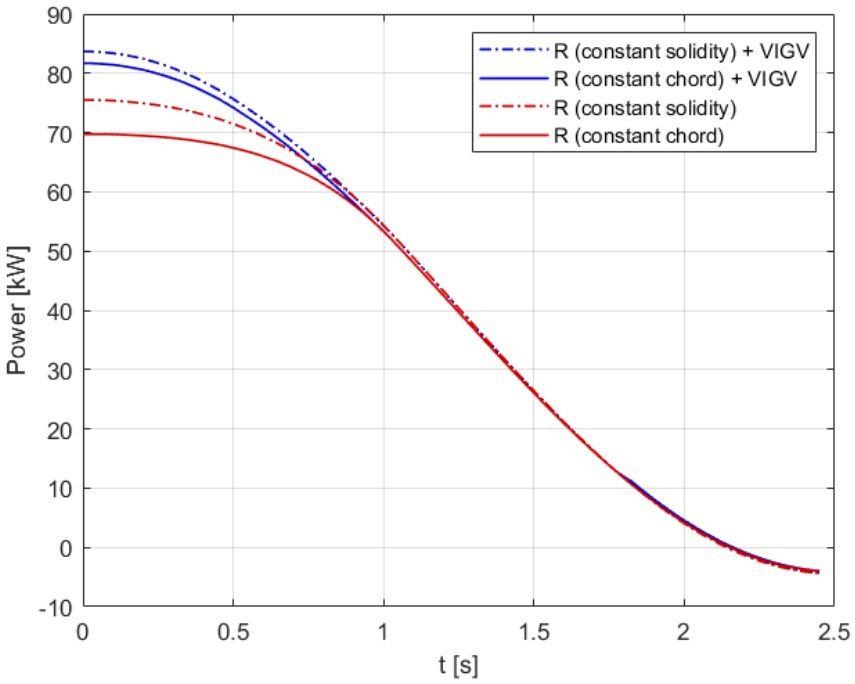

Figure 4.7: Power production during the period of a stronger wave

Solutions that involve the use of VIGV increase power production by extending the operating range of the turbine, preventing force coefficients from dropping abruptly in blade regions subject to excessively high incidences.

Furthermore, a configuration with a rotor of constant solidity proves to be better than a rotor with constant chord, in terms of power generation.

Regarding the total drag phase, there aren't any truly significant corrections: the additional power produced due to the stator action is visibly minimal.

To define how effectively this power is generated, the efficiency parameter is used, whose behavior is described in fig. 4.8.

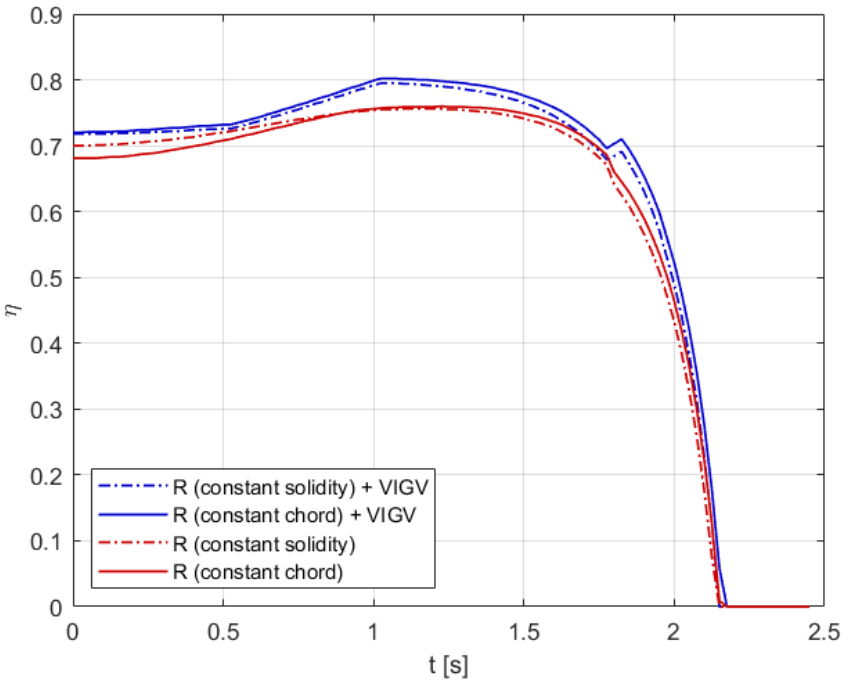

Figure 4.8: Efficiency during the period of the standard wave

As before, there are no significant changes between cases with only the rotor, while, as can be seen, efficiency increases when the VIGV are present. This is because throughout the entire period, the downstream stator is recovering some of the kinetic energy at the outlet, and particularly, when activated, the upstream stator reduces the power dissipated by drag in the first part of the period that it is quite high if the rotor stalls, and increases the power produced in the last part of the period.

$a = 1.5\ [m]$

This wave is weaker by 25% compared to the standard one. Being a wave of low intensity, there won't be stall phenomena on the rotor, but the total-drag phase is more significant. The region most affected by this phenomenon is the tip.

In fig. 4.9 the incidence history at the tip is reported:

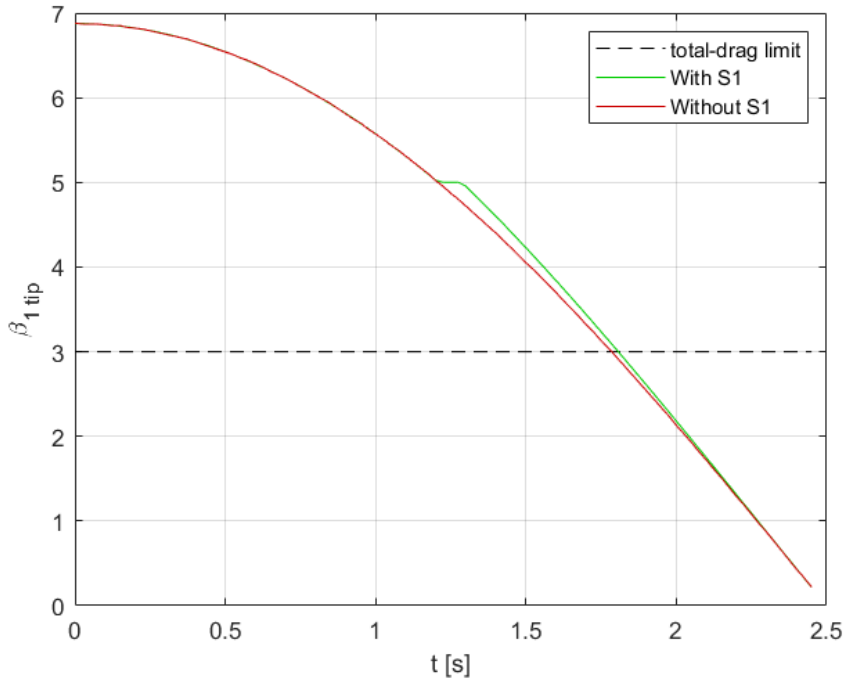

Figure 4.9: Incidence at the tip during the period of a weaker wave

As always, the upstream stator is activated before entering the total drag phase, in an attempt to increase power production in the final part of the period.

In fig. 4.10, on the other hand, the orientation of the upstream stator during the considered period is represented.

In this case, there is no stall to correct, so it remains stationary with zero incidence throughout the first part of the period. Shortly before the turbine enters the total-drag phase, it quickly rotates to the maximum imposed incidence.

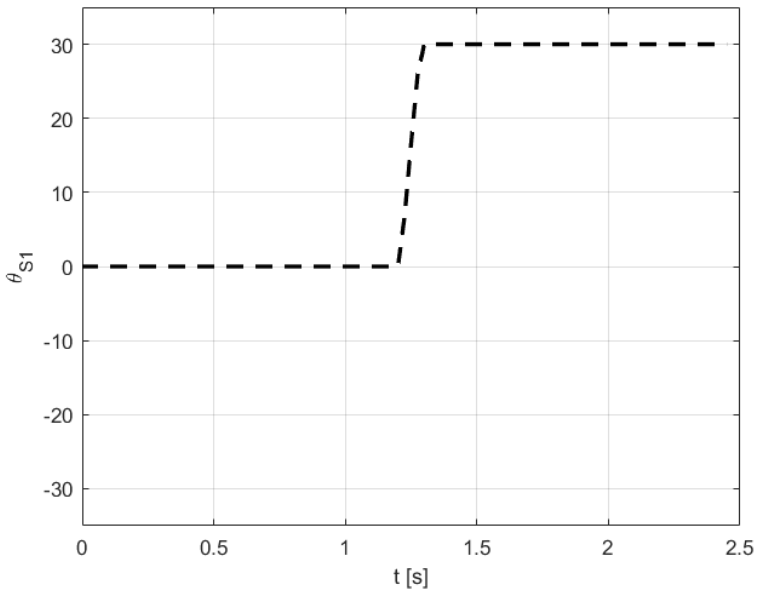

Figure 4.10: Orientation of S1 during a weaker wave

Regarding power production, the four configurations behave similarly to each other, considering that a solution with constant solidity consistently proves to be better than one with constant chord.

The total drag phase is not significantly delayed by the action of the upstream stator, which is also moved before the critical phenomenon occurs, attempting to generate more power in the final phase of the period. In this case as well, a maximum rotation has been imposed, which is significantly lower than what an optimized VIGV system could achieve.

Since power production is low for weak waves, and in general, the total-drag phase is not significantly improved, it makes sense that, for weak waves, the stator is rotated from the beginning of the period to keep incidences on the rotor as high as possible (without exceeding the stall limit), to increase power production throughout the entire period.

In fig. 4.11 is reported the power production according to the canonical control law for the upstream stator, and in fig. 4.12 is reported the power production trend for the same wave when the upstream stator is always deflected by the maximum rotation imposed (+30 [deg]):

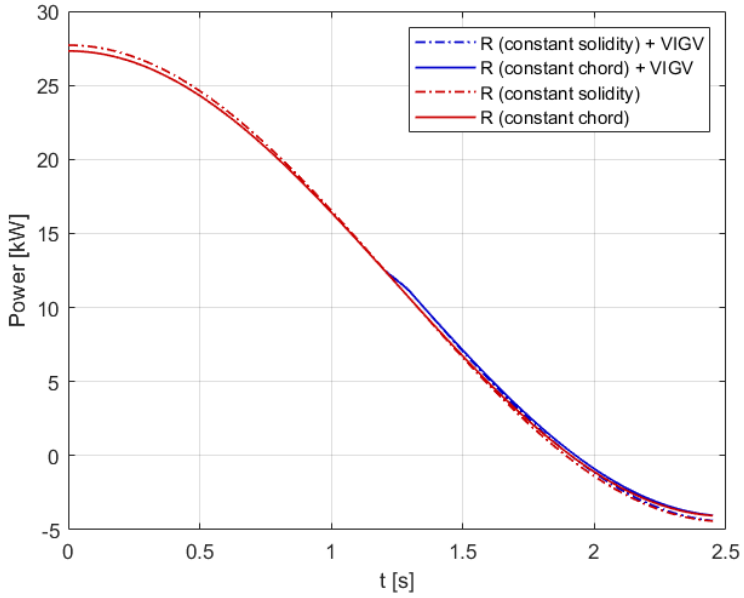

Figure 4.11: Power production during the period of a weaker wave (1)

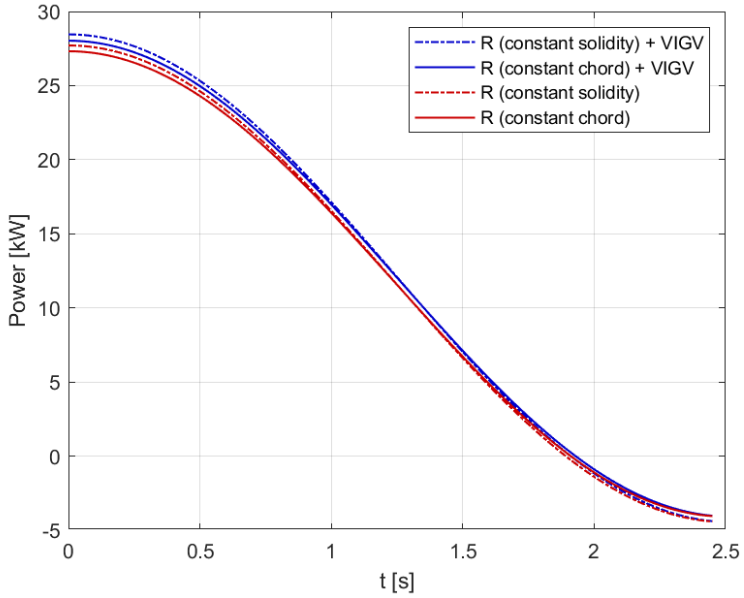

Figure 4.12: Power production during the period of a weaker wave (2)

A Wells turbine equipped with VIGVs does not worsen the effect of a wave weaker than the standard one but improves it only slightly. Certainly, for low waves, it is better that the stator is fully deflected during the whole period in favor of high incidences on the rotor.

To define how effectively this power is generated, the efficiency parameter is used, whose behavior is described in fig. 4.13.

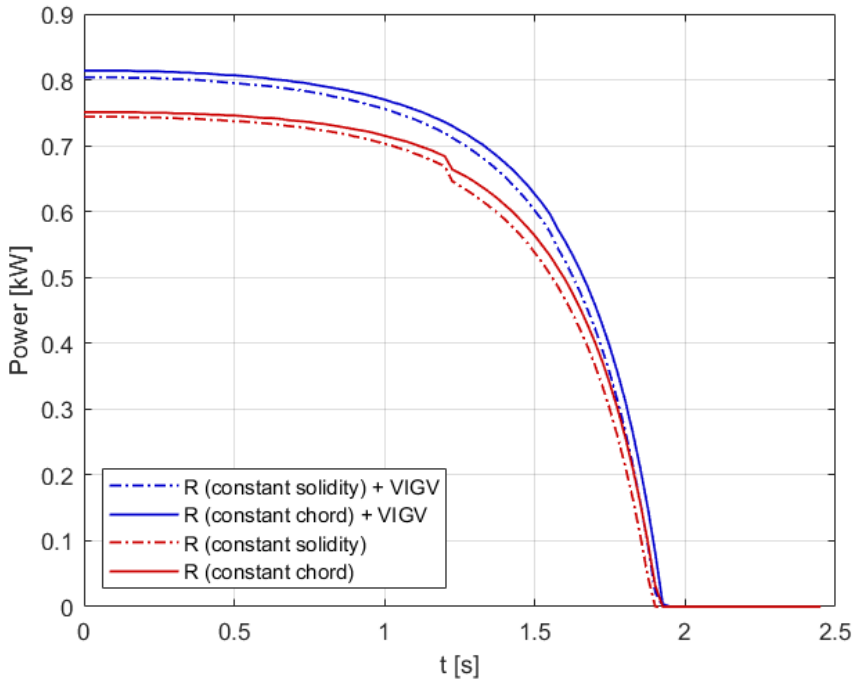

Figure 4.13: Efficiency during the period of the standard wave

As before, there are no significant changes between cases with only the rotor, while, as can be seen, efficiency increases when the VIGV are present. This is because throughout the entire period, the downstream stator is recovering some of the kinetic energy at the outlet, and the upstream stator is trying to maximise the power production during the whole period.

4.3. Power production under different waves

Analyzing what happens in a single period is appropriate to understand the dynamics in each phase, but, regarding power production, it is more accurate and representative to consider the average power produced during the period. Below, in fig. 4.14, are the trends of the average power produced by the four configurations analyzed in this study, for a set of waves with amplitudes:

$$a = [1\ 1.5\ 2\ 2.5\ 3]$$

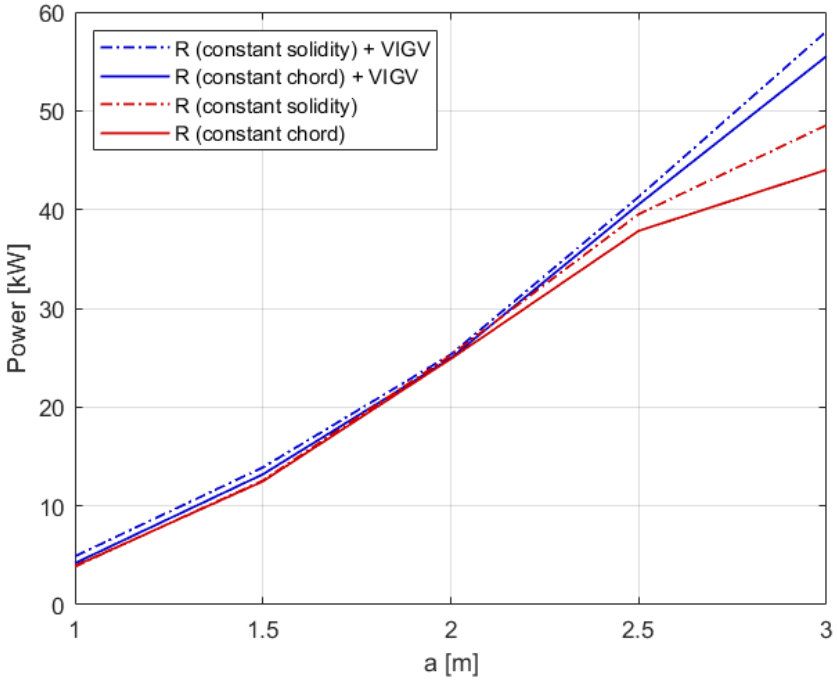

Figure 4.14: Average power production during different waves

There are no truly significant differences between constant chord or constant solidity, for waves with amplitudes lower than the standard one. A slight improvement if reached if VIGV are adopted.

Moreover, for larger amplitudes, solutions with constant solidity prove to be better than those with constant chord, and solutions equipped with Variable Inlet Guide Vanes (VIGV) turn out to be superior to those without.

5 | Conclusions and Outlook

In this work, various aspects related to Wells turbines have been analyzed. In particular, in addition to normal operating conditions, the focus is set on methods to enhance their performance and extend their operational field, even during phases when major challenges arise. The aim of this work is not to replace the existing documentation or other solutions proposed by other researches, but to contribute to it and suggest new alternatives to be considered.

For what concerns the rotor only, it certainly makes sense to consider Wells rotors with constant solidity: this type of geometry maximizes energy production compared to a rotor with constant chord. To achieve this, attention must be paid to the structural issue that could affect the blade at the root, as it presents a lower cross-section, and higher forces at the tip.

Furthermore, the use of Variable Inlet Guide Vanes (VIGV) proves to be a promising strategy to prevent stall on the rotor and extend the operational range to waves of greater amplitude than the standard one, significantly increasing energy extraction.

An important aspect to consider regarding VIGV, in a future perspective, is to optimize the blade profiles in such a way that there is a good compromise between high deflections and low losses. Another interesting aspect to investigate is a spherical inlet system associated with VIGV for which the literature suggests lower losses compared to a cylindrical inlet, paying the price of an higher structural complexity.

Regarding the total-drag phase, a VIGV system does not create truly significant modifications: the phenomenon is, in fact, inevitable.

In conclusion, it makes sense to consider building OWC (Oscillating Water Column) plants with Wells turbines equipped with VIGV systems in locations where standard waves are not a requirement, as the system would be more versatile compared to a plant equipped with regular Wells turbines.

Normally, a plant equipped with a canonical Wells turbine is designed not to stall on the standard waves of a particular location. With the addition of a VIGV system, it is

conceivable to place the plant where the waves are stronger than the standard one, as energy extraction is higher and the stall phenomenon can be fully corrected or significantly reduced. This could help compensate for the total drag phase, which proves to be always critical, especially for waves weaker than the standard one.

To conclude, it is clear that a solution of this kind entails higher costs in terms of the production and maintenance of turbines and plants. However, in exchange, it offers clean, continuous, and available energy, considering also that an OWC plant is non-invasive and not harmful to the marine ecosystem.

Bibliography

[1] A. Falcao, "Wave energy utilization: A review of the technologies," 2010.
doi: 10.1016/j.rser.2009.11.003.

[2] T. Setoguchi and M. Takao, "State of art on self-rectifying air turbines for wave energy conversion," 2006.
doi:10.1016/j.enconman.2005.11.013.

[3] L. Gato and A. Falcao, "Performance of the wells turbine with a double row of guide vanes," 1990.
doi:10.1299/jsmeb1988.33.2_265.

[4] A. Brito-Melo, L. Gato, and A. Sarmento, "Analysis of wells turbine design parameters by numerical simulation of the owc performance," 2002.
doi:10.1016/S0029-8018(01)00099-3.

[5] S. Raghunathan, "The wells air turbine for wave energy conversion," 1995.
doi:10.1016/0376-0421(95)00001-F.

[6] V. Barnabei and A. Castorrini, "Investigation of passive morphing blades forwells turbines using computational fluid-structure interaction," 2023.
Paper ID: ETC2023-177.

[7] K. Tapas and S. Abdus, "Influence of stall fences on the performance of wells turbine," 2020.
doi:10.1016/j.energy.2019.116864.

[8] D. Greenblatt and O. Pfeffermann, "Wells turbine stall control using plasma actuators," 2021.
doi:10.2514/1.J060278.

[9] J. Denton, "Loss mechanisms in turbomachinery," 1993.
doi:10.1115/93-GT-435.

[10] J. Dunham and P. Came, "Improvements to the ainley-mathieson method of turbine performance prediction," 1970.

doi:10.1115/1.3445349.

[11] M. Coppinger and E. Swain, "Performance prediction of an industrial centrifugal compressor inlet guide vane system," 2000.
doi:10.1243/0957650001538254.

[12] D. Handel and R. Niehuis, "Aerodynamic investigations of a variable inlet guide vane with symmetric profile," 2014.
doi:10.1115/GT2014-26900.

[13] D. Cebrià, O.-C. J., and R. Fernandez-Feria, "Lift and drag characteristics of a cascade of flat plates in a configuration of interest for a tidal current energy converter: Numerical simulations analysis," 2023.
doi:10.1063/1.4816495.

[14] Y. Fang, D. Sun, X. Dong, and X. Sun, "Effects of inlet swirl distortion on a multistage compressor with inlet guide vanes and stall margin enhancement method," 2023.
doi:10.3390/ aerospace10020141.

[15] J. Xin, X. Wang, and H. Liu, "Numerical investigation of variable inlet guide vanes with trailing-edge dual slots to decrease the aerodynamic load on centrifugal compressor impeller," 2016.
doi:10.1177/1687814016640653.

[16] R. Frank, C. Wacker, and R. Niehuis, "Loss characterization of a conventional variable inle guide vane," 2021.
Paper ID: ETC2021-596.

[17] Z. Zaheer, "Cfd analysis of the performance of different airfoils in ground effect," 2019.
doi:10.1088/1742-6596/1355/1/012006.

[18] M. Khalid, "Cfd analysis of naca 0012 aerofoil to investigate the effect of increasing angle of attack on coefficient of lift and coefficient of drag," 2022.
doi:10.53898/josse2022216.

[19] S. H. Lee and Y. O. Han, "Experimental investigation of high-angle-of-attack aerodynamics of low-aspect-ratio rectangular wings configured with naca0012 airfoil section," 2020.
doi:10.1007/s42405-019-00215-z.

[20] N. Ahmed, B. Yilbas, and M. Budair, "Computational study into the flow field developed around a cascade of naca 0012 airfoils," 1998. doi:10.1016/S0045-7825(98)00104-2.

[21] B. Yilbas, "Numerical simulation of the flow field around a cascade of naca 0012 airfoils-effects of solidity and stagger," 1998. doi:10.1016/S0045-7825(97)00253-3.

List of Figures

List of Tables

List of Symbols

Variable	Description	SI unit
$\boldsymbol{a}$	maximum wave height	m
$\boldsymbol{b}$	blade height	m
$\boldsymbol{B}$	shrouded/unshrouded blade coefficient	-
$\boldsymbol{c}$	chord	m
$\boldsymbol{c_D}$	drag coefficient	-
$\boldsymbol{c_L}$	lift coefficient	-
$\boldsymbol{c_P}$	pressure recovery factor	-
$\boldsymbol{d(i)}$	vector of diameters	m
$\boldsymbol{D}$	diameter	m
$\boldsymbol{D}$	drag force	N
$\boldsymbol{dr}$	portion of the radius	m
$\boldsymbol{dr_{up}}$	update of the radius	m
$\boldsymbol{e}$	elevation of the wave	m
$\boldsymbol{f}$	wave frequency	Hz
$\boldsymbol{F_t}$	tangential force	N
$\boldsymbol{F_x}$	axial force	N
$\boldsymbol{g}$	gravity	m/s^2
$\boldsymbol{h}$	diameter ratio	-
h	enthalpy	J
$\boldsymbol{i}$	counter	-
$\boldsymbol{j}$	counter	-
$\boldsymbol{k}$	clearance	m
$\boldsymbol{L}$	lift force	N
$\boldsymbol{L_{owc}}$	OWC length	m
$\boldsymbol{Ma}$	mach number	-

N_b	number of blades	-
N_t	number of time steps	-
N_p	number of points	-
P	pressure	Pa
P_a	available power	W
P_{lost}	power lost due to drag	W
P_{kin}	power lost due to kinetic energy	W
P_t	total pressure	Pa
P_{use}	useful power	W
$q(i)$	vector of volumetric flow rates	Kg/m^3
Q_{max}	max volumetric flow rate	Kg/m^3
R	air constant	$J/kg/K$
R	rothalpy	J
Re	reynolds number	-
s	pitch	m
t	time	s
T_a	air temperature	K
U	peripheral velocity	m/s
V	absolute velocity	m/s
W	relative velocity	m/s
Y	total pressure loss cefficient	-
Z_{owc}	OWC width	m
α_2	rotor discharge angle (of V)	rad
β_1	rotor incidence angle	rad
β_2	rotor discharge angle (of W)	rad
β_{max}	rotor stall incidence	rad
β_{min}	rotor total-drag incidence	rad
γ	air specific heat ratio	-
δ_{s_2}	downstream stator incidence angle	rad
ζ	kinetic energy loss coefficient	-
η	efficiency	-
θ_{s_1}	upstream stator rotation angle	rad
θ_{s_2}	downstream stator rotation angle	rad

$\boldsymbol{\mu}$	air viscosity	$Pa \cdot s$
$\boldsymbol{\pi}$	pi	-
$\boldsymbol{\rho}$	density	Kg/m^3
$\boldsymbol{\sigma}$	solidity	-
$\boldsymbol{\tau}$	thickness	m
$\boldsymbol{\omega}$	rotational speed	rpm

List of Subscripts

Subscript	Description
0	quantity related to section 0
1	quantity related to section 1
2	quantity related to section 2
3	quantity related to section 3
4	quantity related to section 4
$\boldsymbol{s_1}$	quantity related to the upstream stator
$\boldsymbol{s_2}$	quantity related to the downstream stator
$\boldsymbol{t}$	total quantity
$\boldsymbol{t}$	tangential component
$\boldsymbol{x}$	axial component
$\boldsymbol{h}$	quantity related to the hub
$\boldsymbol{m}$	quantity related to the midspan
$\boldsymbol{t}$	quantity related to the tip
$\boldsymbol{c}$	related to clearance losses
$\boldsymbol{p}$	related to profile losses

List of Acronyms

Acronym	Description
$\boldsymbol{AR}$	Aspect ratio
$\boldsymbol{FP}$	Flat plates

$\boldsymbol{IGV}$	Inlet guide vanes
$\boldsymbol{VIGV}$	Variable inlet guide vanes
$\boldsymbol{CFD}$	Computational fluid dynamics
$\boldsymbol{OWC}$	Oscillating water column
$\boldsymbol{S1}$	Upstream stator
$\boldsymbol{S2}$	Downstream stator
$\boldsymbol{R_c}$	Rotor (with constant chord)
$\boldsymbol{R_s}$	Rotor (with constant solidity)

Acknowledgements

I would like to express my gratitude to my advisor Prof. Paolo Gaetani for the opportunity to work on this project and for the passion for the subject conveyed during the Turbomachinery course. Additionally, I want to thank my coadvisor Noraiz Mushtaq for the support provided throughout the work.

I warmly thank my family, my friends and my colleagues.